Edge states, Magnetisation and Topological domain walls in Graphene

by
Yang Liu

A Doctoral Thesis

Submitted in partial fulfilment of the requirements for the award of
Doctor of Philosophy of Loughborough University

September 2015

Certificate of Originality
Thesis Access Conditions and Deposit Agreement

Students should consult the guidance notes on the electronic thesis deposit and the access conditions in the University's Code of Practice on Research Degree Programmes

Author……...……..…….

Title……..

I [Please insert name and address], "the Depositor",
would like to deposit [Please insert title of dissertation], hereafter referred to as the "Work", once it has successfully been examined in Loughborough University Institutional Repository

Status of access OPEN / RESTRICTED / CONFIDENTIAL

Moratorium Period……years, ending……../……20…….

Status of access approved by (CAPITALS):……

Supervisor (Signature)……...……...

School of……...……

Author's Declaration *I confirm the following :*

CERTIFICATE OF ORIGINALITY
This is to certify that I am responsible for the work submitted in this thesis, that the original work is my own except as specified in acknowledgements or in footnotes, and that neither the thesis nor the original work therein has been submitted to this or any other institution for a degree

NON-EXCLUSIVE RIGHTS
The licence rights granted to Loughborough University Institutional Repository through this agreement are entirely non-exclusive and royalty free. I am free to publish the Work in its present version or future versions elsewhere. I agree that Loughborough University Institutional Repository administrators or any third party with whom Loughborough University Institutional Repository has an agreement to do so may, without changing content, convert the Work to any medium or format for the purpose of future preservation and accessibility.

DEPOSIT IN LOUGHBOROUGH UNIVERSITY INSTITUTIONAL REPOSITORY
I understand that open access work deposited in Loughborough University Institutional Repository will be accessible to a wide variety of people and institutions - including automated agents - via the World Wide Web. An electronic copy of my thesis may also be included in the British Library Electronic Theses On-line System (EThOS). I understand that once the Work is deposited, a citation to the Work will always remain visible. Removal of the Work can be made after discussion with Loughborough University Institutional Repository, who shall make best efforts to ensure removal of the Work from any third party with whom Loughborough University Institutional Repository has an agreement. Restricted or Confidential access material will not be available on the World Wide Web until the moratorium period has expired.

- That I am the author of the Work and have the authority to make this agreement and to hereby give Loughborough University Institutional Repository administrators the right to make available the Work in the way described above.

- That I have exercised reasonable care to ensure that the Work is original, and does not to the best of my knowledge break any UK law or infringe any third party's copyright or other Intellectual Property Right. I have read the University's guidance on third party copyright material in theses.
- The administrators of Loughborough University Institutional Repository do not hold any obligation to take legal action on behalf of the Depositor, or other rights holders, in the event of breach of Intellectual Property Rights, or any other right, in the material deposited.

*The statement below shall apply to **ALL** copies:*

This copy has been supplied on the understanding that it is copyright material and that no quotation from the thesis may be published without proper acknowledgement.

Restricted/confidential work: All access and any copying shall be strictly subject to written permission from the University Dean of School and any external sponsor, if any.

Author's signature……..Date……...……...……

user's declaration: for signature during any Moratorium period (Not Open work): ***I undertake to uphold the above conditions:***			
Date	Name (CAPITALS)	Signature	Address

Abstract

In modern electric and electronic engineering and industry, silicon based semiconductor technology has been dominating for almost a century. However, the search for evolutionary successors of the silicon has never been stopped.

Since last decade, graphene started to draw much attention as a novel prospective material for the semiconductor industry. Composed of a single layer graphite, graphene reveals many extraordinary physical properties. Mechanically, it is the strongest material ever known due to the very strong covalent bonds binding its carbon atoms. Optically, it has a broaden absorption spectrum due to its non-trivial band structures. Electrically, it has the highest conductivity at low energies due to its special energy spectrum together with its rigid and neat lattice structures. Further, the graphene has been reported to be able to reveal quantum Hall effect at room temperature with affordable magnetic fields. It also shows (anti) weak localization phenomenon. Therefore, the graphene is hopefully a proper material to investigate many quantum effects and their applications at room temperature. Graphene is also bio-friendly and safe to use in biotechnologies. Due to the high surface to volume ratio, it is efficient in absorbing molecules. By the virtue of its many useful properties, graphene may have many applications in electronics, optics, optoelectronics, bio-devices and many other fields. In this thesis, we are mostly interested in its electronic transport and magnetic properties.

The main goal of this thesis is to study the edge states and their roles in conductivity and magnetism of graphene nanoribbions and flakes. In Chapter 2, we have analytically and numerically investigated the electron transmission properties of graphene nanoribbions with zigzag and armchair edges. The obtained results show the direct connections between the edge states and the transport properties of graphene nanoribbons. In the end of the chapter we also emphasized the relationships between the integer quantum Hall effect and the edge states. To investigate the quantum interference effect in graphene nanodevices, we have studied the Aharonov-Bohm effect in graphene nanodisks and rings in Chapter 3. The numerical simulations have revealed a conventional Aharonov-Bohm effect in these structures, while account of the confinement effects originated from the edges results in

the suppression of the conductivity peaks of Aharonov-Bohm oscillations. In chapter 4, we described the quantum oscillations of the magnetization of graphene flakes. At small values of the magnetic field, the diamagnetic curves of graphene flakes show characteristics of both the Aharonov-Bohm and De Haas-van Alphen oscillations. Whereas at very high field, the De Haas-van Alphen oscillations take non-trivial shape related to the graphene spectrum in the form of Hofstadter's butterfly. In Chapter 5, we have investigated the transmission and magnetization properties related to the distortions induced by pseudo magnetic fields in graphene lattices. The lattice distortions break the time-reversal symmetry in either valley of the two kinds of Dirac points while remain the time-reversal symmetry of the whole lattice system. Therefore, any effects that break the valley symmetry are hopefully able to result in the observable effect which reveals the influence of the pseudo magnetic field. In Chapter 5, we have used an extra magnetic field to break the symmetry of the two sublattices and valleys. The resulting oscillations of the diamagnetic curves of graphene samples exhibited close relationships between the magnetizations and the pseudo magnetic fields related to the lattice distortions. The topological aspects of the graphene systems are considered in chapter 6. There, we have examined the snake-like states of transport electrons in the configurations of graphene ribbons with a domain wall in the centre. The comparisons between the two cases of the graphene PN-junction and the configuration of the graphene ribbon with antisymmetric magnetic fields are studied. The calculated Thouless-Kohmoto-Nightingale-den Nijs topological invariants confirmed the topological equivalence of the above two cases. The dualities of electrical and magnetic field actions have also been investigated in this chapter.

Acknowledgements

First and foremost I would like to thank my supervisor, Professor Feo Kusmartsev, who is remarkably knowledgeable in the area of the research of this thesis. He has given me extraordinarily great help and tutorial through my years of research. My evident improvement of knowledge in condensed matter physics is highly due to his help. And he also provided me the financial support. Besides work, he is also a good friend and care about my daily life. I am lucky and happy to be his student.

In the last year of my PhD course, I had worked together with professor Eugene Mele. I feel great appreciate to his help and the time he spent on me. Through the short one year time, my knowledge of the theoretical physics improved evidently. I am also impressed by his hard working, the high efficiency and enthusiasm that he has in doing the research. He has set a role model for me.

I have cooperated with a Switzerland group in the university of Basel lead by Professor Christoph Bruder and Rakesh Tiwari. We had a lot of online discuss and Rakesh had made a travel to us for a short period of communication.

I also would like to say thanks to my personal tutor, Doctor Binoy Sobnack, who has been a good friend to me and helped me go through many challenges in the daily life.

I owe my parents a lot. They kept supporting me financially and emotionally. I had few times returned home to see them, but I am sure that they had worries no less than mine. They encouraged me to work hard.

In the past years since I come to this nation, I have met many friends here. They have helped me, supported me and brought me happiness through ages. Many of them have left for home but the memories of those happy moments remain. There has been and will be many hurdles in study, but from my friends I have gained energy. I didn't list the names of them, but I would like to say thanks to them all.

Contents

List of Figures

List of Tables

Chapter 1

Introduction

Carbon is the basic element of life on the earth. In the virtue of its flexibility of bonding among carbon atoms, the carbon systems create several different configurations, the allotropes. E.g. diamond, graphite/graphene, carbon nanotube, fullerene etc. Graphene is a two dimensional allotrope of carbon with honeycomb lattice structures and can be seen as the single layer graphite. The conducting electron gas is confined in a narrow layer which is about single to 2 atoms width in z direction. In 1947, P. R. Wallace first studied the band structures of graphene [1] by using the tight-binding method. His result showed a gapless spectrum at Dirac points.

In year 2004, graphene was first time succeeded (mechanical) exfoliate isolated from graphite. Andre Geim and Konstantin Novoselov won the 2010 Nobel Prize for their work [2, 3].

The special massless chiral Dirac fermions (low energy excitations) in graphene with relativistic energy spectrum lead to abundant of interesting properties. Some straightforward examples include the ambipolar field effect [4, 5], Klein tunneling and similar phenomenon [6, 7, 8]. Due to the chirality property of graphene's sublattices, the transmission probability of quantum tunneling of electrons through the potential barrier is angle dependent [6, 7]. The Klein tunneling effect has been observed in the case of electron's transport penetrating through the electrostatic barriers [9]. Together with its high mobility ($\sim 10^5 cm^2 V^{-1} s^{-1}$ at room temperature) and fast Fermi-velocity ($1/300c$, c is the speed of light), these properties of graphene immediate draw attentions in potential uses for constructing high speed field-effect transistors (FETs) [10] and optoelectronic devices [11].

Another extraordinary property of graphene is the observation of quantum Hall effect (QHE) at room temperature by using the achievable field strength (B=45T) [12]. While the observation of quantum Hall effect in conventional materials requires very low temperature

in the presence of an accessible field strength. In more critical conditions, fractional quantum Hall effect (FQHE) has also been detected in graphene [13, 14].

In mesoscopic systems, the edge states become important and dominated the electric properties of the materials. The edge states are believed to carry the conductivity when the Fermi surfaces are deviated from the positions of the resonant states. In quantum Hall effect, the conduction currents are constituted by these edge states. In the quantum dots, the edge states shape the diagram of diamagnetization curve [15]. Originated from the two sublattices nature of graphene, the boundary conditions become complicated problems and they are angel dependent [16, 17]. The most popular and well studied specific edges are zigzag and armchair edges. The systems with either of these two edges have evidently different spectrums: there are localized edges states related to the zero energy band in zigzag graphene nanoribbons while the same edge states do not appear in armchair nanoribbons [18, 19]. Further, the armchair boundary mixes the wavefunctions of the electrons in two Dirac valleys of graphene's spectrum while the zigzag boundary does not. In the presence of an external magnetic field, the bulk Landau levels (LLs) bend up towards higher energy levels when the charge concentrations move closer to the edges of the sample. The chiral natural of the graphene lattices lead to the anomalous integer quantum Hall effect [20, 21]. In practice, because most graphene samples are sustained on SiO_2 substrates, the edge reconstruction is detectable together with the QHE edge states. To choose either of the phenomenon to be observed, one can tune the electrostatic potentials near the edges through the screening method [22].

When the stress/strain is imposed on the graphene sheet, graphene can create gauge fields in its sublattices. With delicate fabrications, this distortion induced gauge fields can be made similar to the external magnetic fields [23, 24, 25]. Although the stain field cannot break the time-reversal (T) symmetry of the system as a whole, in either of the two valleys, the T-symmetry is broken respectively. The strain field is likely to cause such physical observables as Shubnikov-de Haas (ShdH) and dHvA oscillations. Based on the similar mechanism, the presence of the flat zero energy states in corrugated graphene sheet have also been predicted [26, 27, 28, 23].

1.1 Lattice structure and tight binding approximation

Monolayer graphene is made of a planar sheet of carbon atoms arranged in a honeycomb lattice, as shown in Fig. 1.1. The honeycomb lattice is constituted from a triangular lattice with two atoms per unit cell. The stability of this lattice structure comes from the covalent bonds binding carbon atoms and the bonds are formed through the orbital hybridization of electrons orbiting the atoms. Each carbon atom has 4 valence electrons and they occupy

$2s(\uparrow\downarrow)2p(\uparrow\uparrow)$ orbitals. First, the 2s orbital spin down electron can be excited to a 2p spin up state resulting in the $2s^1 2p^3$ configuration. Then the s and p orbitals partially overlapped and mixed to create hybridized bonds. Graphene lattice is result from the sp^2 hybridization where the 2s orbital is hybridized with 2 2p orbitals to create 3 equivalent σ-band (accompany with 3 σ^*-antiband). These bands serve as covalent bonds binding carbon atoms which hold the lattice together firmly. The left out of plane p_z orbital is weakly coupled with its neighbors and form a π (and π^*) band. The σ bands are far below the Fermi surface thus are the valence bands. For each carbon atom in graphene lattice, there is 1 electron per atom sits in π band, thus the electrons orbitals of graphene are half filled in charge neutral conditions. In another word, the Fermi surface is located at the centre of the $\pi(\pi^*)$ band. Therefore, the π band is most important in determining the electronic properties of graphene and it is the only band been taken into account in the effective Hamiltonian's approximation.

In the tight binding approximation, electrons are thought to be localized in the vicinity of the lattice atoms (ions). The Hamiltonian is then written as

$$H = \sum_{r_i, r_j} \varepsilon_{r_i, r_j} |r_i\rangle\langle r_j|. \tag{1.1}$$

From Bloch's theorem, the envelope wave function has the form:

$$\Psi_k(r) = \sum_R e^{ik\cdot R}[c_a\psi_A(r-R) + c_b\psi_B(r-R)], \tag{1.2}$$

where $\psi_A(r)$ and $\psi_B(r)$ are related to the A and B sites of graphene respectively.

Then substitute the wave function Eq. 1.2 into the tight binding Hamiltonian Eq. 1.1. For the simplest approximation, we integrate only the hopping integrals from the nearest neighbor sites. Meanwhile we treat all the other hopping integral (probability) terms between sites with distance further than the nearest neighbors to be equal to zero. This approximation results in the Hamiltonian having the form of the matrix

$$H = v_f \begin{pmatrix} 0 & 1 + e^{-i\frac{\sqrt{3}}{2}k_y a 2cos\frac{k_x a}{2}} \\ 1 + e^{i\frac{\sqrt{3}}{2}k_y a 2cos\frac{k_x a}{2}} & 0 \end{pmatrix}. \tag{1.3}$$

The corresponding energy spectrum is

$$\epsilon(k) = \pm v_f \sqrt{1 + 4cos^2\frac{k_x a}{2} + 4cos\frac{k_x a}{2}cos\frac{\sqrt{3}k_y a}{2}}. \tag{1.4}$$

The energy momentum dispersion is plotted in Fig. 1.2.

There are two different sets of Dirac points in the figure of the spectrum. These Dirac points are identified as K and K' in Fig. 1.2. For the low energy approximation, we

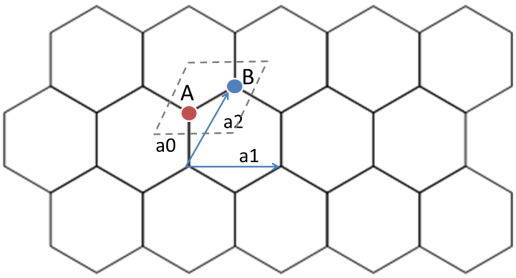

Figure 1.1: The honeycomb lattice structure of graphene. A unit cell is shown in the dashed gray diamond, which contains two atoms (a dimer) marked by A and B. a_1 and a_2 are the primitive lattice vectors. The lattice parameter is a_0. Graphene is composed by two sublattices, either of them contains A or B sites respectively.

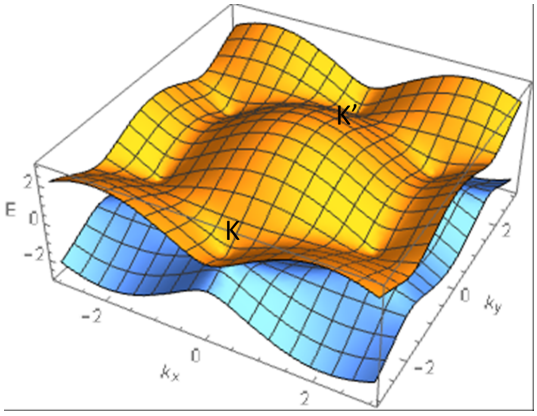

Figure 1.2: The energy momentum dispersion of graphene. The spectrum is calculated from tight binding model. In the derivative of this figure, only the nearest neighbors' hopping have been considered. From the spectrum plot here, 6 Dirac points (the positions where the two bands touch) can be seen. These Dirac points belong to two inequivalent sets which we identify them as K and K'. In the vicinity of each Dirac points, the spectrum is asymptotic to be relativistic, which is approximated through the effective Hamiltonian 1.5.

expand the whole Hamiltonian 1.3 in the vicinity of the Dirac points K and K' but omit the nonlinear corrections. We finally reach the simplified Dirac Hamiltonian 1.5

$$\hat{H} = v_f \begin{pmatrix} 0 & \hat{p}_x - i\hat{p}_y & & \\ \hat{p}_x + i\hat{p}_y & 0 & & \\ & & 0 & -\hat{p}_x + i\hat{p}_y \\ & & -\hat{p}_x - i\hat{p}_y & 0 \end{pmatrix}, \tag{1.5}$$

where $v_f = 10^8$cm s^{-1} is the Fermi velocity and $\hat{p}_{x,y}$ are the momentum operators in x, y directions respectively. The corresponding wave vectors are $\Psi(r) = (\psi_A^K, \psi_B^K, \psi_B^{K'}, \psi_A^{K'})^\intercal$.

1.2 Barrier scattering and Klein tunneling

In the vicinity of the Dirac points, graphene can be seen as zero (small) gapped semiconductors. The mechanism of the Klein tunneling is shown in Fig. 1.3a: when the incident quasiparticles transmit through the barrier region (the barrier can be made from the doping), the charge carriers convert from electrons to holes. As a consequence, when the height of the potential barrier increases, the transmission probability generally increases with a series of peak values. The transmission probabilities through the square barriers are solved by using plane wave eigenfunctions of the Dirac Hamiltonian, Eq. 1.5.

$$\Psi_k(x,y) = \begin{pmatrix} 1 \\ se^{i\theta} \end{pmatrix} e^{ik_x x} e^{ik_y y}, \tag{1.6}$$

where $\theta = Arctan\frac{k_y}{k_x}$ is the incident angle of the wave vectors, the value of s is +1 for the electron band and -1 for the hole band.

Then we use the continuous boundary conditions on the edges of the barrier. The final result of the transmission probability is described by Eq. 1.7 and the contour plot of the transmission probability in logarithm scale is shown in Fig. 1.3b. [1]

$$T = \frac{cos^2\theta_1 cos^2\theta_2}{(cos(2q_x L)cos\theta_1 cos\theta_2) + sin^2(2q_x L)(1 - ss' sin\theta_1 sin\theta_2))}. \tag{1.7}$$

1.3 Quantum Hall effect and edge states

When an external magnetic field perpendicular to the graphene is applied, the Landau Levels (LLs) are formed in the bulk of the material. Approaching to the edges, the LLs tend to bend up to higher energy levels due to the confinement effect of the edges.

The effect of the magnetic field can be introduced through Peierl's substitution $\hat{p} \rightarrow \hat{p} - \frac{e}{c}\vec{A}$ [29]. Then we obtain the modified Hamiltonian of the form

[1] This result was first calculated by another student, I made little corrections and plotted the figure.

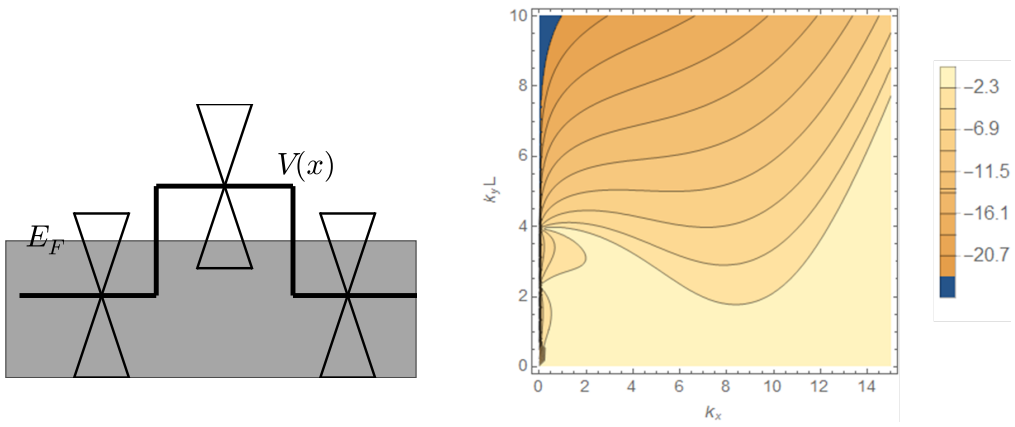

(a) (b)

Figure 1.3: (a) A Schematic show of the Klein tunneling. The cones represent the spectrum near the Dirac points. The flat gray line is the position of the Fermi energy. In the schematic figure, the Fermi surface sits in the electron band out of the barrier. Inside the barrier, the Fermi surface sits in the hole band of the Dirac cone. The transmission is taken place through the conversion of charge carriers, which are the electrons out of the barrier and holes in the barrier. (b) Contour plot of the logarithm of the electron transmission probability through a single square barrier. The height of the barrier is $U = 90meV$ and the width $L = 50nm$. The transmission probability is angle dependent.

$$\hat{H} = v_f \begin{pmatrix} 0 & \hat{p}_x - i\hat{p}_y - \frac{e}{c}\vec{A} \\ \hat{p}_x + i\hat{p}_y - \frac{e}{c}\vec{A} & 0 \end{pmatrix}, \tag{1.8}$$

where $\vec{A} = H_0 \begin{pmatrix} -y \\ 0 \\ 0 \end{pmatrix}$ is the vector potential in Landau gauge. The related magnetic field, $H = H_0\hat{z}$ is normal to the graphene surface. This Hamiltonian gives a pair of coupled Dirac equations:

$$v_f \left(\hat{p}_x - i\hat{p}_y + \frac{e}{c}H_0 y\right) \Psi_B = E\Psi_A, \tag{1.9a}$$

$$v_f \left(\hat{p}_x + i\hat{p}_y + \frac{e}{c}H_0 y\right) \Psi_A = E\Psi_B. \tag{1.9b}$$

We seek a solution of the wavefunction in the form $\Psi_A(x,y) = e^{ik_x x}Y(y)$. Use this substitution in the Dirac equations Eq. 5.13 results in the formula below.

$$Y''(y)+\frac{1}{\hbar}\left[\frac{E^2}{v_f^2}-\frac{\hbar^2}{l_B^2}-\left(\hbar k_x+\frac{\hbar y}{l_B^2}\right)^2\right]Y(y)=0, \tag{1.10}$$

where $l_B=\sqrt{\frac{\hbar c}{eH_0}}$ is the magnetic length.

This equation has the same form as the equation of the quantum harmonic oscillator. The equation of the quantum harmonic oscillator renders a set of eigenstates corresponding to the discrete energy spectrum:

$$E_n^{e,h}=\pm v_f\sqrt{2n\frac{e\hbar H_0}{c}}, \tag{1.11}$$

where the index e refer to positive electron part of the spectrum while the index h refer to holes part of the spectrum.

In the Hall bar measurement, the transport current is carried by the edge states close to the edges of the sample. The hall conductivity is proportional to the number of the edge channels of a parameter $\frac{e^2}{h}$. The number of the edge channels is equal to the number of the LLs with energies below the Fermi surface. The plot of the spectrum of the zigzag nanoribbon is shown in Fig. 1.4. The spectrum is plotted numerically through tight-binding method, which is described in Appendix A. Each level are doubly degenerated due to the existence of the two valleys in graphene (here we have omitted the spin degeneracy). The zero energy grand states split into two at the edges of the sample: one of the two states is in the electron branch while another one is in the hole branch. After counting in the spin degeneracy, we get the Hall conductivity, which is in a simple form:

$$\sigma_{xy}=\frac{4e^2}{h}(\upsilon+\frac{1}{2}), \tag{1.12}$$

where υ is the Landau Level filling factor.

It has been reported, with very strong magnetic field, the degeneracy of the LLs can be lifted. The lift of the valley degeneracy is due to the many body interactions. And the lift of the spin degeneracy is due to the Zeeman spliting.

More details regarding the boundary conditions and edge states will be discussed in the next chapter.

1.4 Main results of this Thesis

In Chapter 2, we have examined the configurations of the edge states in graphene nanoribbons. We calculated the charge density distribution and the current corresponding to these edge states in both the cases when there is an external magnetic field and no field. The

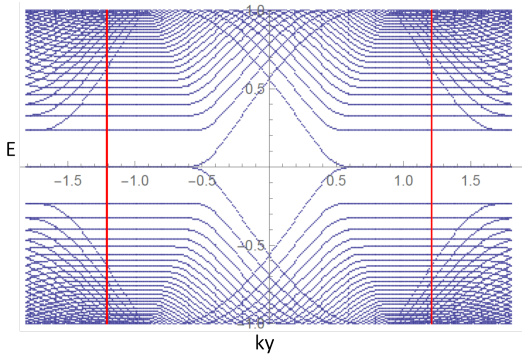

Figure 1.4: Energy spectrum in graphene nanoribbon with zigzag edges. The homogeneous magnetic field is perpendicular to the graphene sheet. The red vertical lines are the position of the Dirac points before adding the magnetic field. If taken into account of the spin degeneracy, each level is double degenerated. The zero energy states are chiral degenerated.

study showed a close connection between the conductivity of the graphene nanoribbon and the edge states. The different deploys (direction) of the edges led to different edge states.

In Chapter 3, we have investigated the Aharonov-Bohm (AB) effect in graphene. Our primary aim was to understand the transport properties of electrons through graphene quantum disks & rings and their responses to the external magnetic fields. Many coarse approximations have been made in attempting to reveal the characteristics of AB effect in graphene samples. In the end of the chapter, accurate numerical simulations based on Green's function technique have been performed. The resulting conductivity-magnetic field flux relationships showed the characteristics of AB effect together with the confinement effect from the shapes of the flakes.

In Chapter 4, we have described new quantum oscillations in the magnetisation of graphene flakes that are induced by magnetic fields which depend on the shape of the flake. At small values of the field they are due to the Aharonov-Bohm effect and with the increasing of the field they are transformed into dHvA oscillations. The specific forms of the dHvA oscillations were analyzed in terms of their energy spectrums, which have a form of Hofstadter's butterfly. Numerical results based on lattice tight-binding model and continuum Dirac equations were presented and compared. We have discussed possible experiments to investigate the quantum oscillations in Moiré and graphene anti-dot superlattices.

In Chapter 5, we have proposed an alternative way to reveal the magnetism of graphene through lattice distortions. We have calculated the magnitude of the pseudo magnetic field induced by the stress/strain of the lattice. The expected behaviors of the oscillations of the

magnetism are plotted in Section 5.5.

In Chapter 6, we focused on the domain walls in graphene sheets. We compared the two configurations of the graphene domains constructed by the use of antisymmetric chemical potential together with homogeneous magnetic field and unique chemical potential with antisymmetric magnetic field. Despite their different physical mechanisms, these configurations are topologically equivalent.

Chapter 2

Boundaries and Edgestates

2.1 Abstract

We reviewed and analyzed some boundary condition problems and edge state issues. In this chapter, we mainly considered graphene nanoribbons and sheets, with and without the external magnetic field. The low (zero) energy edge modes were observed in some edges (e.g. zigzag) while is not in some others (e.g. Armchair). When the graphene sample is exposed in an external magnetic field normal to its surface, closing to edges of graphene nanoribbons, the Landau levels (LLs) of the spectrum bend up toward higher energy levels. This behavior is similar to the cases of the systems corresponding to Pauli Hamiltonian. We made a detailed look at the graphene nanoribbons with Armchair and Zigzag edges. The analytic estimation and the numerical simulation reached good agreements in the two structures. Meanwhile, the basic numerical methods have been introduced and will be used in the following chapters throughout this thesis.

2.2 Introduction

Different from the problems which are described by Pauli Hamiltonian or formed by the square lattices, the boundary conditions of graphene are more complex due to its two sublattices composition. The sites on the two sublattices A and B are staggered, thus it is difficult to precisely define the boundaries. Practically, the properties of the boundaries are angular dependent. However, the graphene nanoribbons with ideal Zigzag and Armchair boundaries can be described properly. There are many arguments of the boundary conditions for the more general configurations of edges. [30, 31, 18] Edward and Vladimir have given the universal matrix formed boundary conditions with a few parameters to be deter-

mined. These boundary conditions are derived by taken into account all reasonable choices of the 4 dimension matrices. [30]Akhmerov and Beenakker have claimed that at low (zero) energy, the A-B sublattices are nearly decoupled and the boundaries are equivalent to either zigzag or armchair edges depending on the deployed orientations of the sample. [31] Some topological aspects on these boundary condition problems have been also presented from others' work [32, 33]. In this chapter, we will not dive into the complexity of the general boundary condition problems but stay in zigzag and armchair cases.

2.3 Graphene nanoribbons

The graphene nanoribbons with zigzag edges and armchair edges are shown in Fig. 2.1. The low excitation Dirac Hamiltonian for bulk graphene sheet is given in Eq. 1.5 and the four-spinor solutions are $(\psi_A, \psi_B, \psi'_B, \psi'_A)$. The general solutions of this Hamiltonian has the form

$$\psi_{A(B)} = (Ae^{ik_x x} + Be^{-ik_x x})e^{ik_y y}. \tag{2.1}$$

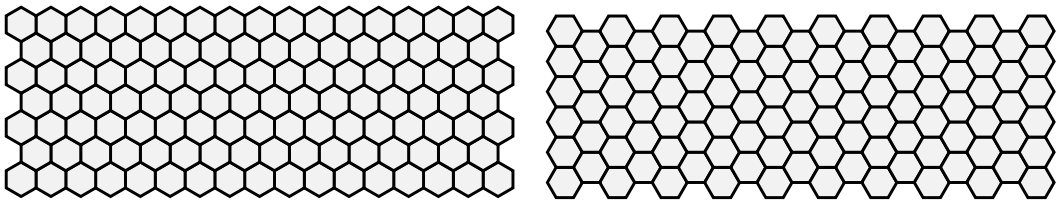

(a) (b)

Figure 2.1: The graphene ribbon with (a) zigzag edge and (b) armchair edge. In zigzag nanoribbons, on either edge (top or bottom), the sites are always terminated in one sublattice. In armchair ribbon, there are two possible combinations of the top and bottom edges. The two edges can be matched or mismatched, depending on the width of the ribbons.

2.3.1 Zigzag edges

In zigzag nanoribbons, on either zigzag edge, the sites of the graphene lattice are always terminated in only one sublattice (A or B). So it is natural to define the boundary conditions by assuming the wave functions of A or B sublattice vanish on their relevant edges respectively. Following the claim in the paper [18], the boundary conditions of the zigzag

graphene nanoribbon are described as

$$\psi_A^{(\prime)}(x=0) = \psi_B^{(\prime)}(x=L) = 0, \tag{2.2}$$

where L is the width of the ribbon.

This boundary conditions lead to two kinds of confinement criterion corresponding to the valid momentum vectors $k_x(y)$. The wave vector k_y is in the longitudinal direction where the translation invariant persists, therefore k_y is a good quantum number. The solutions are given by Eqs. (6) and (7) in the paper [18]. The two equations are related to the bulk modes and edge decay modes respectively.

$$k_y = \frac{k_x}{tan(k_x L)}, \qquad \text{Bulk modes} \tag{2.3a}$$

$$\frac{k_y + ik_x}{k_y - ik_x} = e^{2iLk_x}. \qquad \text{Edge decay modes} \tag{2.3b}$$

The spectrum and charge density distribution are plot in Fig. 2.2.

2.3.1.1 Transmission probability

In the transmission problems introduced in the last chapter, Sec. 1.2, we have assumed a 1D square potential barrier in the bulk graphene sheet. Now if we consider a narrow ribbon, the confinement from the width of the ribbon would influence the electrons' transmission probabilities through the barriers. We made simple comparisons between the energy spectrum (density of states) and the transmission probabilities of electrons corresponding to the different values of Fermi energies. The results are shown in Fig. 2.3.

2.3.2 Armchair edges

In armchair nanoribbons, the lattices are not terminated on either A or B sublattice individually near the same edge. By considering the assumption that no current has penetrated through the edges, the boundary conditions of the armchair graphene nanoribbon may be described as

$$\phi_{A(B)}(x=0) = \phi'_{A(B)}(x=0), \tag{2.4a}$$

$$\phi_{A(B)}(x=L) = \phi'_{A(B)}(x=L)e^{ik_d L}, \tag{2.4b}$$

with $k_d = \frac{4\pi}{3a_0}$.

The two valleys are mixed in the armchair nanoribbons. As a result of the boundary conditions, the criterion of the validity of the momentum vector k_x is represented by Eq. (11) or (12) in the reference [18] and is shown below.

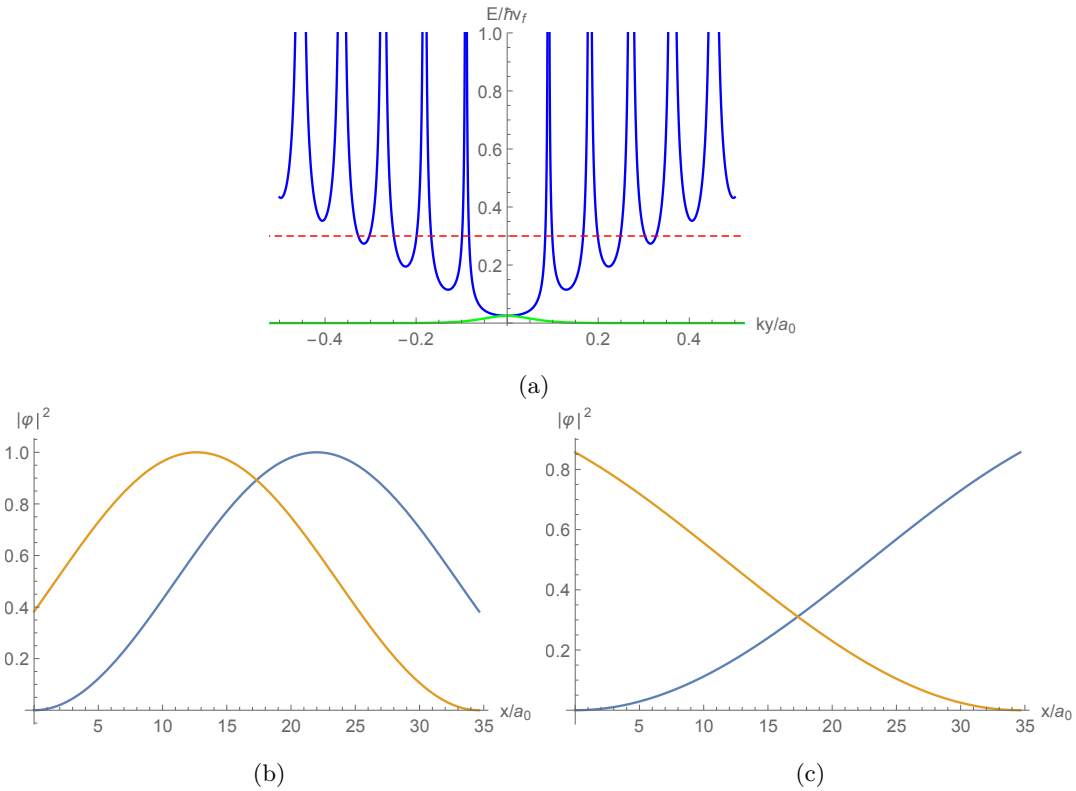

Figure 2.2: The (a) energy spectrum and (b c) the edge states in zigzag nanoribbon with the width of $35a_0$. (a) The spectrum vs k_y. The green line is the spectrum of the edge mode. The blue curves are the spectrum of the bulk states. The dashed red line is a specific position of the Fermi energy. The number of the transport channels is equal to the number of the cross points of the Fermi surface and the spectrum. (b c) The charge density distribution of (b) one bulk mode and (c) one edge decay mode chosen randomly in the ribbon. The Orange curves are the wave functions ψ_A in A sublattice while the blue one is the density of the wave function ψ_B in B sublattice. In zigzag nanoribbon, the charge density distribution on either A or B sublattice shows a smooth curve varying on space.

$$k_x = \frac{2\pi n}{2L + a_0} + \frac{2\pi}{3a_0}. \tag{2.5}$$

Note that in the armchair nanoribbons, there is no zero energy edge mode.

The spectrum and charge density distribution are plotted in Fig. 2.4.

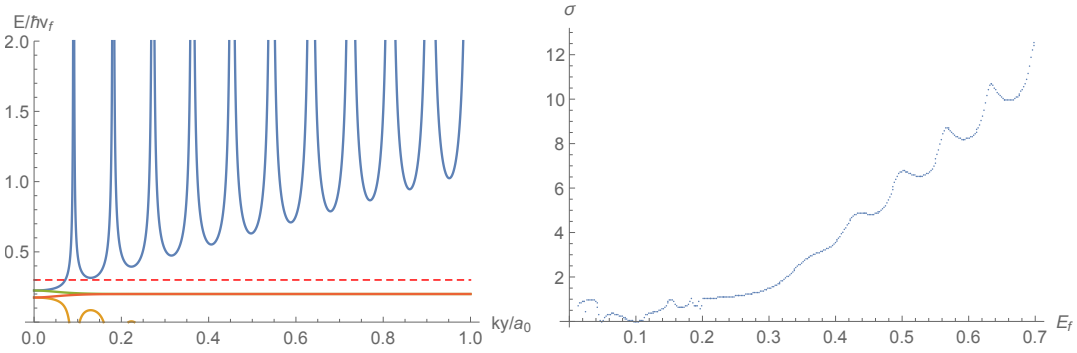

(a) (b)

Figure 2.3: The comparison between the energy spectrum (a) and the conductivity (b) in zigzag nanoribbon of graphene. (a) The spectrum is calculated of the barrier region of potential v. We have assumed this barrier region is long enough thus the states within the region can be well defined by the edge states in the barrier. (b) The precise numerical simulation of conductivity, obtained from the recursive Green's function method. Comparing (a) and (b), we noticed the characteristics: when increasing the Fermi energy, the rising of conductivity in (b) emerges when the new channels are crossed by the Fermi energy in the spectrum (a). At these positions, the density of states reach the singularities.

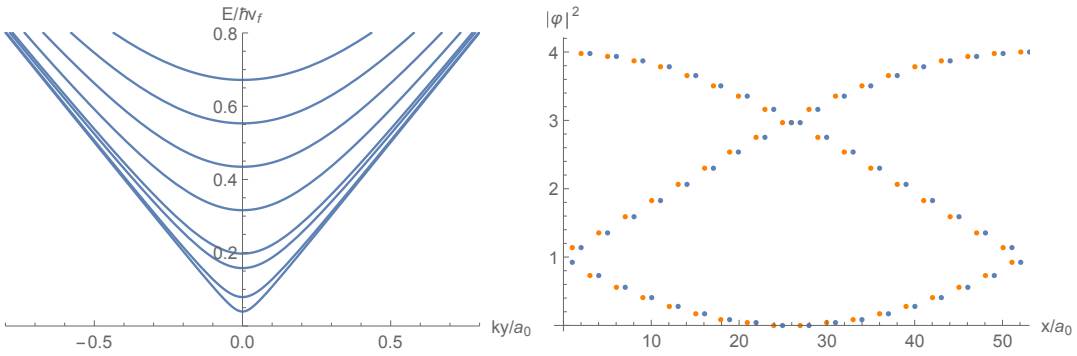

(a) (b)

Figure 2.4: The energy spectrum and edge states in armchair nanoribbons. (a) The spectrum with respect to k_y. (b) The charge density distribution of the bulk modes in the armchair ribbons. The Orange curves are the wave functions ψ_A in A sublattice while the blue one is the density of the wave function ψ_B in B sublattice. In armchair ribbons, we see a staggered image of the charge density distribution.

2.4 Edge modes in magnetic field

In last chapter 1.3, we have introduced the relationship between Quantum Hall effect and the edge states. In this chapter we looked at these edge states more carefully and we introduced the semiclassical approximation to render a more intuitive understanding. We focused on zigzag nanoribbons here.

When the magnetic field is applied perpendicular to the graphene sheet, the bulk states' Hamiltonian has the form similar to Eq. 1.8. By considering the deployment of the edges of the sample, the vector potential is chosen to be $\vec{A} = H_0(0, x, 0)^\intercal$. After Peierl's substitution[29], we obtain the Hamiltonian in the following form:

$$\hat{H} = v_f \begin{pmatrix} 0 & \hat{p}_x - \frac{e}{c}\vec{A} - i\hat{p}_y \\ \hat{p}_x - \frac{e}{c}\vec{A} + i\hat{p}_y & 0 \end{pmatrix}, \tag{2.6}$$

where $\vec{A} = H_0(0, x, 0)^\intercal$ is the vector potential of the external magnetic field. The magnetic field $H = H_0\hat{z}$ is normal to the graphene surface.

This Hamiltonian Eq. 2.6 can be solved and the analytic solutions are: [1]

$$\Psi_A = c1\mathscr{D}_{\frac{cE^2}{2\hbar v_f^2 eH}}(-\frac{\sqrt{\hbar c}k_x}{\sqrt{eH}} + \frac{\sqrt{2eH}y}{\sqrt{\hbar c}})e^{ik_x x} + c2\mathscr{D}_{-1-\frac{cE^2}{2\hbar v_f^2 eH}}(-\frac{i\sqrt{\hbar c}k_x}{\sqrt{eH}} + \frac{i\sqrt{2eH}y}{\sqrt{\hbar c}})e^{ik_x x}, \tag{2.7}$$

Where $c1$, $c2$ are random parameters. Ψ_B is obtained by substituting Ψ_A into Eq. 5.13. Because we are considering the region close to one edge $y = 0$ only, we neglect the items of the solution in Eq. 2.7 which divergent to the infinity (when $y \to \infty$). The terms left are the ones with the normalization parameter $c1$. The norm squares of the wave functions are plot in Fig. 2.5a.

Semicalassical analyses offer a more intuitive understanding of these states derived above. In semiclassical approximations, see Eq. 1.10, we treated the term in the bracket following the term of the energy E as the effective potential. I.e. $V(x) = \frac{\hbar^2}{l_B^2} + \left(\hbar k_x + \frac{\hbar y}{l_B^2}\right)^2$. We name it the effective potential because it is the potential seen from the wave function Ψ_A of A sublattice. The schematic show of the effective potential of the eigenstates corresponding to the specific value of k_x is shown in Fig. 2.5b. The parabolic potential together with the reflection wall (the red line in the Fig. 2.5b) lead to the confinements of the wave functions. The spectrum and wave functions can be estimated by semiclassical methods through Bohr-Sommerfeld quantization or WKB approximation. We have shown an example of the edge currents in armchair graphene nanoribbons, plotted in Fig. 2.6. The result is obtained

[1] The result is derived by Matej, a PhD student we have worked together.

through recursive Green's function method, the details are given in Appendix B. In the figure, the edge channels are clearly seen.

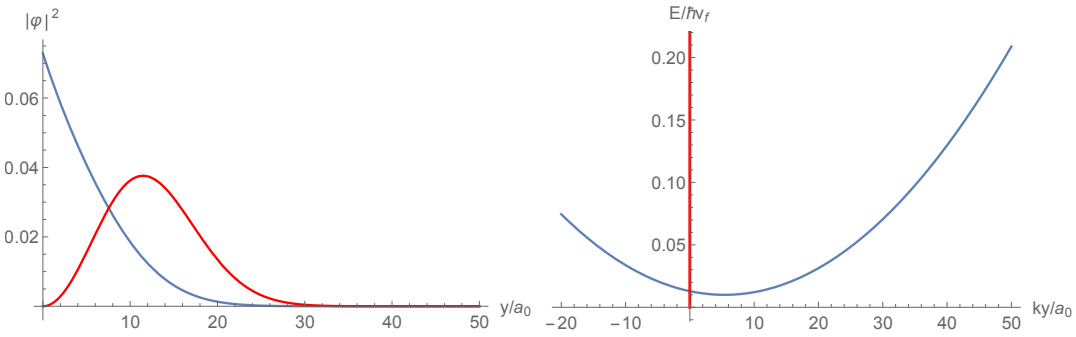

(a) (b)

Figure 2.5: (a) The norm square of the wave function $|\Psi_A|^2$ and $|\Psi_B|^2$ closing to one of the zigzag edge ($y = 0$) in the presence of an external magnetic field which is perpendicular to the graphene sheet. The red curve is the probability of charge density related to the wave function ψ_A while the blue one is of the wave function ψ_B. The Fermi energy is chose to sit in between zeroth and the 1st Landau Level. (b) The effective potential of the wave function Ψ_A in sublattice A are parabolic potential wells.

2.5 Discussion

In this Chapter, we have briefly considered the edge states in zigzag and armchair edges of the graphene sample. For the cases of more general edges, the boundaries conditions are much more complex. There can be many decayed edge modes which are not defined in Dirac Hamiltonian. [31] If we only focus on those modes which have been well described in the Dirac Hamiltonian, the appearance of the edge decay modes would depends on the angle of the edges been cut of the sample. [30, 32, 18] By the numerical simulations, we have also confirmed the prediction that the edge currents have the tendency to round the dangling defects.

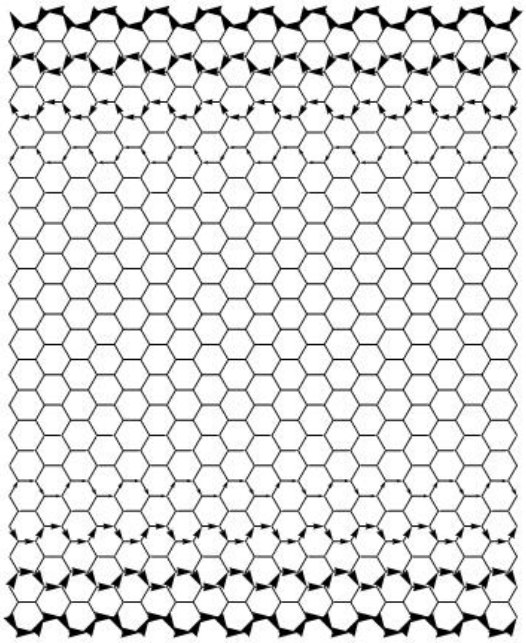

Figure 2.6: The edge channels in armchair graphene nanoribbon in the presence of magnetic field. For a given Fermi energy of the system, as shown in the figure, it is clear to see the edge channels on top and bottom edges. These edge currents transport in opposite directions without backscattering near either edge. In this figure, 3 edge channels on either boundary (top and bottom) are clearly seen. The number of the transport edge channels changes in accordance with the change of the position of the Fermi energy.

Chapter 3

Aharonov Bohm scattering

3.1 Abstract

In this chapter, we have briefly reviewed/reproduced the work of Aharonov-Bohm (AB) scattering in the region containing the magnetic flux. First we described the conventional phenomenon in the cases of Pauli Hamiltonian. Many intuitive figures are plotted showing the dependence of the scattering on the strength of the flux enclosed in the scattering region. The transmission probabilities oscillate with the period of field flux $\Delta\Phi = \Phi_0$, where Φ_0 is the flux quantum. In the following sections, we have tried to transport the same treatments to graphene. However, there are new problems there. Graphene, due to its two valleys (there are two inequivalent Dirac points K, K') property, the value of the exhibited Berry phase of its Dirac fermions is π in each single valley [34]. Therefore we have suspected that the period of the AB effect in graphene may become half of the value of the cases with Pauli Hamiltonians. However, the periodicity turned out to be the same as the conventional cases after brief calculations. The boundary conditions at the edges of the scattering region are big problems. We simply used some coarse assumptions to reveal the fundamental properties of AB effects. To extract basic knowledge from the configurations and avoid the analytic difficulties sticking to the boundary conditions, we performed numerical calculations through recursive Green's function method. For an instance, we checked the transport situations in nano-disks and rings. The conductivity obtained in these structures showed clear quantum oscillation behaviors. Attempts from other approximations are also made in this chapter and several animations are plotted for clarity. The readers may skip those less important trials and jump to the last section 3.6 regarding the results of this chapter.

3.2 Introduction

A moving electron in an external magnetic field picks up a phase associated with its trajectory. When the trajectory of the electron or quasiparticle closes a loop, the integrated change of the phase associated with the particle's wave functions is in commensurate with the flux of the field enclosed inside the loop. In year 1959, Aharonov and Bohm claimed a new pure quantum phenomena, that is, even if the trajectories of electrons are not in the region of the magnetic field, the same phase changes persist and are commensurate with the flux enclosed within the loop of the trajectory. In their original work, they calculated the scattering of an incident beam on a zero-radius magnetic field flux and gave the formula of the scattering cross-section. The periodic behavior with respect to the flux strength was evidently predicted. [35] The phenomenon are interpreted from simple reasons: In the region where the field strength has been vanished, though the physical magnetic field is zero, the gauge field - the vector potential is not the same zero. The Aharonov-Bohm effect has been confirmed by experiments.

3.3 A review of Aharonov and Bohm's work

In the presence of an external magnetic field perpendicular to the surface of the material, Scrödinger's equation containing the vector potential has the form (written in polar coordinates):

$$[\frac{\partial^2}{\partial r^2}+\frac{1}{r}\frac{\partial}{\partial r}+\frac{1}{r^2}(\frac{\partial}{\partial\theta}+i\alpha)^2+k^2]\psi=0, \tag{3.1}$$

where k is the wave vector of the incident particle and $\alpha=-e\phi/c\hbar$.

Using the boundary conditions that the wave functions are convergent at the scattering centre ($R=0$), the general solutions given by Aharonov and Bohm are shown below:

$$\psi=\sum_{m=-\infty}^{\infty}a_m J_{|m+\alpha|}(kr)e^{im\theta}, \tag{3.2}$$

where $a=(-i)^{|m+\alpha|}$. [36]

The asymptotic behavior of Eq. 3.2 at large radius R is:

$$\psi\rightarrow e^{-i(\alpha\theta+r'cos\theta)}+\frac{e^{ir'}}{(2\pi ir')^{\frac{1}{2}}}sin\pi\alpha\frac{e^{-i\theta/2}}{cos(\theta/2)}. \tag{3.3}$$

3.4 Scattering on cavity

3.4.1 Plane waves result

Bessel functions have been used to describe the scatterings on cavity. First expanded the wave function Eq. 3.2 in series of Bessel functions, then we used the boundary conditions that the wave functions vanish at the edge of the scattering cavity. The resulting wave function becomes:

$$\psi = \sum_{m=-\infty}^{\infty} \left(J_{|m+\alpha|}(kr) - \frac{J_{|m+\alpha|}(kr)}{H_{m+\alpha}(kr_0)} H_{m+\alpha}(kr) \right) a_m e^{im\theta}, \tag{3.4}$$

where r_0 is the radius of the cavity and α is the number of flux quantum. The transformation of the wave functions can be done because Hankel function (or Bessel function of the 3rd kind) $H_{m+\alpha}$ is itself also a solution of the regarded Schrödinger's equation 3.1.

In Fig. 3.1, we have shown the charge density distribution and the current of the different values of magnetic flux.

3.4.2 Wave packet approximation

Single electron's semiclassical trajectory is described through wave-packet approximation. Gaussian functions are adopted here to display the single electron's scattering on cavity:

$$\psi = \frac{1}{\delta\sqrt{2\pi}} \exp\left[-\frac{(x-x_0)^2}{2\delta_x^2} - \frac{(y-y_0)^2}{2\delta_y^2} + Ik_x x + Ik_y y \right], \tag{3.5}$$

where we have parameters δ to describe the size of initial wavepacket. For the sake of simplicity, we set $\delta_x = \delta_y = \delta$ regarding to a circular symmetric wavepacket. The simulated results are shown in Fig. 3.2. The periodic behaviors are clearly seen.

3.5 AB Scattering in graphene

3.5.1 Maths work

The Hamiltonian of graphene's Dirac fermions in the presence of the magnetic field is (in polar coordinates):

$$H = v_f \begin{pmatrix} 0 & -i\hbar e^{-i\phi}\frac{\partial}{\partial\rho} - \hbar\frac{e^{-i\phi}}{\rho}\frac{\partial}{\partial\phi} + \frac{ie\phi}{2c\rho}e^{-i\phi} \\ -i\hbar e^{i\phi}\frac{\partial}{\partial\rho} + \hbar\frac{e^{i\phi}}{\rho}\frac{\partial}{\partial\phi} - \frac{ie\phi}{2c\rho}e^{i\phi} & 0 \end{pmatrix}. \tag{3.6}$$

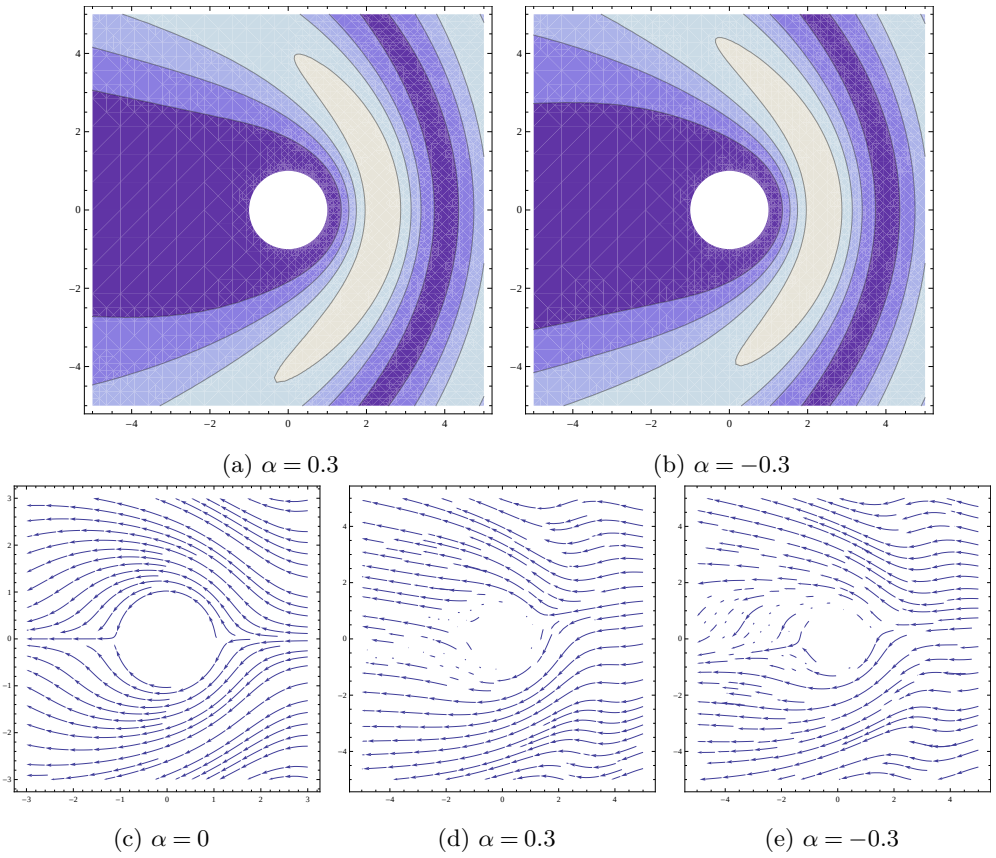

(a) $\alpha = 0.3$ (b) $\alpha = -0.3$

(c) $\alpha = 0$ (d) $\alpha = 0.3$ (e) $\alpha = -0.3$

Figure 3.1: Plane wave scattering on cavity with flux constraint inside the cavity. (a b) Contour plot of the electron density distribution and (c d e) the current with representative values of the magnetic flux in the cavity. $\alpha = \phi/\phi_0$ is the ratio the magnetic flux of the flux quantum.

The magnetic flux $\phi\hat{z}$ is normal to the surface of graphene. In symmetric gauge, the vector potential of the applied magnetic field has the components $A_\phi = \frac{\phi}{2\rho}$, $A_z = A_\rho = 0$. It leads to a pair of coupled equations:

$$v_f(-i\hbar e^{-i\phi}\frac{\partial}{\partial\rho} - \hbar\frac{e^{-i\phi}}{\rho}\frac{\partial}{\partial\phi} + \frac{ie\phi}{2c\rho}e^{-i\phi})\Psi_B = E\Psi_A, \tag{3.7a}$$

$$v_f(-i\hbar e^{i\phi}\frac{\partial}{\partial\rho} + \hbar\frac{e^{i\phi}}{\rho}\frac{\partial}{\partial\phi} - \frac{ie\phi}{2c\rho}e^{i\phi})\Psi_A = E\Psi_B. \tag{3.7b}$$

Comparing with Scrödinger's cases, we wrote the wave functions in the following form

$$\begin{pmatrix}\psi_A\\ \psi_B\end{pmatrix} = \begin{pmatrix}a_m J_{|m+\alpha|}(kr)e^{im\theta}\\ \psi_B\end{pmatrix}, \tag{3.8}$$

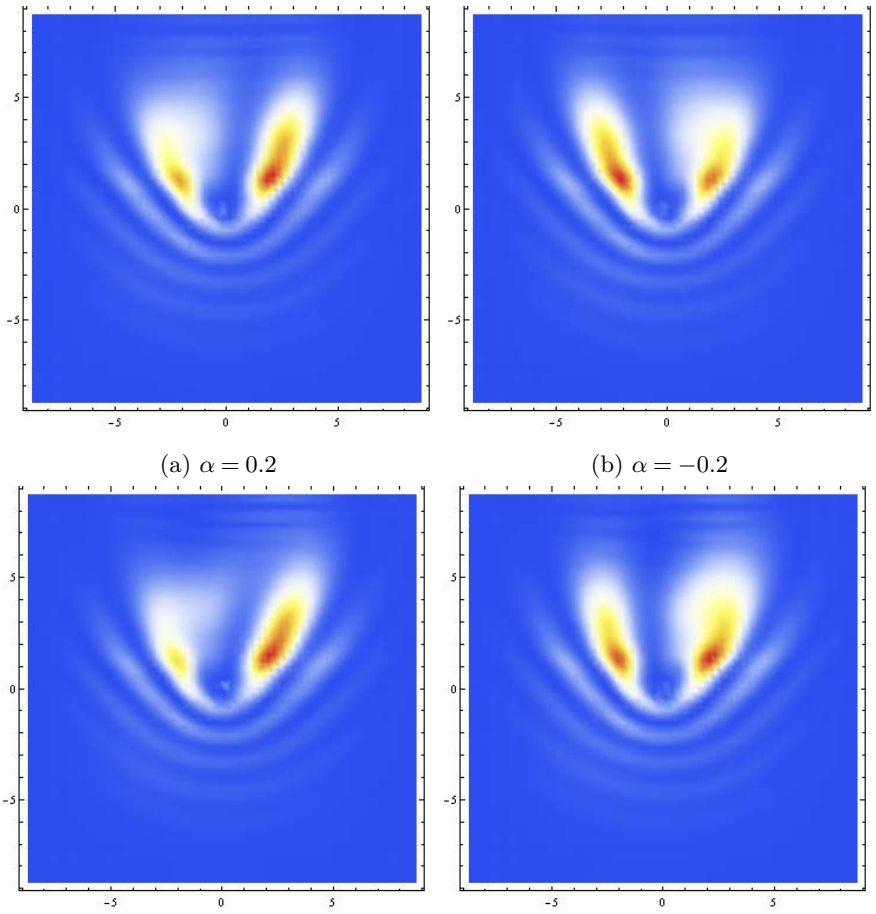

(a) $\alpha = 0.2$ (b) $\alpha = -0.2$

(c) $\alpha = 1.2$ (d) $\alpha = 0.8$

Figure 3.2: Wavepacket simulation of different values of flux in unit of flux quantum. α is the magnetic flux which is equal to $\alpha = \phi/\phi_0$, ϕ_0 is the magnetic flux quantum. The period behaviors are displayed clearly with a period of $\alpha = 1$.

where

$$\psi_B = -\frac{i}{2k\sqrt{\rho}}\left(k\rho J_{-1+|m-\alpha|}(k\rho) - 2(m-\alpha)J_{|m-\alpha|}(k\rho) - k\rho J_{1+|m-\alpha|}(k\rho)\right). \tag{3.9}$$

Should notice that, unlike Schrödinger's cases, in this assumption the wave function does not converge to finite values at origin ($R = 0$), instead it diverges to a singularity. Now let us consider a cavity with finite radius. The assumed wave functions, Eq. 3.8, satisfy the following properties: 1) It describes a plane wave of an incident electron from the right infinity ($\theta = 0$); 2) Its asymptotic behavior converges to the same form of standard

scattering function $(e^{ikx} + f(\theta)e^{ikr}/r)$ (here the normalization parameter is $\sqrt{r}$ for the case of 2D instead of 3D). Naively, if we simply define the boundary condition as $\psi_A = 0$ (i.e. the wave function vanish in one sublattice at the edge), the scattering wave functions have been derived from this boundary condition and the images are plotted in Fig. 3.3

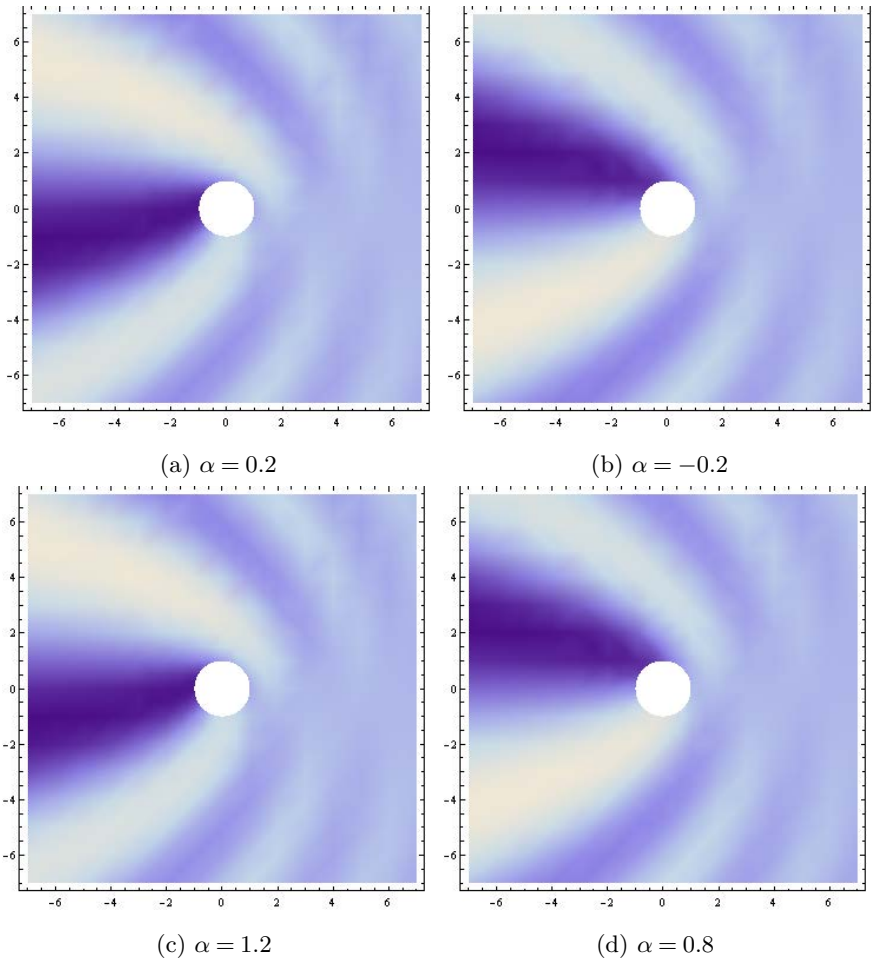

(a) $\alpha = 0.2$ (b) $\alpha = -0.2$

(c) $\alpha = 1.2$ (d) $\alpha = 0.8$

Figure 3.3: Dirac formed plane waves scattering on the cavity. The magnetic field is constrained within the cavity. $\alpha = \phi/\phi_0$ is the ratio the of the magnetic flux to the flux quantum. In these figures, the boundary conditions used are $\psi_A = 0$ at the edges of the cavity.

3.5.2 Definition of scattering cross-section

The general form of the wave functions in scattering model has an asymptotic behavior:

$$\Psi = \Psi_{inc} + \Psi_{scatt}, \tag{3.10}$$

where Ψ_{inc} is the incident beam and $\Psi_{scatt} = \binom{\psi_{A'}}{\psi_{B'}} \frac{e^{ikr}}{\sqrt{r}}$ is the scattered component. The scattering cross-section is therefore defined as the equation below:

$$\sigma = |f(\theta)|^2 = f(\theta)^+ f(\theta), \tag{3.11}$$

where $f(\theta) = \binom{\psi_{A'}}{\psi_{B'}}$.

3.5.3 Mass gap

In Schrödinger's case, the potential barrier plays the role of annihilating edges preventing the wave functions form penetrating into the classical forbidden region. For the Dirac fermions in graphene, mass gaps are able to work as the forbidden boundaries. But the inadequacy is: the mass gap itself brings into polarizations to the wave functions. For an instance, there will be two antisymmetric forms of the mass gaps:

$$V_m = \begin{pmatrix} \Delta & \\ & -\Delta \end{pmatrix} \qquad \text{or} \qquad V_m = \begin{pmatrix} -\Delta & \\ & \Delta \end{pmatrix} \tag{3.12}$$

and they are not the same. The demonstrations of scattering on the different obstacles are plotted in Fig. 3.4

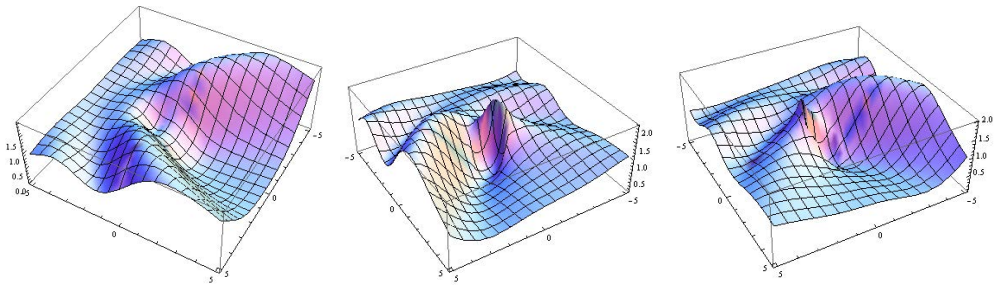

(a) (b) (c)

Figure 3.4: The 2-spinor plane waves' scattering on cavities. There is no magnetic field in these cases shown in the figures. (a) The incident plan waves scatter on a potential barrier, (b) on a mass gap describing by the matrix $diag(+m, -m)$ and (c) on the mass gap describing by the matrix $diag(-m, +m)$.

3.5.4 1st Born approximation

The wave function in the 1st Born approximation is

$$\Psi = \Psi_{in}(r) + \int d^2r' G_0(r-r')V(r')\Psi(r'), \tag{3.13}$$

which is a general solution of the Hamiltonian $(\Delta + k^2)\Psi = V(r)\Psi(r)$. [2, 3]

The Green's function is simplified to the following form as derived in the ref [37]:

$$lim_{r\to\infty} G_0(r,\omega) = \frac{1}{4\pi^2}\int d^2k \frac{e^{ikr}(\omega I + v_F k\sigma)}{\omega^2 - v_F^2|k|^2} \sim \frac{i\omega r/v_F}{v_F^2\sqrt{2pi\omega r/v_F}} \begin{pmatrix} 1 & e^{i\theta} \\ e^{-i\theta} & 1 \end{pmatrix}. \tag{3.14}$$

In our cases with the presence of magnetic fields, the perturbation potential has the form:

$$V(r) = \begin{pmatrix} 0 & -\frac{\alpha}{r}e^{i\theta} \\ \frac{\alpha}{r}e^{i\theta} & 0 \end{pmatrix}. \tag{3.15}$$

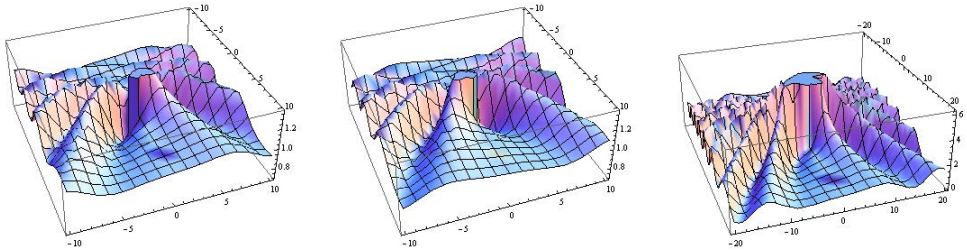

(a) $\alpha = 0.1$ (b) $\alpha = -0.1$ (c) $\alpha = 1.1$

Figure 3.5: The probability distribution of the electrons scattering on a circular region with magnetic flux inside. The estimations are obtained from the 1st Born approximation.

The results of the 1st order Born approximation are plot in Fig. 3.5.

3.6 Quantum surface interference devices: nano-disks & rings

The structure of a graphene nano-ring is shown in Fig. 3.6a. We have applied a magnetic field out of paper on these flakes. In the specific configuration, the magnetic field is non-zero only within the hole of the ring. The electrons traveling in the arms round the hole gain different phases from the non-zero vector potential of the applied magnetic field. The transmission probability resulted from the interference of the electrons' wave functions passing

different paths. In these figures. 3.6, we show results of the transmission probability and the local density of states (LDOS) which are calculated numerically. The Aharonov-Bohm effect is clearly seen in these quantum surface interference devices (QSID). The transmission probabilities of the incident electron beams with fixed Fermi energy are shown in Fig. 3.7. Landau-Buttiker formalism is used in calculating the quantum transport probability. To estimate the temperature dependence of the conductivity of these nano-devices, we have used Fermi-Dirac distribution.

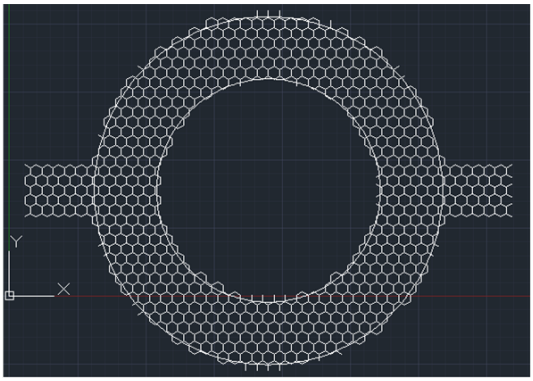

(a)

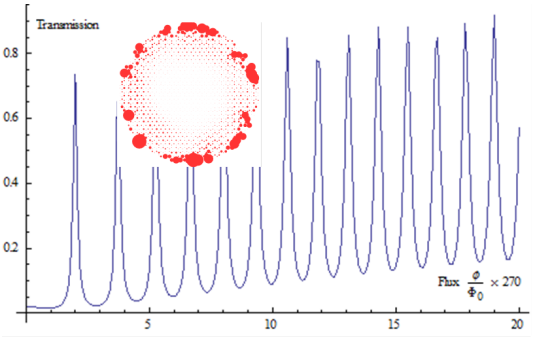

(b)

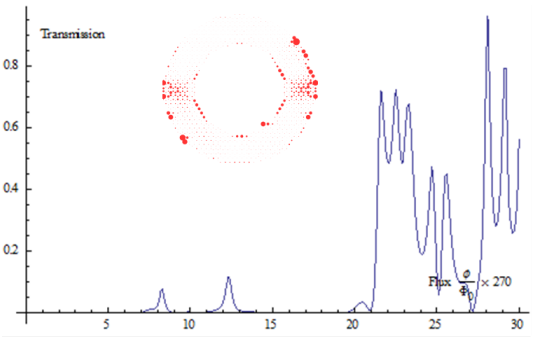

(c)

Figure 3.6: (a) A graphene nano-ring. The two leads are deployed in zigzag direction. (b) The dependence of the transmission coefficient through a graphene nano-disk of radius about 2-4 nm on the magnetic flux normal to the disk plane. The incident wave has an energy about 0.1t, where t is the hopping integral. The practical value of t is approximately equal to 3ev. Insert figure: Local density of states (LDOS) of the nano-disk. The magnetic flux of the whole disc area is $\sim$ 30 flux quanta. (c) The dependence of the transmission coefficient on magnetic flux normal to the graphene nano-ring of radius of 3 nm. The electrons have the same incident energy 0.1t. We see clearly here the Aharonov-Bohm oscillations.

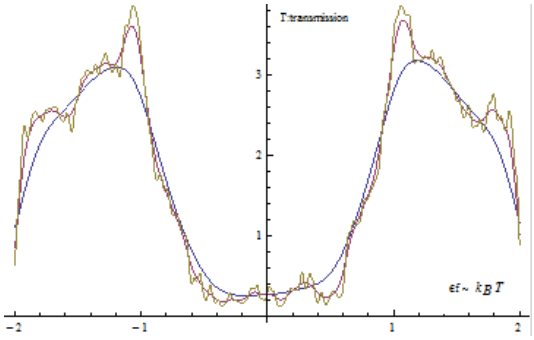

Figure 3.7: The transmission through a graphene nano-disk (Fig. 3.6a) vs the Fermi energy of the system. The brown, red and blue lines represent the measurement of the transmission probabilities at different temperatures of 100K, 300K, 1000K respectively. These results are calculated numerically and Fermi-Dirac statistics are used.

3.7 Discussion

In graphene, the boundaries of the cavity have not been accurately solved in analytics. In this chapter, we have tried several approximations and assumptions. On the edges of the cavity in graphene, the boundary conditions vary along the edge. As a consequence, we cannot say by ease that the wave functions vanish on either A or B sublattice individually at the edges. Maybe the cavity with special shape such as the hexagonal edges can be analytically solved. For a critical case, assuming there is a scattering region enclosing magnetic flux in its inner area. If the radius of this scattering region shrinks to zero, the case become similar to the configurations in Aharonov and Bohm's original work [36]. The wave functions of the graphene's Dirac Hamiltonian will diverge to singularities at the scattering center. However, in our numerical simulations, the boundaries are described accurately. The Aharonov-Bohm effect has been clearly demonstrated through the numerical calculations. The transmission probabilities show the oscillation behaviors with respect to the changing of the magnetic field or the Fermi energy. The periods of the oscillations are commensurate to the periodicity of the magnetic flux within the sample having integer numbers of the flux quantum. At the beginning of this chapter, I had thought there may be possibilities of seeing the conductivity oscillating with periods related to half integer of the flux quantum instead of the integer values. Whether the π property of the berry phase in graphene has influenced the AB effect or not is still a puzzle to me. At least, we know it contributes to the weak localization (WL). Resulting from the π Berry phase, besides localization effect, the graphene ribbon can show the anti-weak localization effect (AWL) in proper conditions[34].

Chapter 4

Magnetism[1]

4.1 Abstract

We describe new quantum oscillations in the magnetization of graphene flakes that are induced by magnetic fields which depend on the shape of the flake. At small values of the field they are due to the Aharonov-Bohm effect and with increasing field they are transformed into dHvA oscillations. The specific form of the dHvA oscillations is analyzed in terms of their energy spectrum, which has a form of Hofstadter's butterfly. Numerical results using a lattice tight-binding model and a continuum Dirac equation are presented and compared. We discuss possible experiments to investigate the quantum oscillations in Moiré and graphene anti-dot superlattices.

4.2 Introduction

Graphene has unique electrical properties manifest in its high transport mobility for electrons and holes, optical absorption and quantum resistance and capacitance [38]. This has stimulated work to identify and apply the special electronic properties in graphene-derived materials [39, 38]. An extraordinary advantage of graphene over all other materials is that its unique quantum coherent characteristics (quantum resistance, capacitance and Hall effect) can be observed even at room temperature [40, 38]. The electrical transport and other associated properties of graphene in magnetic field have also been widely studied, both in the context of the Klein tunneling [41] and in Quantum Hall effect [42].

[1]The research in this chapter is done by cooperating with another PhD student Matej Brada. I did most of the numerical simulations in the sections 4.4 & 4.5 and partially the analitic calculations in the section 4.3.

The ongoing research in graphene in strong magnetic fields has already revealed a clear evidence for Shubnikov-de Haas oscillations (SdH) of the electrical resistance [43]. These reveal new feature of the SdH oscillations in graphene such as a novel phase inversion that has been observed with increasing dc bias where the oscillation maxima develop into minima and vice versa when dc bias increases. However, the similar oscillations in the magnetization, De Haas-Van Alphen (dHvA) effect, have not been studied yet although they should also exist. The dHvA oscillations usually have the same origin associated with the energy spectrum in magnetic field. In the present paper we find a series of new dHvA effects that can related to the shape of the small graphene flakes and can be associated with the formation of boundary-specific edge currents. Observation of these features as well as the resolution of the full energy spectrum for very small graphene flakes as discussed in this paper, requires extremely large magnetic fields[44]. Recently it was shown[45] that the scalable growth of aligned single crystalline graphene flakes on commercial copper foils is possible. Thorough characterization of these flakes reveals their uniform structural and electronic structures. The flakes are formed on a copper substrate randomly and have nearly the same shapes and can be made of different sizes, of the order of nanometers or larger (how large). Such arrays consisting of thousands or millions of very similar small flakes may be an ideal system to observe the predicted effects which can be seen in the accessible magnetic field. Such flakes may be also ideal building blocks for large-scale layered heterostructures with angle-tunable optoelectronic properties[46, 47].

The effects described here may also be relevant to experiments on graphene on a hexagonal boron nitride (hBN) substrate [48]. Since hBN has a small lattice mismatch with graphene, moiré patterns emerge. These patterns show that the hBN generates a superimposed periodic potential, which significantly changes its energy spectrum. The energy spectrum gains two secondary electron-hole symmetric Dirac points [49]. The Ref.[48] describes some fundamental transport features at zero-energy and high-energy Dirac points induced by the moiré potential. Both, *ab initio* simulations and calculations in the framework of tight binding model were used. Three different moiré patterns were considered, corresponding to rotation angles of 7°, 11°, and 21° between graphene and hBN lattices. Moiré patterns create a lattice with significantly larger unit cells than that of pristine graphene, lowering the magnetic field requirement discussed above to achievable values.

Alternatively, the effects discussed in this paper may also be accessible to experiments on ultracold atoms in an optical lattice [50]. The analog to the Lorentz force can be created artificially, using one of the many possible methods (using Coriolis force arising in a rotating atomic gas [51, 52] or inducing Berry's phase by Raman lasers [53, 54]). In the Ref.[50] optical lattice is used to generate large tunable homogeneous artificial magnetic fields. While the lattice with ultra-cold atoms is maintained with standing wave produced

by lasers, the artificial magnetic field is generated by running beam lasers. These running wave lasers induce hopping in the optical lattice with a spatially dependent complex tunneling amplitude. This means that an atom hopping around a closed loop will gain a phase, which mimics an Aharonov-Bohm phase. This additional phase imposes a tunable magnetic field-like restriction on the atoms. The "artificial" magnetic field in such systems may be strong enough to obtain the unit flux quanta per elementary plaquette of the optical lattice.

The magnetization of normal metals comes conventionally from two contributions: the electron spin (Pauli paramagnetism) and orbital motion (Landau diamagnetism). The Pauli magnetization found in graphene is normally much smaller than the orbital one [55] and in the present paper we consider only the diamagnetic magnetization. The electronic properties of graphene can be described thoroughly by tight-binding model [56] or with the use of effective mass or (k,p) method resulting in two-dimensional Dirac equation [1, 57]. These two methods are very complementary and give consistent results, assuming the system is very large and the magnetic field used is small. In this case, when the contribution of the edge states is not very crucial, the low energy spectrum in the region of Dirac cone obtained by both methods is almost equivalent. Then the orbital diamagnetic magnetization has a direct relationship with the Landau-quantized bulk energy spectrum. When magnetic field is applied, the energy spectrum is quantized and discrete Landau Levels(LL) appear. The density of states is then a delta function arising at each Landau Level and at zero temperature the magnetization can be estimated by summation over the occupied energy levels, i.e. located below the Fermi energy. Each energy level rises as the magnetic field increases, while electron population shifts from highest energy occupied level to the next lower one every time when the energy of a Landau Level passes through the Fermi energy. This will result in oscillation of magnetization.

In this paper, we estimate the magnetization of graphene flakes of various shapes in large fields using the solutions of Dirac equation and the tight-binding model. In the next sections we will discuss the influence from boundary conditions and discuss the consequences for magnetization oscillations for graphene flakes having different shapes.

4.3 Dirac equation

Dirac equation describing the electron spectrum in graphene is derived by the asymptotic approximation of graphene's single electron's energy spectrum around the so-called Dirac points, i.e. with the use of the (k,p) method. Then the spectrum of elementary electronic excitations in graphene may be obtained with the use of the following Dirac Hamiltonian:

$$\hat{H} = v_f \begin{pmatrix} 0 & \hat{p}_x - i\hat{p}_y \\ \hat{p}_x + i\hat{p}_y & 0 \end{pmatrix}, \tag{4.1}$$

where $v_f = 10^8 \text{cm s}^{-1}$ is Fermi velocity and $\hat{p}_{x,y}$ are momentum operators in x, y directions. The introduction of magnetic field can be obtained by the Peierl's substitution $\hat{p} \to \hat{p} - \frac{e}{c}\vec{A}$ [29]. This results in the modified Hamiltonian of the form

$$\hat{H} = v_f \begin{pmatrix} 0 & \hat{p}_x - i\hat{p}_y - \frac{e}{c}\vec{A} \\ \hat{p}_x + i\hat{p}_y - \frac{e}{c}\vec{A} & 0 \end{pmatrix}, \tag{4.2}$$

where $\vec{A} = H_0 \begin{pmatrix} -y \\ 0 \\ 0 \end{pmatrix}$ is the vector potential giving the magnetic field, $H = H_0\hat{z}$ normal to the surface. This Hamiltonian gives a pair of coupled Dirac equations

$$v_f \left(\hat{p}_x - i\hat{p}_y + \frac{e}{c}H_0 y\right)\Psi_B = E\Psi_A, \tag{4.3a}$$

$$v_f \left(\hat{p}_x + i\hat{p}_y + \frac{e}{c}H_0 y\right)\Psi_A = E\Psi_B. \tag{4.3b}$$

We seek a solution in the form $\Psi_A(x,y) = e^{ik_x x}Y(y)$. Making this substitution into the Dirac equations, (5.13) results in a formula, which has the same form as an equation for quantum oscillator:

$$Y''(y) + \frac{1}{\hbar}\left[\frac{E^2}{v_f^2} - \frac{\hbar^2}{l_B^2} - \left(\hbar k_x + \frac{\hbar y}{l_B^2}\right)^2\right]Y(y) = 0, \tag{4.4}$$

where $l_B = \sqrt{\frac{\hbar c}{eH_0}}$ is the magnetic length.

Such harmonic oscillator has a discrete energy spectrum:

$$E_n^{e,h} = \pm v_f \sqrt{2n\frac{e\hbar H_0}{c}}, \tag{4.5}$$

where the index e refer to positive electron part of the spectrum while the index h refer to holes part of the spectrum.

Imagine that the graphene is electronically doped. The doped electron density can be estimated with obtained energy spectrum as a difference between electron and hole densities, $n_e - n_h$. Then, using the methods of statistical mechanics we obtain that the charge density in graphene is equal to:

$$n_e - n_h = \frac{2eH}{hc}\sum_{n=0}^{+\infty}\left(\left[e^{(E_n^e-\mu)/T}+1\right]^{-1} - \left[e^{(E_n^e+\mu)/T}+1\right]^{-1}\right), \tag{4.6}$$

where μ is the chemical potential. When temperature T is close to 0, this charge density (the difference $n_e - n_h$) is equal to either n_e or $-n_h$ only, depending on the nature of the electron or hole type doping. The Landau filling factor is equal to $\lambda = (n_e - n_h)hc/(2eH)$, which reflects the ratio of the number of particles per elemetary flux quanta. With the change of magnetic field, the chemical potential is sweeping past Landau Levels $E_{[\lambda]}$. At zero temperature, the magnetization can be calculated from the sum of all energy levels below Fermi energy $M = -\sum \partial E/\partial H$. Therefore, we can intuitively surmise that every time when the Landau filling factor changes by integer, the magnetization changes and may result in periodic oscillations. This suggests a set of peaks at positions of the value of magnetic field:

$$\frac{1}{H_\lambda} = \lambda \frac{2e}{n_e hc} \quad \text{or} \quad \Delta\left(\frac{1}{H_\lambda}\right) = \frac{1}{H_{\lambda+1}} - \frac{1}{H_\lambda} = \frac{2e}{n_e hc}, \tag{4.7}$$

when λ is integer. Equation (4.7) may also be written in another form $\Delta(\frac{1}{H_\lambda}) = \frac{2\pi e}{\hbar c S_f}$ by considering $n_e = \frac{S_f}{2\pi^2}$, where S_f is the area of the Fermi surface. [2] The symmetrical energy spectrum describing the charge neutrality point(CNP) results in symmetric magnetization-magnetic field curve, i.e. there is no difference of magnetization between hole and electron doping as there is no difference between hole bands and electron bands if $n_h = n_e$. There are more detailed research through Lifshitz-Kosevich approach in Ref.[58, 59].

4.4 Tight-binding Model for graphene flakes

The tight-binding model is usually derived by assuming that electrons have tunneling amplitudes between orbitals on neighbouring atom sites. These hopping processes are described by the Hamiltonian:

$$H = \sum_{<i,j>} t_{ij} c_i^\dagger c_j + h.c., \tag{4.8}$$

where the operator $c_i^\dagger$ creates a spinless electron on the site i while c_j - destroys a spinless electron on the site j. The matrix $||t_{ij}||$ describes the hopping overlapping integrals. With magnetic field, an additional phase is added to each matrix element, t_{ij}, through Peierls substitution,

$$t_{ij} \to t_{ij} e^{\frac{2\pi}{\Phi_0}\int_{r_i}^{r_j} \vec{A}\cdot dl},$$

where $\Phi_0 = ch/e$ is an elementary flux quantum. For numerical simulations below, the magnetic flux through each hexagon has been taken in the form $\Phi = p/q\Phi_0$, where p/q is a rational number, which might be interpreted as number of cells per current vortex. For simplicity, we only consider the nearest neighbor sites' hopping integrals.

[2] From eq.(4.5), for electron band, $S_f(E_n) = 2\pi n \frac{eH}{\hbar c}$ and $n_e = Degeneracy \times No.\ of\ levels = \frac{2eH}{hc} \times n$. Then we obtain $n_e = \frac{S_f}{2\pi^2}$.

Next, we choose a convenient gauge for the vector potential associated with the magnetic field $H = H_0\hat{z}$ from the set used in the Refs.[56, 60]. Following then the Ref.[60], we obtain the same Harper equation in the form:

$$\varepsilon\psi_m^B = \psi_{m-1}^A + a_m\psi_m^A, \tag{4.9a}$$

$$\varepsilon\psi_m^A = a_m\psi_m^B + \psi_{m+1}^B, \tag{4.9b}$$

where $a_m = 2\cos\left(k_y\frac{\sqrt{3}a}{2} + 2\pi\frac{p}{q}\frac{1}{3a}\frac{x_m^A + x_m^B}{2}\right)$. Here the tight-binding wave function, $\vec{\psi}_m = (\psi_m^A, \psi_m^B)^T$, defines the probability of the electron to occupy the m-th site of A or B sublattices of the graphene and ε is an eigenvalue.

Expressing these equations in matrix form, where we display only nonvanishing elements, we obtain:

$$\begin{pmatrix} 0 & a_0 & & & & & & e^{ik_dq} \\ a0 & 0 & 1 & & & & & \\ & 1 & 0 & a_1 & & & & \\ & & a_1 & 0 & 1 & & & \\ & & & & \cdots & & & \\ & & & & a_{q-2} & 0 & 1 & \\ & & & & & 1 & 0 & a_{q-1} \\ e^{-ik_dq} & & & & & & a_{q-1} & 0 \end{pmatrix} \begin{pmatrix} \psi_0^B \\ \psi_0^A \\ \psi_1^B \\ \psi_1^A \\ \\ \psi_{q-2}^A \\ \psi_{q-1}^B \\ \psi_{q-1}^A \end{pmatrix} = \varepsilon \begin{pmatrix} \psi_0^B \\ \psi_0^A \\ \psi_1^B \\ \psi_1^A \\ \\ \psi_{q-2}^A \\ \psi_{q-1}^B \\ \psi_{q-1}^A \end{pmatrix}. \tag{4.10}$$

Below we present the dependance of the energy eigenvalues for this matrix (4.10) on magnetic flux per lattice plaquette which is measured in the units of elementary flux quanta Φ/Φ_0. The spectrum has a form of the Hofstadter's butterfly (Fig.4.1a) [61].

The gaps found in the Hofstadter's butterfly spectrum suggest clear tracks of nonlinearity in both the energy spectrum and magnetization. For example, if we replot the energy spectrum as function of electron density on the lattice versus magnetic field and draw the lines of density along the spectrum gaps, we get the Fig.4.1b. A horizontal line on this Figure corresonds to the fixed value of n/n_0. Note that other non-horizontal lines show traces of the gaps arising in energy spectrum at different values of magnetic field. Every cross between the horizontal and non-horizontal lines on this Figure corresponds to a maximum of the magnetization. As the magnetic field changes, the horizontal fixed density line passes through the sets of gaps periodically, resulting in repeated peaks and troughs of magnetization. Although there are many gap lines below the fixed density line, the turning points take place only when a new gap line is crossed.

In the low value of Φ/Φ_0 region, this fractal plot (see Fig.4.1a) is very similar to Landau quantization spectrum. The periodicity is calculated intuitively from the Wannier diagram

(see Fig.4.1b). Along the schematic line of a fixed density (see colour line), we found that the cross points satisfy the equation:

$$\frac{|n/n_0 - 1/2|}{\Phi/\Phi_0} = \frac{l}{2}, \tag{4.11}$$

where l is an integer and the value $\Phi = H_0\Lambda$ is the magnetic flux penetrating one hexagonal cell, Λ is the unit cell area equal to $\frac{\sqrt{3}}{2}a^2$ where a is the unit cell base vector. After substitution and simplification the equation is given by the formula

$$\frac{1}{H_0} = \frac{l}{2}\frac{e}{hc}\Lambda\frac{1}{|n/n_0 - 1/2|} = \frac{l}{\Phi_0|n - \frac{n_0}{2}|}. \tag{4.12}$$

n_0 is the Bloch band saturation electron density, which in our spinless case, is equal to $2/\Lambda$ (2 electrons per unit cell). The deviation of density counted from the charge neutrality point $n - \frac{n_0}{2}$ may be written in terms of Fermi surface $\frac{S_f}{2\pi^2}$. Using these equations and their substitutions, finally we obtain the equations in the very familiar form as above (see, eq. (4.7)):

$$\frac{1}{H_0} = l \cdot \frac{\pi e}{\hbar c S_f} \quad \text{or} \quad \Delta\left(\frac{1}{H_0}\right) = \frac{\pi e}{\hbar c S_f}. \tag{4.13}$$

From the Figure.4.1a, it is evident that gaps refer to the lines with odd index l. In other words, 2 lines with one even and odd index l refer to one Landau Level.

Similarly, for large magnetic field, ie when $\Phi/\Phi_0 > |n/2n_0 - 1/4|$ (on the Wannier diagram presented in the Fig.1b this happens when the gray horizontal line passes the largest gap line), the positions of troughs satisfy the similar equation:

$$\frac{1}{H_0} = l \cdot \frac{1}{\Phi_0\left(\frac{n_0}{2} \pm |\frac{n_0}{2} - n|\right)}. \tag{4.14}$$

4.5 Graphene quantum dots

In this section, we will consider the case of circular graphene flakes of various sizes as well as flakes of different shapes. Let us assume that they represent quantum dots. If their size is of the order of hundred nanometers or smaller it is reasonable to describe them by tight binding model. However, when they will have a very large size, about μm or more we will solve the Dirac equation. In this case we have to introduce some boundary condition (e.g. hard wall where no current can penetrate the barrier). The results obtained in the framework of these two approaches for large and small quantum dots will be compared and common features will be identified.

4.5.1 General boundary condition for quantum graphene flakes

It is well known that graphene flakes (in majority cases) have only two types of boundaries having zig-zag or armchair shape. These types of boundaries can be formed on the hexagonal lattice only along a few specific directions. Because of this fact, it is possible to develop a rigorous approach to treat the electrons confined in the flakes with these boundaries. As described in Ref.[62, 63, 64], for the Dirac equation:

$$-i\hbar v_f \vec{\alpha} \cdot \nabla \Psi = E\Psi,$$

where the matrix

$$\vec{\alpha} = \begin{pmatrix} \vec{\sigma} & 0 \\ 0 & -\vec{\sigma} \end{pmatrix} \tag{4.15}$$

and $\vec{\sigma} = (\sigma_x, \sigma_y, \sigma_z)$ is vector of Pauli matrices, the general energy independent hard wall boundary conditions are restricted to the wave function spinors $\Psi = (\Psi_1, \Psi_2, \Psi_3, \Psi_4)$ defined on the sample edges by the equations

$$\Psi = M\Psi; \quad M^2 = 1; \quad \{\vec{n}_B \cdot \vec{\alpha}, M\} = 0. \tag{4.16}$$

Here M is 4×4 arbitrary Hermitian matrix and the vector $\vec{n}_B$ is a normal to the boundary. The anticommutation relationship in the last equation of (4.16) ensures that no current penetrates through the hard edges. Several valid possible forms of the matrix M are given in Ref.[62]. Now, for circularly symmetric dot, we may assume that the boundary conditions (BC) are rotationally invariant. From that we may find that there are 3 types of simple boundary conditions, which are arising from those abundant forms of the matrix M given in Ref.[62]. These BCs on the disk boundary are described by the following equations for the spinor Ψ:

$$\Psi_1 = \Psi_4 = 0 \quad \text{or} \quad \Psi_2 = \Psi_3 = 0 \quad \text{or} \quad \Psi_1 = \Psi_4, \quad \Psi_2 = \Psi_3. \tag{4.17}$$

By adoping the first of these BCs as a first possible approximation, we obtain the energy spectrum of the graphene quantum dots. The dependence of the energy levels against the radius of the disk is plotted in Fig.4.2. There we see that when the radius of the disk is very large we reproduce the conventional Landau spectrum for graphene [46, 42]. However when the radius of the disk decreases the Landau energy levels split into many levels (see the Figure.4.2). This happens because Landau Levels have very strong degeneracy. The energy levels also rise (or bend) - this is just the size quantisation effect.

Near the edge of the sample there can exist many edge states supporting charge currents. These edge levels can be associated with crossing of the bent LLs with the Fermi energy (see, for example, the crossing of the bent LLs by the red line on the Fig.4.2a). There we

present two cases when the number of edge states is equal to three (when the Fermi energy is E_{F1}) and nine (when the Fermi energy is E_{F2}). The number of the edge states in each of these cases is equal to the number of such crossings. When magnetic field increases the LLs are moved above the Fermi energy , one by one. Then the number of the edge states decreases. Each crossing of the LL through the Fermi energy corresponds to a peak in the magnetization.

4.5.2 The shape dependence for dHvA oscillations

In this section we describe the energy spectrum of a quantum dot in magnetic field with the use of tight-binding model, where the Hamiltonian is represented in a Hermitian matrix form, see Eq.(4.10). This approach allows to consider quantum dots of various shapes. There, the energy spectrum can be obtained accurately by finding all eigenvalues of the Hermitian matrix, which has a specific form for each shape. Here we present four examples of quantum dots, which have a hexagon shape, see Fig.4.3a, disk shape, see Fig.4.3b, triangular shape, see Fig.4.4a, and rhombic shape, see Fig.4.4b. Note that while the hexagon, triangle and rhombus all have only zig-zag boundary, the disk has both zig-zag and armchair ones, i.e. in this case we have to use a variable BCs. To calculate the magnetization dependence on magnetic field for these variously shaped graphene flakes (see, Fig.4.3c, 4.3d, 4.4c, 4.4d) we use the same method as given in the section 3. On these Figures, we see that the main features remain similar between the different shapes. This is a direct result of the bulk states, as each flake has the same structure and Landau Levels as inside graphene flake. However different shapes of the flakes give rise to different BCs, which produce *different edge states*. Since both, the edge states and bulk states are involved in creating this magnetization oscillations, it is important to note that at high values of Φ/Φ_0, the edge states are contributing less to the overall magnetization than the bulk states and the magnetization graphs are very similar to each other. There is however a small difference related to the size of the flakes, which is associated with some fine fractal structure inherent to the bulk. Increasing the size of the flake has exactly the same effect on dHvA oscillations, which become more and more prevalent. At low values of Φ/Φ_0, or at small sizes of the flakes, the edge states become prevalent, and there, we can see that the magnetization behaves differently for different shapes of graphene flakes. This is because of the different edge states. Note that each trough on the Figures is well described by the analytic equation (4.14). Each trough is corresponding on the Wannier diagram (see the Fig.4.3) to a cross-point between a fixed electron density horizontal line and a gap line having the filling factor slope. In this density-magnetic flux Wannier diagram for the hexagonal flake Fig.4.3e, we have systematically marked each gap line in pair numbers. The index of each line represents

the starting and ending points for this line on the y-axis. Red, green, and orange colours are used to indicate the approximate gap size from large to small. The fixed density of electrons in a system is indicated by the dashed line. In Fig. 4.3e, the position of this density line is at the position with the same charge density as in the plots of magnetization, see Figs 4.3c, 4.3d, 4.4c, 4.4d. The gray horizontal line shows the charge neutrality point. Each cross point in Fig.4.3e, which is marked by a cross, represents a pass of the Fermi surface over a gap. These cross points are also related to a trough in magnetization plot, as indicated by arrows in Fig.4.3c & Fig.4.3d. Red and green arrows are used to identify the cross points with positive and negative gap slopes, respectively. We notice there are slight mismatching between the accurately calculated values of troughs (the positions of arrows) with the troughs of the magnetization in Fig.4.3c & Fig.4.3d. This is because of the confinement effect arising on finite flakes. In Fig.4.3c, a nearly periodic oscillations are observed at low magnetic field. Their period slightly decreases when the field increases. There, the values of the magnetic flux associated with these troughs are read and marked. These oscillations are related to Aharonov-Bohm effect. Here each peak of the magnetization corresponds to an extra magnetic flux quanta penetrating the entire flake. The absorption of magnetic flux and the magnetization oscillations, associated with the edge currents, appeared due to the time reversal symmetry breaking arising in magnetic field. The spacing between neighboring oscillations is $\sim \frac{1}{N}$, where N is the total number of unit cells, see, for example, the Fig.4.3c.

4.6 Comments on Dirac Boundary Conditions at the Edges

It is very useful to make a comparison of the results obtained in the framework of tight-binding (TB) and continuum Dirac models. Note that while for the case of the TB model the boundary conditions for various flake shapes are well defined, for the Dirac equation it is not uniquely specified. The reason is that the Dirac equation is derived within the effective mass method in the continuum approximation which is, strictly speaking a system with smoothly varying potentials. The boundary of the flake does not satisfy this constraint and must be augmented with an appropriate boundary condition for the Dirac spinor at the edge.

This boundary condition depends on the orientation of the edge. One can expect that the boundary condition can be enforced, in the framework of a Dirac model, by gapping the exterior region on a large energy scale. However, this description of the vacuum is problematic. Such a gap can appear, for example, if the time reversal symmetry is broken

keeping other symmetries intact. This may be done in a way as in Haldane model for Quantum Hall Effect without LLs [65]. But the exterior region should be T-invariant, excluding this possibility. Even if we allow it, the we have two possibilities: 1) the Chern number exterior to the flake is the same is interior or 2) it is different (see the Ref.[66]). These two situations stabilize different edge state spectra.

Another possibility arises, for example, if one breaks the spatial inversion symmetry outside the flake. In essence this polarizes the external medium and allows for bound charges accumulating on the interface. If the exterior polarization is uniform, the charge accumulation on the interface has a vector anisotropy, and is clearly dependent on the orientation of the edge.

One can also gap the spectrum, retaining P and T symmetries but breaking the translational symmetry in a $\sqrt{3} \times \sqrt{3}$ superlattice exterior to the flake. This has the effect of coherently mixing the two valleys at the interface and will generically produce Friedel oscillations in the charge density interior to the flake. The phase of these oscillations can depend on the orientation of the edge. The identification of the appropriate Dirac boundary condition that describe the size and shape quantization of the lattice calculcalations in this case remains an open and interesting problem.

While we have employed both models to describe the magnetization of the graphene flakes, it is important to note the differences and similarities between these two approaches. At large values of Φ/Φ_0, both models provide very similar results. The splitting of Landau Levels in the Dirac approach creates the magnetization oscillation as Fermi surface passes through these Landau Levels. These oscillation can be clearly identified for all flakes, see the Figs4.3c, 4.3d, 4.4c and 4.4d.

At lower values of Φ/Φ_0, the dHvA oscillations are not as prominent as the Aharonov-Bohm one. This stems from the fact that Dirac equation describes best the continuum infinite graphene. To describe the edge states with the use of the Dirac equation the boundary conditions of the flakes should be put in a correspondence to some symmetry invariant manifold as we discussed above. Specifically for the flakes the vacuum around should satisfy the time reversal and space inversion invariance. With such an approach the edge states of any flake are well described in the framework of the Dirac equation, too. However, the edge states contribution to magnetisation of the small size flakes is comparable to the contribution of the bulk. The Dirac approach may give additional insights on the topological nature of these edge magnetization oscillations (see, also, for a detail, the papers on topological insulators[66, 67, 68, 69, 70]).

4.7 Discussion of possible experiments

Usually the fractal features of Hofstadter like spectrum of monolayer graphene can not be directly observed. It requires very high magnetic field, which is experimentally inaccessible. Therefore to reveal the characteristics of the energy spectrum with ratio Φ/Φ_0 of the order of 1, other experimental ideas are needed. They are briefly discussed in introduction.

One idea is to use Moiré lattices. The increase of the unit cell in such lattices can be used as a way to decrease the value of magnetic field associated with reasonable rational fractions of magnetic flux quanta, see Ref.[71]. In this paper, it was shown that a slight angle mismatch between two lattices put together forms a superlattice which has a much larger supercell size. Therefore smaller field is required to reach the value of the elementary flux quanta. Although in this case, the Moiré lattice has a triangular point , i.e. the full C_6 symmetry, the Hall and longitudinal conductivities measured there display they-self similarity and therewith their evident connections with Hofstadter's butterfly-like energy spectrum.

When we change magnetic field or the carrier density, we see that the crosspoints of the carrier's density line with the gap-lines in Wannier diagram are related to the peaks of Hall conductivity σ_{xy} and the troughs of longitudinal conductivity σ_{xx}.

The method we presented in this paper can be used to estimate the magnetization oscillations and other behavior in these Moiré lattices. The oscillations of magnetizations for Moire flakes will have similar characteristics with the examples shown in our paper.

Another, previously mentioned, experimental framework for creation of Moiré pattern is to consider aligned hBN superlattices [72, 73]. The spectrum calculated in this case is valid within $1eV$ [74] and has a truncated Hofstadter's butterfly shape which shows minibands at low fractions of the elementary magnetic flux quanta per hexagon unit cell. In this graphene-hBN configuration the prime branches of the energy spectrum are the traces of Landau Levels related to the first Dirac points (the normal Dirac points in monolayer graphene). There are also secondary Dirac points, which appear at the edges of Brillouin zone. They are related to the minibands attached to each energy branch. Interestingly, the charge density-magnetic field Wannier diagram presented on the Figure 4 of the paper [73] shows energy gaps having linear dependence on magnetic flux, which is an evidence of the existence of dHvA oscillations.

There are some other systems where the proposed effects can be observed, e.g. cold atoms [50] or graphene antidot lattice (GAL) [44]. In case of the cold atoms, the optical lattice commonly studied have a square symmetry, it could be formed into a hexagonal lattice as well. In the arrays of graphene antidots [44], a hexagonal lattice is mimicked through rhombic etched holes. The Hofstadter's butterfly energy spectrum calculated for this system

has a fine structure, which contains a lot of similarities with the monolayer graphene energy spectrum. Therefore, it is very possible to observe dHvA oscillations of magnetization in graphene antidot lattice flakes with experimentally achievable magnetic fields. Similar oscillations of magnetization may be also observed on charged nano-bubbles and nano domes, which have been recently discovered in the epitaxial graphene, see Refs.[75, 76, 77].

The inclusion of electron spins doubles the number of degrees of freedom and the number of electrons below Fermi energy. This means that the effective amplitude for magnetization will be increased (roughly double), since it is calculated by summing over all states below the Fermi energy. However, as follows from the equations (4.12,4.14), if we take into account the electron spins there will arise the Zeeman splitting and, of course, due to this splitting the periodicity of dHvA oscillations will be changed. Note that the electron-electron interaction should not also be neglected. It may have a strong influence on the ground state of quantum dots as it has been declared in semiconductor QDs in ref [78].

4.8 Conclusions

In this paper we have determined de Haas-van Alphen oscillations for quantum dots made of graphene flakes having different shapes. As an example we have focused our studies on flakes with the hexagonal, triangular, rhombic, and disk shapes and shown that they represent examples of nontrivial topological insulators. Different approaches have been used. One of them is a (k,p) method or the Dirac equation, where the period of the dHvA oscillations has been determined to be $\Delta\left(\frac{1}{H}\right)=\frac{2e}{n_e hc}$. This period has been compared with one obtained in the framework of the tight binding model, where the Hofstadter's butterfly energy spectrum has been obtained and analyzed. Both approaches have been employed equally for both graphene flakes of hexagonal and circular shapes. The flakes with triangular and rhombic symmetry were studied using the thight binding approach only. In all cases the obtained magnetization spectrum shows clear signs of dHvA oscillations, especially in high magnetic field, which appear together with Aharonov-Bohm effect clearly noticeable at low magnetic fields.

Finally, we have proposed several types of experiments where the predicted dHvA oscillations obtained in this paper might be directly observed experimentally. The described features of the fractal Hofstadter energy spectrum can be also observed optically with microwave experiments when graphene flake will be embedded in linear resonator[79]. Probably, in this case for a clear Hofstadter fractal spectral shape, high quality samples are required. Moreover, the highly concentrated gaps originated between minibands at low magnetic field may fuzz the oscillations of magnetization. The magnetization measured in graphene may be ambiguous when the density of small dHvA oscillations rises.

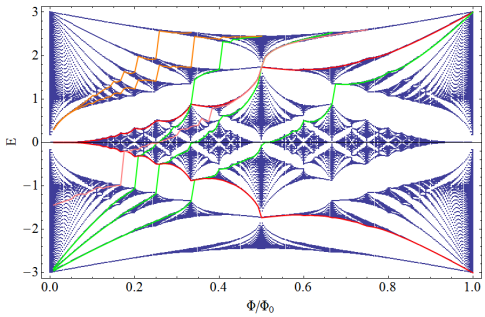

(a) Hofstadter's butterfly

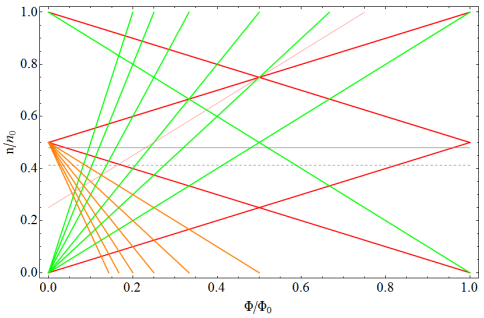

(b) Wannier Diagram

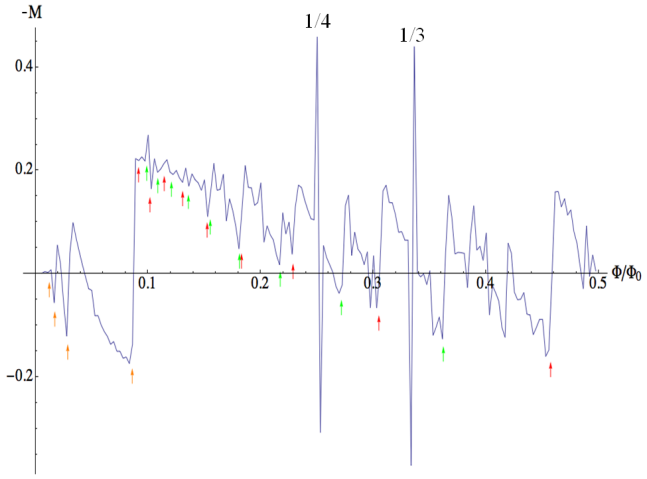

(c) Magnetization at the charge density $n/n_0 = 0.54$

Figure 4.1: (colour online) (a) Hofstadter's butterfly showing the energy spectrum evolution on magnetic flux per elementary unit cell, calculated for a hexagonal lattice of infinite size. Energy gaps can be clearly seen. Red, green and orange curves are given to indicate the approximate gap size from large to small. (b) The Wannier diagram: the linear dependence of electron density n/n_0 on magnetic flux Φ/Φ_0, given for different integer filling factors. Here n_0 is the Bloch band saturation density. There is a correspondence between each of these linear dependencies (the solid straight lines) and the "gap" curves shown on the left figure of the Hofstadter spectrum. To show this we use the same color for related curves. The half filling of the band, $n/n_0 = \frac{1}{2}$, corresponds to the Dirac point. The dashed grey horizontal line is related to a constant electron's density. (c) The dependence of magnetization $-M$ on magnetic flux Φ/Φ_0 calculated at a fixed charge carrier density for infinitely large hexagonal lattice. The magnetization is measured in units $2t/\Lambda$, where t is the hopping energy and Λ is the plaquette area. Troughs on the graph (the peaks of the magnetization) are associated with electron (hole) trajectories which are commensurate with the graphene lattice. They are related to the cross-points between the density-line (gray lines) and the gap-lines (color lines). The arrows show the positions of troughs calculated from the equations (4.12, 4.14) with several integer values of l. The most pronounced peaks in magnetisation corresponds to the flux equal to $\Phi/\Phi_0 = 1/4$ and $1/3$, here the commensurable effects are most pronounced.

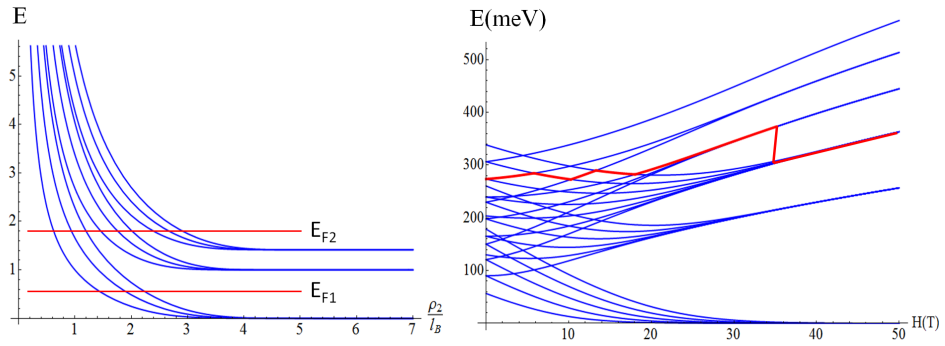

(a) Radius of the graphene flake (b) Magnetic Field

Figure 4.2: The energy spectrum of the circular graphene flake represented by our quantum dot (QD) in magnetic field. (a) We show the dependance of each energy level on the radius of the QD. Here the unit of energy is equal to $E_0 = \sqrt{2}\hbar v_f/l_B$. The radius, ρ of the circular graphene flake (our QD) is measured in the units of magnetic length l_B. When the QD radius ρ is much larger than the magnetic length l_B the conventional Landau spectrum of graphene is reproduced. When the QD radius decreases each energy level is rising and splitting due to the size quantisation. This splitting gives rise to the oscillations shown below in Fig. (4.3d). With increasing magnetic field, the Fermi surface usually sweeps through the split Landau Levels and therefore the oscillations of the magnetisation arise. Each crossed LL corresponds to a peak on the magnetization plot. As an example, we present two positions of the Fermi level schematically presented by red horizontal lines and associated with two values of electron density. The number of crossing points of the energy spectrum by each of these lines may indicate the number of edge states existing at such electron density. So for the first Fermi level we have 3 edge states, while for the second level the number of edge states is equal to 9. Note that this is schematical presentation of the edge states, which are normally discussed as a bending of LLs, see for example, Fig.1, in the Ref. [22].(b) The dependence of each energy level on magnetic field H measured in Teslas for QD with a fixed radius $R = 200a = 28$nm. Highly degenerated LLs are clearly seen in region of very high magnetic field (or small magnetic length l_B). That is consistent with the Figure (a). Here at low magnetic field there is abundance of the energy level crossings, which can bring an ambiguity to the interpretation of results of the magnetization measurements. For an illustration we also present the dependence of the uppermost filled energy level on magnetic field given by the red curve, which has saw-tooth form (for simplicity, only positive energy spectrums are shown in the figures.)

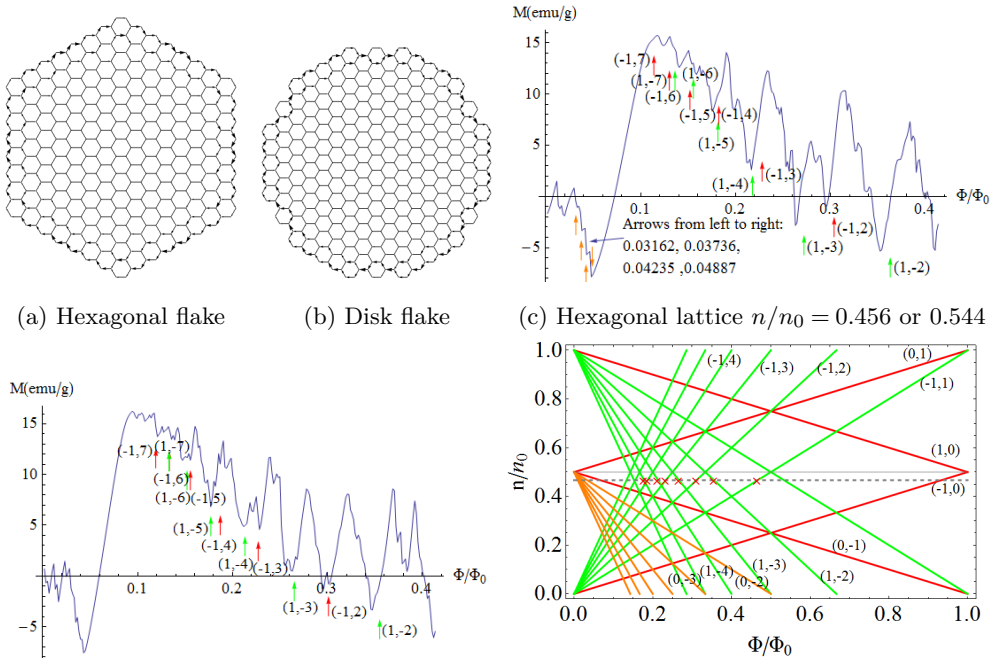

(a) Hexagonal flake (b) Disk flake (c) Hexagonal lattice $n/n_0 = 0.456$ or 0.544

(d) Dot $n/n_0 = 0.456$ or 0.544 (e) Density vs magnetic field

Figure 4.3: (a) The graphene flake having the Hexagon shape. Here only the zigzag-type boundaries exist. One may clearly see here the edge current, which was associated with some particular electronic state (b) Disk shape graphene flake has a variable boundary conditions, where both the zig-zag and armchair were employed. The energy used in (a) is $E = -1.39t$ and in (b) $E = E = -1.385t$. The flux used is $\Phi/\Phi_0 = 1/7$ for both. (c) The magnetization of the hexagon flake calculated with the use of the tight binding model. The marked troughs given in the Figures (c) and (d) correspond to the cross-points between the constant electron density-line (the dashed gray line) and the gap-lines given in color on the Figure (e). The pair numbers in the brackets relates each trough to a specific gap line. For example, an index $(1,-2)$ represents a trough referring to the cross between the dashed gray density-line with the colored gap-line marked $(1,-2)$. The index of the lines is given by their start and end point on the y-axis. The color of the line corresponds to the slope of the gap line crossed (the red color is used for the negative slope, the green color - for the positive slope). At low values of Φ/Φ_0, the Aharonov-Bohm effect is prominent. The spacing between troughs is in agreement with the estimated value of $\frac{1}{N}$, where N is the number of unit cells. (d) The calculated magnetization of the disk flake, shown in (b). The behavior observed is similar to one given in (c). (e) The Wannier diagram: The index of the lines represents the starting and ending points of the line, with 0 being the charge neutrality point and non-zero integers being the multiplications of the saturation position $(n/n_0 = 1)$. For example, if a gap-line starts from the position $(\Phi/\Phi_0, n/n_0) = (0,1)$ and ends at the position $(1,0)$, it is marked by $(1,0)$.

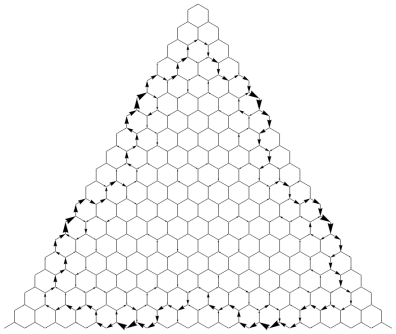

(a) Triangular lattice

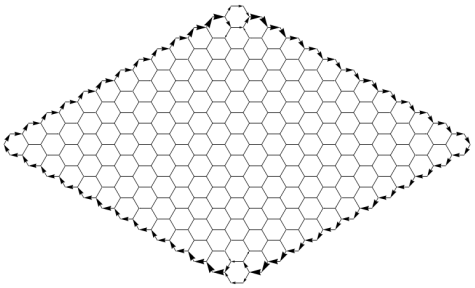

(b) Rhombic lattice

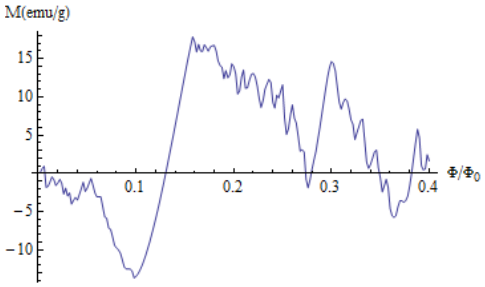

(c) Triangular lattice $n/n_0 = 0.44$ or 0.56

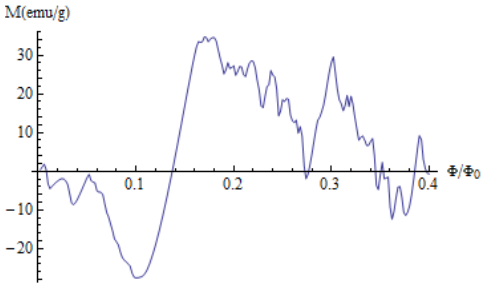

(d) Rhombic lattice $n/n_0 = 0.44$ or 0.56

Figure 4.4: (a) The graphene flake having the Triangular shape at energy $E = 2.687t$. Only the zigzag-type boundaries are present. (b) Rhombic shape graphene flake also has only zigzag-type boundaries. Here, the energy is $E = 2.05t$. The triangular and rhombic lattice have different edge states due to their non-identical boundaries. The arrows indicate the single electron current flowing on the flake. On both flakes the magnetic field was associated with the flux $\Phi/\Phi_0 = 1/7$. (c) The magnetization of the triangular flake calculated with the use of the tight binding model. (d) The calculated magnetization of the rhombic flake, shown in (b). Again, the behavior is similar to the triangular one, and to the hexagonal flake at high values of Φ/Φ_0, as expected, since bulk states are prevalent in such a case. At low values of Φ/Φ_0 however, the behavior is different for each flake, as the edge states vary from shape to shape.

Chapter 5

Magneto Elastic effect

5.1 Abstract

The stress/strain caused distortions of graphene lattices can induce a gauge field. Analogizing to a real magnetic field, the strength of this pseudo-magnetic field is mathematically related to the Gaussian curvature of the surface of the graphene sheet. With careful stretch of the graphene sheet, we may create an roughly homogeneous pseudo-magnetic field in the sheet. There are clear differences between this pseudo magnetic field and a real external field. In the case of this pseudo-magnetic field, the electrons in either of the two energy valleys of graphene in momentum space see the opposite field strength. We show, however by adding an external magnetic field, the consequence of this stress induced gauge field can be revealed. The conductivity and magnetization of the sample are expected to show the quantum oscillations which are similar to Shubnikov-de Haas oscillations (ShdH) and De Haas-von Alphen oscillations (dHvA) respectively. In rippled graphene, where the average Gaussian curvature is zero, the flat energy bands appear at zero energy states when the magnetic length is relatively smaller than the curvature radius [26, 27, 28, 23].

5.2 Introduction

Many recent research papers have shown that the strain imposed on graphene can cause similar effects as an external magnetic field [80, 81, 82]. An elastic strain can cause a distortion in graphene lattice therefore it spatially changes the hopping energy between carbon atoms. As a consequence, a gauge field may be induced from the strain, which is equivalent to a constant magnetic field, see Ref.[82]. Hence there may be LLs which are associated not with magnetic field but with the strain imposed on graphene. Therefore

on stretched graphene samples, one may observe the Landau quantization. Indeed, the predicted LLs formed due to pure strain-induced "pseudo-magnetic field" have been recently observed [83]. There, the strain was associated with the creation of nanobubbles. Analogous strain induced effects may arise in charged nanobubbles and nanodomes which have been recently revealed [76, 75]. There, the Raman spectroscopies have been used to detect and to measure the strain.

5.3 Stress/strain induced pseudo magnetic field

In graphene, an effective field induced from a 2D gauge field $u_{i,j}$ is presented in the form of [80, 82, 84, 85]

$$A_x = \frac{\beta t}{a}(u_{xx} - u_{yy}), \tag{5.1a}$$

$$A_y = -\frac{\beta t}{a}(u_{xy}), \tag{5.1b}$$

where $\beta = -\partial \ln t / \partial \ln a \simeq 2$. t is the nearest-neighbor hopping integral, a is the lattice parameter. This may imply that either a bulk or shear distortion can mimic a magnetic field in graphene flakes with the gauge potential:

$$\vec{A} = \begin{pmatrix} -By \\ 0 \\ 0 \end{pmatrix}, \tag{5.2}$$

where the magnetic field $B = B\hat{e}_z$ is aligned in the direction perpendicular to the graphene plane. In contrast with the equation (5.1), we see that an equivalent gauge potential can be created when $A_x = -By = \frac{\beta t}{a}(u_{xx} - u_{yy})$ and $A_y = 0 = -\frac{\beta t}{a}(u_{xy})$. For simplicity, we consider a uniaxial strain, where $u_{xx} = 0$, $u_{yy} = \frac{aBy}{\beta t}$. The stress and strain (the definition, see ref[86]) has the elastic relationship $\sigma_{yy} = E \cdot u_{yy}$, here E is the Young's modulus. Finally, to create the gauge potential required for Landau quantization, the associate force per transverse area $\sigma_{yy}(y)$ should be equal to

$$\sigma_{yy}(y) = \frac{EaB}{\beta t} y. \tag{5.3}$$

Therefore, to observe the oscillations of the magnetization in the graphene flakes as we have described in the last chapter Chap. 4, we needs to apply tensile stress and strain as described in this equation(5.3). If we would be able to apply such a stress (for example, if we bend the substrate plate on which the graphene is attached, then the strain will be related to the applied curvature of the substrate plate), the LLs are produced, then no magnetic field is required to observe the predicted magnetization oscillations. This is simplest example of the usage of uniaxial stress, only. Specifically, for each flake with a specific shape, different other

gauge potentials may also be designed. For example, there is a proposed strain potential in Ref.[87]. There, a graphene ribbon is bent by a non-uniform force or stress applied in plane of the ribbon, to produce a perpendicular uniform magnetic field.

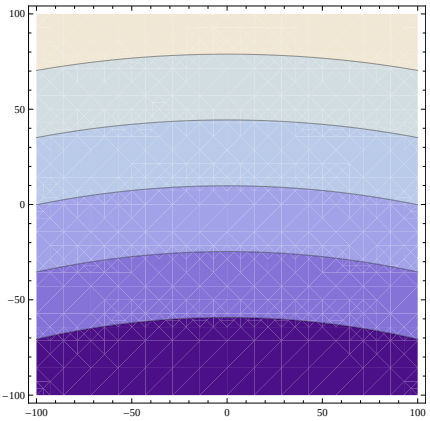

Figure 5.1: The contour plot shows the effective magnetic field of the bent graphene ribbon. The different colors show the gradient of the amplitude of the pseudo magnetic field.

In this framework, the varying force is applied over the edges of graphene ribbon. Then it is stretched in both (x and y) directions, as described in the Ref [87], see the Fig. 5.1 (or Fig. 2 in the paper). The resulting lattice distortions obey the following equations:

$$u_x = u_0 \left(2xy + \frac{f_0}{f_1} x\right), \tag{5.4a}$$

$$u_y = u_0 \left[-x^2 - \frac{\lambda}{\lambda + 2\mu} \left(y^2 + \frac{f_0}{f_1} y\right)\right], \tag{5.4b}$$

where u_0 is equal to $u_{xx}^{max}/2W$, W is the width of the nanoribbon, λ and μ are the Lamé coefficients. Here u_{xx}^{max} is the maximal strain raised in the system. The force acting along the y-edges of the sample is $F_x = f_0 + f_1 y$, where the sample is located within the area $W/2 > y > -W/2$. Here we choose $f_0 = W f_1$. The related strains are determined as:

$$u_{xx} = u_0 (2y + W), \tag{5.5a}$$

$$u_{yy} = u_0 \left[-\frac{\lambda}{\lambda + 2\mu} (2y + W)\right], \tag{5.5b}$$

$$u_{xy} = u_{yx} = 0. \tag{5.5c}$$

By substituting these expressions for strain back to the eq. (5.1), we obtain the value of the constant pseudo-magnetic field B_s, which is acting perpendicular to the graphene nano-dot.

$$B_s = c\beta \frac{2\mu \Phi_0 u_{xx}^{max}}{(\lambda + 2\mu) a W}. \tag{5.6}$$

To define the stress needed to apply to get such value of the pseudo-magnetic field we use the Hooke's Law [86]

$$\sigma_{ik} = K u_{ll}\delta_{ik} + 2\mu(u_{ik} - \frac{1}{2}\delta_{ik}u_{ll}), \tag{5.7}$$

where $K = \lambda + \mu$ is the modulus of compression and δ_{ik} is the Kronicker delta symbol. Then, using these equations we obtain the stress applied:

$$\sigma_{xx} = K u_{ll} + 2\mu(u_{xx} - \frac{1}{2}u_{ll}), \tag{5.8a}$$

$$\sigma_{yy} = \sigma_{xy} = 0. \tag{5.8b}$$

Therefore, only unilateral stress is needed to get the constant pseudo-magnetic field. Eq.(5.8a) after substitution becomes

$$\sigma_{xx} = \frac{2\lambda + 2\mu}{\lambda + 2\mu} 2\mu u_0(2y + W). \tag{5.9}$$

Note that since the stress applied depends linearly only on y-coordinate, the torque of the stretching force about one of the corner with zero force is

$$M = F \times r = \int \sigma_{xx} y dy = \frac{4\lambda + 4\mu}{3\lambda + 6\mu} \mu u_{xx}^{max} W^2. \tag{5.10}$$

The maximum stress along the sample which generates a reasonable pseudo-magnetic field without breaking the sample is estimated in Table 5.1, where for an illustration we have taken the values of the strain suggested in the Ref.[87]. Here in this estimations the width of the ribbon is equal to $W = 0.1\mu m$, and the Lamé coefficients used are taken from the report, see Ref. [88].

Table 5.1: Temperature (T), maximum strain (μ_{xx}), maximum stress (σ_{xx}), moment (M), and pseudomagnetic field strength (B_S)

T, K	μ_{xx}	σ_{xx} $(N \cdot m^{-1})$	M $(N \cdot \mu m^2)$	$B_S(T)$
0	0.05	11.47	3.83×10^{-2}	11.58
100	0.1	22.95	7.65×10^{-2}	23.67
300	0.1	23.13	7.71×10^{-2}	24.75
500	0.2	46.32	15.44×10^{-2}	50.84
1100	0.2	45.5	15.16×10^{-2}	52.36

Thus, the strain may play a role of a magnetic field in tailoring the energy spectrum and the Landau quantization. Therefore, we can suggest that the oscillations of magnetization described in the last chapter, Chap. 4 also may exist in strain distorted graphene flakes.

5.4 Valley symmetry broken

The distortions of lattice cannot break the time reversal (T) symmetry. Therefore, any T symmetry broken effects related to the stress in graphene would cancel it self. In another word, the pseudo magnetic field induced in either valley of the graphene has the same scale but opposite sign. In order to reveal the distortion induced gauge field, we need to break the valley symmetry. This can be done through many ways, such as introducing the intervalley scattering, exchange interactions, or simply a real external magnetic field. In this chapter, we have applied an external magnetic field.

"2+1" Hamiltonian of graphene [64, 62, 63, 89, 29]:

$$-i\hbar v_f \vec{\alpha}\cdot\nabla\Psi = E\Psi, \quad H = v_f \Pi_z \otimes \sigma \cdot \mathbf{p}. \tag{5.11}$$

In the presence of the external magnetic field and stress, the Dirac Hamiltonian 5.11 has the form:

$$\hat{H} = v_f \begin{pmatrix} 0 & \hat{p}_x - i\hat{p}_y - \frac{e(A+A')}{c} & & \\ \hat{p}_x + i\hat{p}_y - \frac{e(A+A')}{c} & 0 & & \\ & & 0 & -\hat{p}_x + i\hat{p}_y + \frac{e(A-A')}{c} \\ & & -\hat{p}_x - i\hat{p}_y + \frac{e(A-A')}{c} & 0 \end{pmatrix}, \tag{5.12}$$

where A is the potential vector of the real external magnetic field, A' is the potential vector of the stress induced pseudo magnetic field.

The top left 2×2 block in the Hamiltonian above is related to the K valley in graphene, the bottom right 2×2 block is related to the K' valley. In the absence of the intervalley interaction, the two valleys are decoupled. The energy eigenvalues of either valley is similar to Eq. 4.5 [15], they are:

$$K: E_n^K = \pm v_f \sqrt{2n\frac{e\hbar(H_0 + H')}{c}}, \tag{5.13a}$$

$$K': E_n^{K'} = \pm v_f \sqrt{2n\frac{e\hbar(H_0 - H')}{c}}. \tag{5.13b}$$

Note: $H' = \nabla \times A'$. Though different form of A' gauge may arise to give the same pseudomagnetic field H', there is no difference among those A's. This is because in the case of static field (see Maxwell equations), by the virtue of the invariance through a gauge transformation, they are equivalent to each other once they are referring to the same pseudomagnetic field.

The schematic representation of the incommensurate LLs constructed in either valleys are shown in Fig. 5.2.

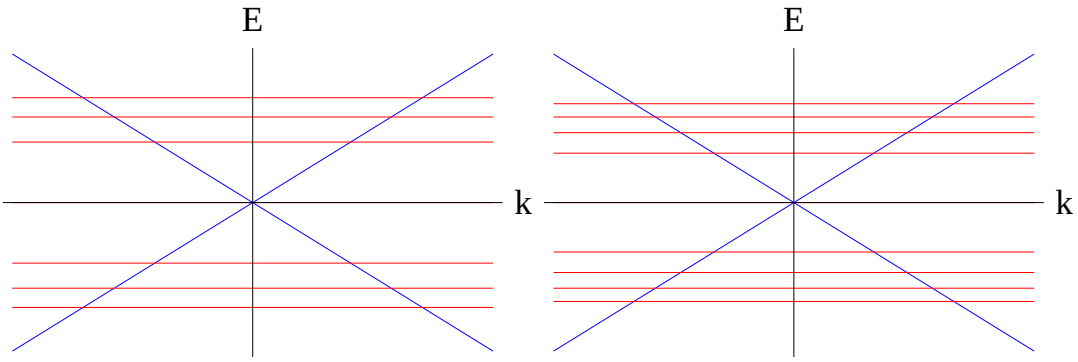

(a) K point (b) K' point

Figure 5.2: The schematic figure shows incommensurate quantized states due to the pseudomagnetic field H'.

5.5 Magnetization

We will focus on the diamagnetism of graphene in this section.

5.5.1 Basic equations

Grand canonical potential:

$$\Omega = -T\sum_{k} \ln\left(1+e^{(\mu-\varepsilon_k)/T}\right) \tag{5.14a}$$

$$= -T\int_{-\infty}^{\infty} g(\varepsilon)\ln\left[1+e^{\frac{\mu-\varepsilon}{T}}\right]d\varepsilon. \tag{5.14b}$$

Magnetization:

$$M = -\left(\frac{\partial\Omega}{\partial H}\right)_{\mu,T}. \tag{5.15}$$

Magnetic susceptibility:

$$\chi = \left(\frac{\partial M}{\partial H}\right)_{\mu,T}. \tag{5.16}$$

5.5.2 Non interaction case

To valid the conditions as in the title of this section, we have the following assumptions:

$$k_BT < k_B\Gamma \ll v_f\sqrt{2\hbar eH}, \quad \Delta\epsilon \ll v_f\sqrt{2\hbar eH}, \quad \langle\mu_{z,z}\rangle < v_f\sqrt{2\hbar eH}. \tag{5.17}$$

The ingrediants of the thermodynamic potential is written in the sum of the two segments:

$$\Omega = \Omega_{vac}|^0_{\varepsilon=-\infty} + \Omega_\mu|^\mu_{\varepsilon=0}, \tag{5.18}$$

where $\Omega_\mu|^\mu_{\varepsilon=0}$ has non-oscillating (Ω_c [90, See eq.2.10]) and oscillating parts ($\tilde{\Omega}$ [90, See eq.2.12]):

$$\Omega_c = -\frac{1}{2\pi^2}\frac{1}{d}\frac{1}{\hbar^2}\int_0^\mu S(\varepsilon)d\varepsilon + \mathcal{O}(T), \tag{5.19a}$$

$$\tilde{\Omega} = \frac{m^*}{2\pi\hbar^2}\frac{\hbar^2\omega_c^2}{\pi^2}\frac{1}{2}\sum_{l=1,\sigma=\pm1}^{\infty}\frac{\psi(\lambda l)}{l^2}\Phi'_{l\sigma}\ \mu, H. \tag{5.19b}$$

The Grand canonical potential at zero chemical potential (μ is at the charge neutral point (CNP)): [91]

$$\Omega_{vac} = g_s g_v\sqrt{\alpha}|H|^{3/2}C\left(\frac{\zeta(3/2)}{4\pi} - 0.1654a\sqrt{|H|C}\right). \tag{5.20}$$

The magnetization at $T \sim 0K$ is the combination of eqns. (5.13, 5.18, 5.19, 5.20).

$$M = M_{vac} + M_c + \tilde{M}. \tag{5.21}$$

The oscillation part of the magnetization $\tilde{M}$ is plot in the Fig. 5.3.

5.6 Broadening of Landau levels

The stress induced effective magnetic field is normally not a constant field but with fluctuations, see Fig. 5.1 for an instant. The fluctuations result in LLs broadening.

We consider our system having the conditions: cyclotron radius $l_B\sqrt{N} \ll$ the sample length scale L. And the fluctuations of the field strength lead to $\rightarrow$ fluctuations of the local density of states ($LDOS(r) \sim B(r)N/\Phi_0$). $\rightarrow$ Energy level broadening ($\varepsilon_N \rightarrow \varepsilon_N + \delta\varepsilon_N$).

Following the Ref. [92], the density distribution is [92, eqn. 28]

$$P(n) = \int_{r<L}\sum_{\pm}\delta(n - BN'/\Phi_0 \pm B'(r)N'/\Phi_0)d^2r/2L^2. \tag{5.22}$$

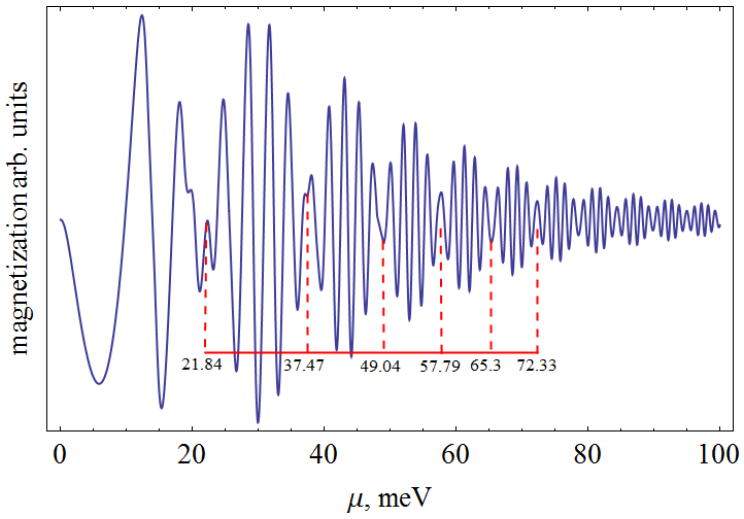

Figure 5.3: The oscillation of magnetization ($\tilde{M}$) with stress in an external magnet field at $H = 20T$ as the function of chemical potential μ. The stress induced pseudo-field is $H' = 2T$.The Dingle temperature $\Gamma = 10K$. The modulated oscillation shows clear bits behavior whose period satisfy the principle $\mu_{n+1}^2 - \mu_n^2 = v_f^2 \frac{H^2 - H'^2}{H'c}$.

The variance of this distribution function is [92, eqn. 29]

$$\langle \delta n^2 \rangle = \frac{N'^2}{4\pi^2 L^4} \langle [\oint A(u)du]^2 \rangle. \tag{5.23}$$

The coherence correspondence (the interactive of the gauge field is not practically coupled between the terms separated far from each other)

$$\langle A_i(r) A_j(r) \rangle \sim Exp[-(r - r')^2 / l_0^2], \tag{5.24}$$

where l_0 is the coherence length, the distance a wave vector reserves its phase.

Broadening of the energy spectrum:

$$\varepsilon_N = v_F \sqrt{2e\hbar} \sqrt{(B + B')N'}, \tag{5.25a}$$

$$\langle \delta \varepsilon_N^2 \rangle \approx [\varepsilon'_N(\bar{n})]^2 \langle \delta n^2 \rangle. \tag{5.25b}$$

This broadening term Eq. 5.25 bring into a correction to the self energy in LK equation. The spectral Green function [90] becomes the form after the correction:

$$g(\varepsilon) = -\frac{1}{\pi} Sgn(\varepsilon - \mu) \mathrm{Im} \sum_{n,k_z} \frac{1}{\varepsilon - \varepsilon_N(k_z) + i\Gamma Sgn(\varepsilon - \mu)}, \tag{5.26}$$

where a correction in the scattering term Γ is replaced by adding a broadening component:

$$\Gamma \to \Gamma + \Gamma_\varepsilon(\varepsilon_n). \tag{5.27}$$

5.7 Conclusion and discussion

In this chapter, we have investigated the electric and magnetic effect induced by the lattice distortions and the possible ways to observe them. We suggested that the oscillations of magnetization described in the last chapter, Chap. 4 also may exist in strain distorted graphene flakes. Here we proposed two ways to search for these oscillations. Routinely, one can measure the magnetization against the stress applied to the flakes. This can be done, for example, by bending copper foils on which the aligned single crystalline graphene flakes have been grown[45]. These graphene flakes formed on the copper substrate randomly will experience the inhomogeneous stress as discussed above. Then on such arrays consisting of thousands or millions of very similar small graphene flakes the magnetization will depend on the angle of the bending and the predicted effects may be observed. An alternative way is to change the charge carrier density in graphene, which can be done by an application of a gate voltage to the manufactured stretched flakes, this latter way may be easier to realize. Thus, the predicted oscillations of magnetization appearing due to applying stress to the graphene flakes may be observed in several ways. In the essence, the magneto-elastic effect is similar to the dHvA oscillations described in the last chapter.

Chapter 6

Snake states and their symmetries in graphene[1]

6.1 Abstract

Snake states are open trajectories for charged particles propagating in two dimension under the influence of a spatially varying perpendicular magnetic field. We examine the correspondence of snake trajectories in single layer graphene for the cases of: (a) uniform doped carrier density in an antisymmetric field profile and (b) antisymmetric carrier distribution in a uniform field. We conclude that these two problems are gauge equivalent and their correspondence is naturally represented in a Nambu-doubled formulation of the two limiting problems. Using gauge transformations in particle hole space to connect these situations, we map the protected interfacial modes to the Bogoliubov quasiparticles of a one dimensional p-wave paired state.

6.2 Introduction

A charged particle moving in two dimensions under the influence of a spatially varying perpendicular magnetic field can exhibit snake state trajectories. These are open two dimensional orbits perpendicular to the the direction of the magnetic field gradient. Snake trajectories occur in both the classical and quantum limits of this problem and are of funda-

[1]In the research of this chapter, I did the numerical work in the sections 6.3, 6.4 and 6.5. The idea of the gauge equavilant is come up by Prof Mele, Sec. 6.4 6.5. The semi-classical interpretation is proposed by Prof Kusmartsev, Sec. 6.6. I also had a lot of cooperate work with the others, names are listed in the Chapter of the publications.

mental interest with potential applications for electron transport in multidomain ferromagnets, two dimensional electron gases and in nanomaterials. In the quantum limit the snake states can be interpreted as the protected modes that occur at domain walls that separate topologically distinct gapped ground states. This picture suggests that snake trajectories can arise even in a *uniform* magnetic field if the particle density is suitably modulated laterally, e.g. by electrostatic gating patterned to form interfaces between distinct quantum Hall ground states.

Indeed exactly this possibility has been explored theoretically and examined experimentally for graphene in a uniform perpendicular magnetic field via measurements of the Hall conductance and of Fabry-Perot like oscillations in the inter-edge conductance across graphene p-n junctions. Graphene is an excellent candidate for this application because it can be electrostatically switched from n to p carrier types and studied in the ballistic transport regime. The converse problem of snake trajectories for a uniform carrier density in a spatially varying magnetic field is even more technically challenging and it has not been examined experimentally. However, a variant of this latter problem *is* routinely encountered in present day experimental environments. In single layer graphene subject to elastic lattice strains, the low energy electronic structure is described by a Dirac Hamiltonian containing a strain-induced gauge field that mimics the effects of a perpendicular (albeit valley asymmetric) magnetic field. For generic smoothly varying strain fields the presence of nodal lines that separate regions of "positive" and "negative" pseudomagnetic field in a single valley is a nearly unavoidable consequence of the symmetry of this strain coupling.

The edge states of the problems with modulated doping and modulated fields are the same, and it is of interest to understand precisely how these two problems are related in the bulk. In this paper we observe that these two situations are actually gauge equivalent representations of the same problem. This equivalence is demonstrated most clearly in a Nambu-doubled formulation of each of these problems, from which it is clear that they are interconverted by local gauge transformations using the particle and hole degrees of freedom in the Nambu basis. Among the insights provided by this approach, we observe that the interfacial degrees of freedom (the snake states) are mapped to a model for the Bogoliubov quasiparticles in a one dimensional superconductor along the tangent line gapped by a "p-wave" pair field.

6.3 Spectra of the folded graphene and pn junction in magnetic field

We consider snake state solutions in two limits of a tight binding theory for electrons on a honeycomb lattice. The Hamiltonian is

$$\mathcal{H} = \sum_i (V_i - \mu)\left(c_i^\dagger c_i - 1/2\right) + \sum_{\langle i,j\rangle} t e^{i\varphi_{ij}} c_i^\dagger c_j + \text{h.c.} \tag{6.1}$$

where $\varphi_{i,j} = (e/\hbar)\int_i^j \vec{A}\cdot d\vec{\ell}$ is the Peierls phase accumulated in a (possibly nonconstant) perpendicular magnetic field B_i. We adopt a coordinate system where the scalar potential V_i and the vector potential $\vec{A}_i$ are spatially varying in the x direction and constant along y. The chemical potential μ is set so that the left and right sectors are simultaneously gapped. The calculations are carried out for "zigzag" interfaces, where a domain wall at $x = 0$ is tangent to a primitive translation vector along y. We examine two limiting domain wall geometries. In the first we assume that the system is uniformly doped, say p type on both sides of an interface where $B(x)$ changes sign. In the second we consider the complementary case where the B field is uniform (or at least a symmetric function of x with no sign changes), and instead the external scalar potential $V(x)$ with zero mean changes its sign on an interface defining a pn junction. We show that the edge-state solutions for these two limits are the same despite the different microscopic dynamics. This manifests a topological equivalence of their bulk ground states. Indeed we find that these can be mapped into each other by gauge transformations that mix the particle and hole degrees of freedom when the problem is rewritten in a Nambu particle-hole basis. This leads to the possibility of inventing architectures that simulate phenomena unusual ballistic transport effects like Andreev reflection even in the absence of a physical superconducting condensate. In the following, we will first discuss the two limits separately and then present their gauge equivalence.

6.3.1 Antisymmetric B, Symmetric V

We assume that the system is uniformly slightly doped p-type and has an antisymmetric magnetic field profile $B(x) = B_o \tanh(x/\ell)$. The spectrum for this problem is displayed in Fig. 6.1. The vertical red lines denote the projections of the bulk K and K' Dirac points, i.e. in the absence of a field these are the interface-projected locations of the bulk gap closures.

For an antisymmetric $B(x)$ the vector potential in Landau gauge is an even function with $A_y(-x) = A_y(x)$. Consequently the system supports normalizable (near) zero energy

states that are "one-sided" in momentum space as shown in Fig. 6.1. There are two types of momentum space anisotropy evident in these spectra: (a) The B-induced zero modes occur only for $q = k_y - K(K') < 0$ in both valleys (b) The $q < 0$ spectrum near K' supports an additional pair of zero modes due to the undercoordinated atoms at the zigzag edges (the total orbital degeneracy of the $q < 0$ spectrum is actually four in this region). The additional low energy modes bridge the K' and K points where they smoothly evolve into the field induced zero modes in the opposite valley. In either case the transition from $q < 0$ to $q > 0$ marks a critical point where the zero energy degrees of freedom hybridize to produce a pair of particle-hole symmetric propagating modes that are confined confined to the domain wall. For p type doping (as illustrated) this pair of interfacial modes copropagate along $-\hat{y}$. Physically the pair of domain wall modes combine cyclotron orbital states of opposite helicity to confine their motion near the interface.

The dispersion of the outer-edge modes near the right-hand K' valley is particularly instructive. Note that this band is nearly flat for small $q < 0$ but it becomes strongly dispersive with positive group velocity for sufficiently large negative q. This occurs via hybridization of the sublattice-polarized edge degree of freedom with the Landau zero mode *on the opposite sublattice* when their guiding centers are forced to the outer edges of the ribbon. Note that the antisymmetry of $B(x)$ requires that the guiding centers are forced to opposite outer edges at the same value of the crystal momentum k_y. These dispersive outer edge modes constitute a return path for the topological current induced in the domain wall. These features can be identified in the spatial distribution of the charge densities plotted in panel (b), see the Figures 6.2, 6.3 6.5, 6.6

To summarize, for constant V and antisymmetric B we observe (a) Four interface/edge modes at the Fermi energy. (b) A pair of co-propagating modes at the domain wall which combine cyclotron motions of opposite helicity. (c)Outer edge modes that hybridize the zeroth Landau level with the zigzag surface state. (d) Valley asymmetry: domain wall modes occur in both valleys but there is support for the outer edge modes only in a single valley. Reversal of the direction of B everywhere will select the other valley.

6.3.2 Symmetric B, Antisymmetric V

We now consider the opposite limit that occurs with uniform magnetic field and an antisymmetric bias $V(x) = V_o \tanh(x/\ell)$. This creates a graphene pn junction in a uniform field which is the situation studied in two recent experiments [93, 94].

The spectrum calculated for this configuration is displayed in Fig. 6.4 where we plot $E - \mu$ as a function of k_y. Here the system is n-doped for $x < 0$ and p-doped for $x > 0$. Again one finds four dispersing modes at the Fermi energy: two with negative velocity at the domain

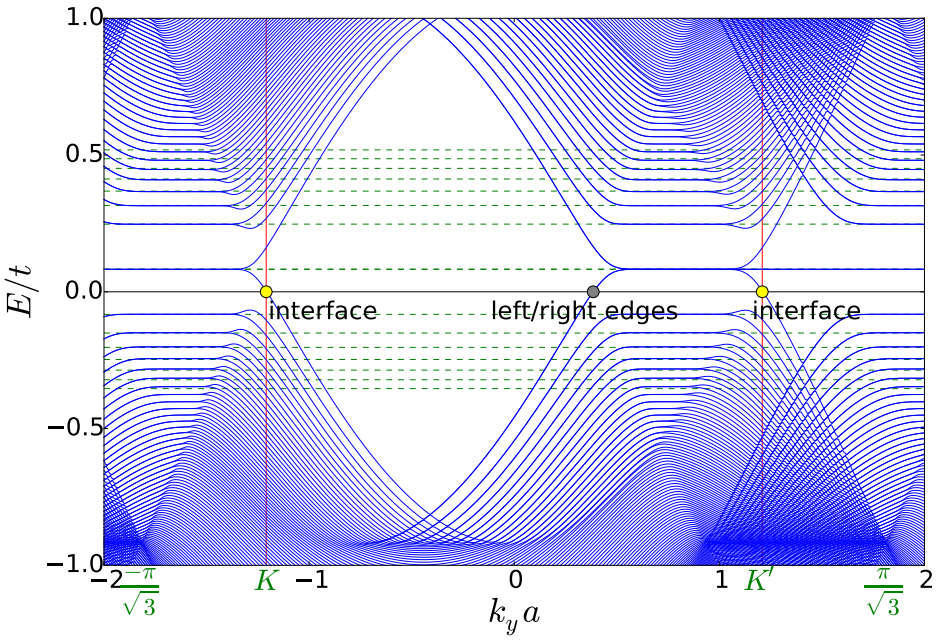

Figure 6.1: Numerically calculated spectrum for graphene with uniform doping in an antisymmetric magnetic field profile. The spectrum plots $E - \mu$ for p-type doping (i.e. $\mu = 0$ and a uniform scalar potential V shifts the system away from neutrality. The spectrum shows four dispersing features at the Fermi energy: two with "positive" velocity on the outer edges, and a pair of modes with "negative" velocity in the domain wall. The flat band that extends from the K to K' points is the surface state for a zigzag edge.

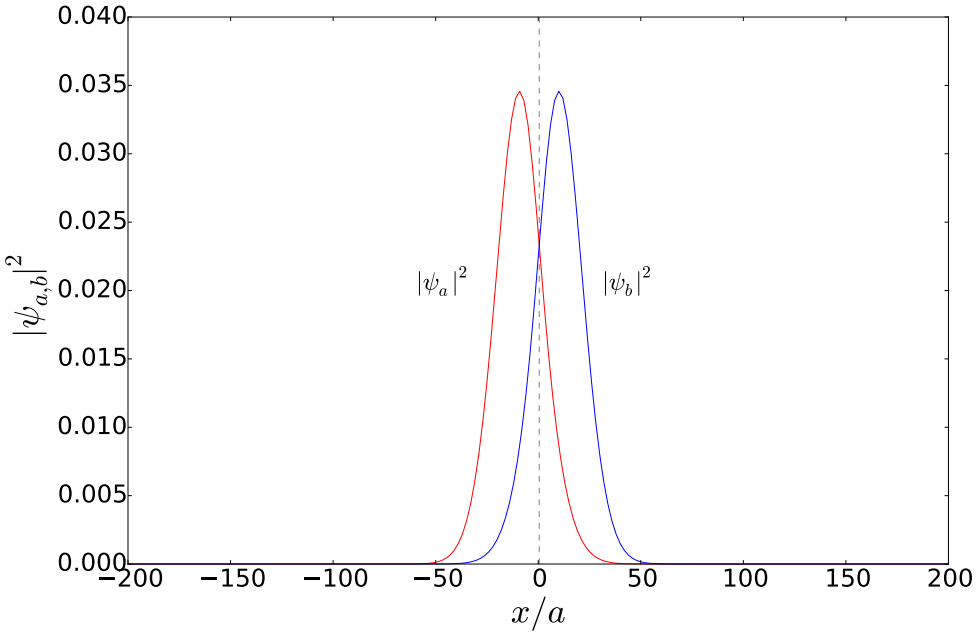

Figure 6.2: Numerically calculated local density of states (LDOS) for the interface zero energy mode associated with one valley K for graphene with uniform doping in an antisymmetric magnetic field profile. The LDOS shows the distribution of the charge density for one of the pair of modes in the domain wall. For the other valley, K' the density of the a and b components of the wave function are interchanged.

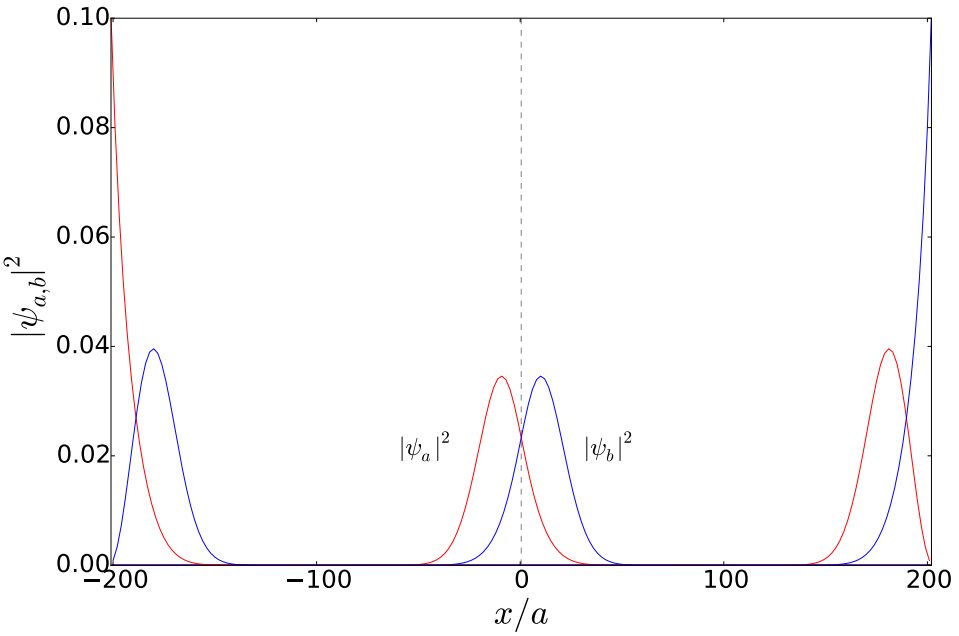

Figure 6.3: Numerically calculated local charge density for all four zero energy modes for graphene with uniform doping in an antisymmetric magnetic field profile.

wall, and two with positive velocity confined on the outer edges. Despite this similarity, the mechanism producing the edge state structure is quite different. We note that the $\sqrt{n}$ signature of Landau quantization of the Dirac spectrum is observed for $q = k_y - K > 0$ in the K valley but for $q' = k_y - K' < 0$ in the K' valley, i.e. the Landau quantized spectra are both one-sided in momentum space, but in opposite senses in the two valleys. In the forbidden regions $q < 0$ and $q' > 0$ the spectrum collapses to a pair of nearly degenerate orbital doublets that connect the two valleys. This degeneracy is exact at $k_y = \pi/a$: the energy jump that is produced by the transition $q > 0$ to $q < 0$ (and vice versa for q') is the quantized energy spacing between the zeroth and first Landau levels, so all the levels for $k = \pm\pi$ are twofold degenerate.

Here the dispersion of the confined interfacial modes can be understood as a response to the lateral electric field produced in the *pn* junction. As x crosses zero the scalar potential $V(x)$ switches its sign and the internal electric field $E = -\partial_x V$ is nonzero. Thus a state with drift velocity $\vec{E} \times \vec{B}/B^2$ sees no deflection and can propagate freely. This can be contrasted with the guiding-center mechanism that liberates these modes in the former antisymmetric-B problem where $E = 0$ and one requires the compensation of helicities of the orbits in reversed B fieldsto produce freely propagating interfacial snake states.

Interestingly, the appearance of dispersive edge modes on the *outer* boundaries follows exactly the same recipe as for the antisymmetric B problem. The quiding center of the Landau zero mode which is sublattice polarized, is forced to the outer edge of the ribbon where it hybridizes with the zigzag surface state on a complementary sublattice to form the one-way dispersive excitation. However, because the B field is constant in this problem, the guiding centers are forced to the outer edges of the ribbon at opposite momenta $\pm k_y$. The entire spectrum of Fig. 6.4 is then invariant under the combined transformation $E - \mu \to -(E - \mu)$ and $k_y \to -k_y$.

To summarize the main results from this model for the graphene *pn* junction in a uniform B: (a) Four interface/edge modes at the Fermi energy. (b) Co-propagating modes in the domain wall determined by their drift velocity specified by B and the potential gradient in the wall. (c) Conventional outer edge modes that hybridize a Landau zero mode with the surface state.

6.4 Gauge equivalence of the two problems in Nambu basis

It is striking that despite the different microscopic origins of the domain wall solutions and the different structure of the full spectra displayed in Figs. 6.1 and 6.4, the basic pattern of

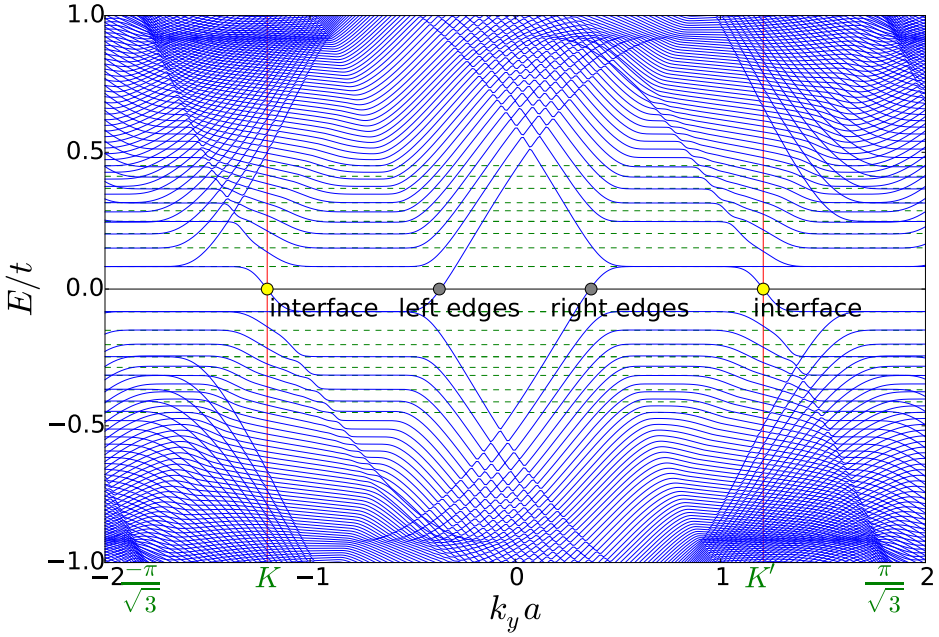

Figure 6.4: Spectra for the *pn* junction in a uniform field. The plot gives $E-\mu$ as a function of k_y for a geometry where B is constant but $V(x) = V_o \tanh(x/\ell)$. The system supports four edge and interface modes: two positive velocity modes on the outer edges and two negative velocity modes at the domain wall. The flat feature is a zigzag edge state that morphs into the zeroth Landau level. The spectra are one sided, and show graphene character near a shifted neutrality point of one sign of $q = k - K$ in one valley and the opposite sign in the other. At $k = \pi$ the spectra are twofold degenerate.

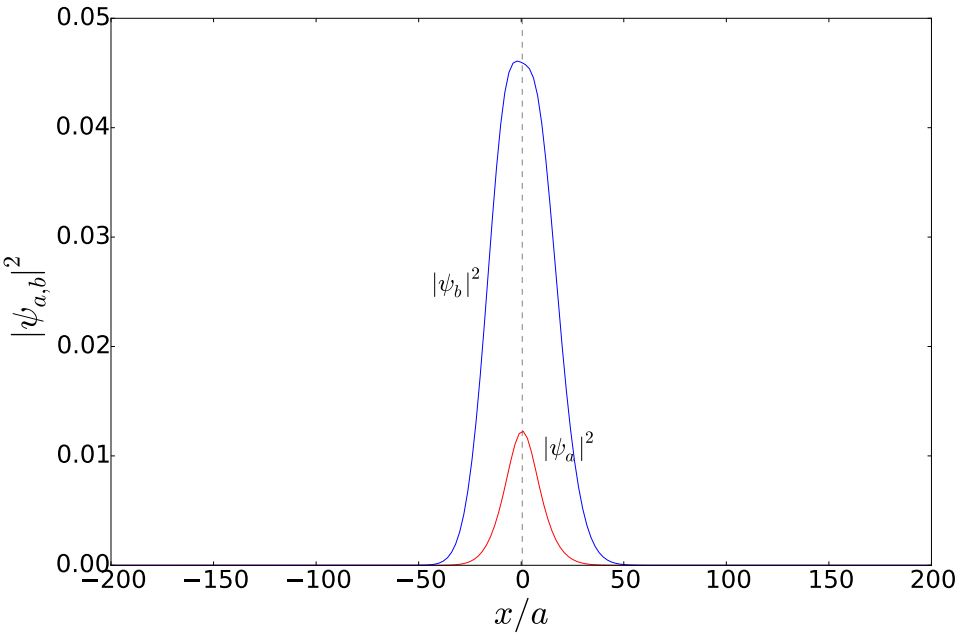

Figure 6.5: Numerically calculated local density of states (LDOS) for the interface zero energy mode associated with one valley K for graphene pn junction with the potential profile $V(x) = V_o \tanh(x/\ell)$ in homogeneous transverse magnetic field. The LDOS shows the distribution of the charge density for one of the pair of modes in the domain wall. For the other valley, K' the density of the a and b components of the wave function are interchanged.

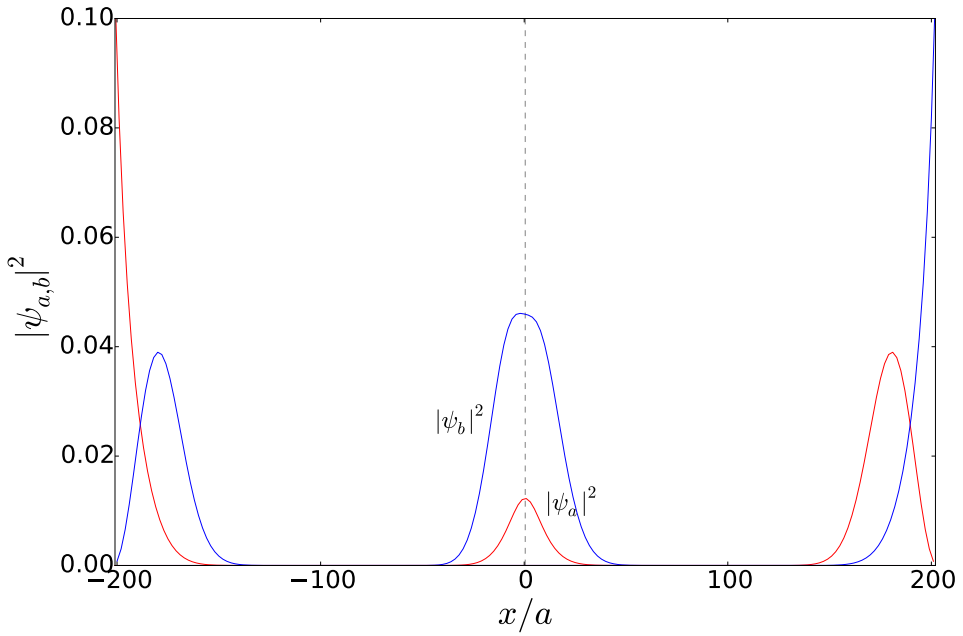

Figure 6.6: Numerically calculated local charge density for all four zero energy modes for graphene pn junction with the potential profile $V(x) = V_o \tanh(x/\ell)$ in homogeneous transverse magnetic field.

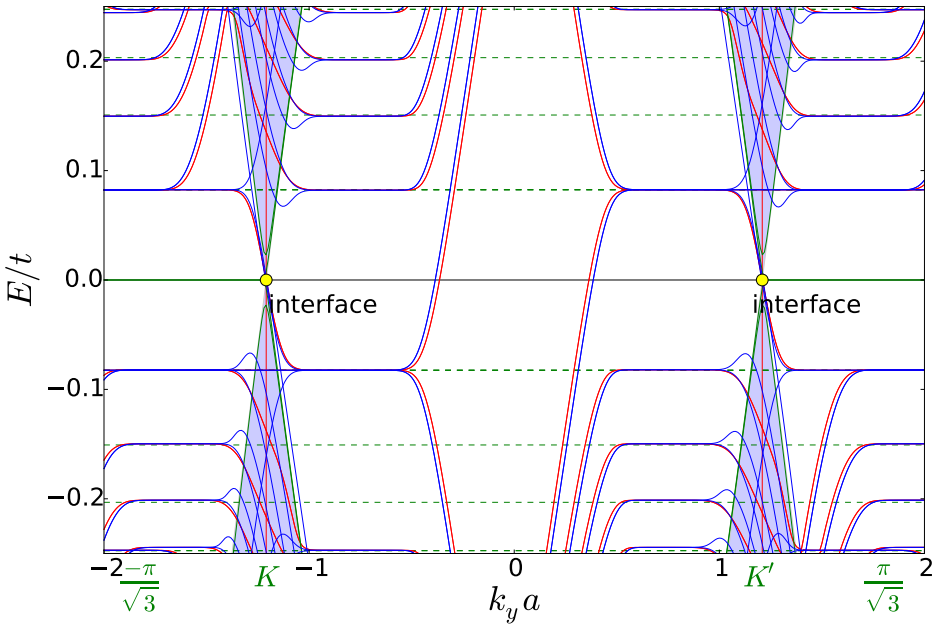

Figure 6.7: Bogoliubov spectrum for the topological domain wall in graphene. The spectrum is the particle-hole doubled version of the antisymmetric B spectrum, plotted only in the particle channel in Fig. 6.1.

the edge state currents is the same. This is evidence of the topological character of these modes. By negating either B or V at the interface we reverse the sign of the Chern number in the first fundamental gap between Landau levels and therefore we require the same pattern of boundary currents. This suggests that the ground states of these two systems can be adiabatically mapped into each other. Yet this conclusion is surprising since the momentum space structures of their spectra examined in the previous section are evidently controlled by the underlying dynamics which are quite different and in fact incompatible for the two states. In this section we show that these ground states can nonetheless be mapped into each other using a particle-hole extension of the original formulations of both problems. The required mapping is a rotation in the particle and hole degrees of freedom expressed in a Nambu basis. Local gauge transformations in this basis interconvert the two problems at the expense of introducing a fictitious pairing field within the domain wall. In this section we develop a family of such mappings and then return to the consequences of the induced pseudo-pairing field in Section xx.

The problems of Section I.A and I.B are distinguished by the coupling of external potentials to bilinears in the fermion operators c and $c^\dagger$. For example, the Peierls phase in Eqn. 1 is coupled to nearest neighbor bilinears in the form

$$te^{i\varphi_{i,j}}c_i^\dagger c_j, \tag{6.2}$$

while the scalar potential that defines the local doping is coupled through the site density operator

$$V_i\left(c_i^\dagger c_i - 1/2\right). \tag{6.3}$$

Sign reversal of the magnetic field direction negates the exponentiated phase in Eqn. 2 while a reversal of the scalar potential flips the sign of the coupling to the net charge operator Eqn. 3. Ignoring the physical spin of the electrons, these reversals are affected by the particle hole transformations

$$\begin{aligned}\bar{c} &= c^\dagger,\\ \bar{c}^\dagger &= c,\end{aligned} \tag{6.4}$$

whereby

$$\begin{aligned}te^{i\varphi_{i,j}}c_i^\dagger c_j \mapsto -te^{i\varphi_{i,j}}\bar{c}_j^\dagger\bar{c}_i = -te^{-i\varphi_{j,i}}\bar{c}_j^\dagger\bar{c}_i,\\ V_i\left(c_i^\dagger c_i - 1/2\right) \mapsto -V_i\left(\bar{c}_i^\dagger\bar{c}_i - 1/2\right).\end{aligned} \tag{6.5}$$

For our application it is useful to collect these operators in two-spinors that resolve the two degrees of freedom at each Bloch wavevector k

$$\psi_k = (a_k, b_k), \tag{6.6}$$

and write the original problem in a doubled Nambu four-component basis

$$\mathcal{H}_N(k) = \begin{pmatrix} \psi_k^\dagger & \psi_{-k} \end{pmatrix} \begin{pmatrix} \mathcal{H}_k & 0 \\ 0 & -\mathcal{H}_{-k}^* \end{pmatrix} \begin{pmatrix} \psi_k \\ \psi_{-k}^\dagger \end{pmatrix}. \tag{6.7}$$

When summed over k this theory gives a doubled "redundant" description of the original problem.

Using Eqns. 5 a global rotation in particle-hole space can globally "choose" the signs of B and V. For example, consider a Hamiltonian $\mathcal{H}[V(x), B(x)]$ parameterized by the fields $V(x)$ and $B(x)$. Then define 2×2 Pauli matrices σ_μ acting on the two sublattice degrees of freedom and Σ_μ acting on the particle and hole degrees of freedom in the Nambu representation. A global operator of the form

$$\mathcal{S}(\theta) = \cos\theta\, \mathcal{S}_1 + \sin\theta\, \mathcal{S}_2\,, \tag{6.8}$$

where $\mathcal{S}_1 = \sigma_3 \otimes \Sigma_1$ and $\mathcal{S}_2 = \sigma_3 \otimes \Sigma_2$, has the property of formally flipping the signs of V and B everywhere in the manner

$$\mathcal{S}(\theta)^\dagger \mathcal{H}[V(x), B(x)] \mathcal{S}(\theta) = \mathcal{H}[-V(x), -B(x)]\,. \tag{6.9}$$

We will discuss the behavior of $\mathcal{S}(\theta = 0) = \mathcal{S}_1$ first and then return to the interpretation of the remaining phase degree of freedom θ.

In an analogous manner, if we promote $\mathcal{S}$ to a local gauge degree of freedom we can introduce a gauge transformation $\mathcal{S}_1(x)$ that *locally* defines the signs of V and B. Specifically, we can use this to interconvert the domain wall configurations of sections I.A and I.B. To keep track of the signs of V and B in the left and right spaces we use a shorthand notation $\mathcal{H}[v_-, v_+; b_-, b_+]$ where $v_\pm$ and $b_\pm$ specify the asymptotic signs of the potential and magnetic field strength. In this notation, $\mathcal{H}[-,+;+,+]$ denotes a situation with $V < 0$ on the left and $V > 0$ on the right, all immersed in a uniform positive field $B > 0$. We now introduce a local gauge transformation

$$\mathcal{S}(x) = \cos\alpha(x)\, \hat{I} + i \sin\alpha(x)\, \mathcal{S}_1\,, \tag{6.10}$$

where $\alpha(-\infty) \to \pi/2$, $\alpha(\infty) \to 0$ and $\alpha(0) = \pi/4$. This has the effect of implementing a one-sided particle-hole transformation, where the local gauge transformation evolves smoothly through the interface. We retain the original problem for $x \gg 0$ but swap particle and hole amplitudes for $x \ll 0$ to invert the signs of V and B. This transformation is unitary and performs the mapping

$$\mathcal{S}\mathcal{H}[-,+;+,+]\mathcal{S}^\dagger = \mathcal{H}[+,+;-,+]\,, \tag{6.11}$$

thereby swapping the representation of a *pn* junction in a uniform field with a system with uniform doping in an antisymmetric B field. In the doubled space the ground states can be

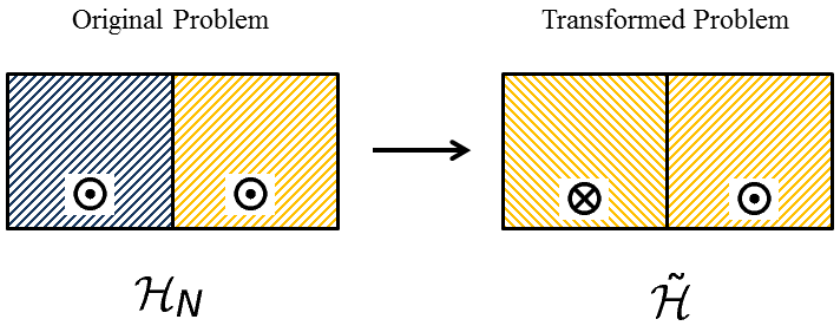

Figure 6.8: (This figure is made by a cooperate PhD student Matej Brada) The left side of the figure describes the original problem, which consists of electrons in the right half and holes in the left half of the sample. The magnetic field is uniform throughout the sample and is pointing out of paper. The right side of the figure describes the transformed problem, where holes in the left half of the sample gets converted to electrons and the field on the left half of the sample reverses its direction.

identified implying that zero-mode structure is unchanged. This In Figure 6.7 we overlay the spectra calculated for the two problems in the Nambu representation, illustrating this correspondence.

6.5 Topological classification

The eigenvalues of the squares of the time-reversal Θ, the particle hole Ξ, and the chiral symmetry Π operators decide the topological class to which a given Hamiltonian belongs to [95, 96, 97, 98]. Our problem does not have time reversal or chiral symmetry (eigenvalues of Θ^2 and Π^2 are zero), but does have the particle-hole symmetry. The two possible outcomes of $\Xi^2 = \pm 1$ imply two different topological classification for our Nambu Hamiltonian, class D and C respectively. Demanding that Ξ anticommutes with $\tilde{\mathcal{H}}$ and is unitary, we find $\Xi = i\sigma_1\tau_2$, such that $\Xi^2 = -1$. Thus, in the Nambu formulation, the Hamiltonian describing

the bulk regions on either side of the domain wall belongs to the Altland–Zirnbauer symmetry class C, with a 2 $\mathbb{Z}$ topological invariant. We have verified this explicitly, by calculating the Chern numbers in the bulk on the either side of the domain wall [99]. On either side of the domain wall, the Chern numbers for the electrons and the Nambu holes add up resulting in the total Chern number to be 2 $\mathbb{Z}$ (*only even integers*). As an example, consider a situation, where the chemical potential is in between the zeroth and the first Landau level in the original problem (see Fig. 6.8). In this case we find that in the Nambu basis, the left half of the sample has Chern number -2 and the right half has Chern number $+2$. This mismatch of Chern numbers suggests the presence of *four* edge states at the domain wall. However, since we have *artificially* doubled the spectrum by going to the Nambu basis, the *genuine* number of edge states at the domain wall is *two*.

6.6 Duality of electrical and magnetic fields actions

Although the full energy spectrum of the hexagonal graphene lattice can be obtained from a tight binding approximation more light on the considered problem can be shed from the continuum approximation. In this case a Taylor expansion centered at two non-equivalent Dirac point **K** and **K'** can produce the Dirac-like Hamiltonians $H_K = v_f \vec{\sigma} \cdot \hat{p}$ and $H_{K'} = v_f (\sigma_x \hat{p}_x - \sigma_y \hat{p}_y)$ [100]. Together these Hamiltonians can combine to reproduce the 4x4 Hamiltonian from Dirac gamma matrices or inverted band structure heterojunctions [101]. Due to the similarities of the two Hamiltonians, here we will only consider the **K** point. An energy gap can be introduced into this Hamiltonian to change the linear energy spectrum of a Dirac point into a parabolic spectrum. The graphene Hamiltonian at **K** point with an external potential $V(x)$ becomes [102, 103, 104]:

$$\hat{H} = v_F(\boldsymbol{\sigma} \cdot \hat{p}) + IV(x) \,. \tag{6.12}$$

Where v_F is the Fermi velocity, σ is the Pauli matrices, $\hat{p}$ is the momentum operator: $\hat{p} = (\hat{p}_x, \hat{p}_x)$, I is the identity matrix and $V(x)$ is an external or bias potential associated with applied perpendicular electric field. Below we consider two cases of asymmetrical electric and symmetric magnetic fields and vice versa considered above.

Let us consider the first case of homogeneous magnetic field applied to the graphene p-n junction. In this case the biased $V(x)$ is asymmetric, i.e. $V(x) = -V(-x)$ and the vector potential, chosen in Landau gauge has the form $A_y = -Bx$, where B is transverse magnetic field applied perpendicular to the graphene plane. Then the Dirac Hamiltonian for electrons normalised for v_F and associated with K valley has the form:

$$H = \begin{pmatrix} V(x) & i(\partial_x - i\partial_y - A_y) \\ i(\partial_x + i\partial_y + A_y) & V(x) \end{pmatrix}. \tag{6.13}$$

Because of the asymmetric potential $V(x)$ the solution for the Dirac equation $H\Psi = \epsilon\Psi$ may have the following form:

$$\Psi = e^{ik_y y} \begin{bmatrix} a(x) \\ b(x) \end{bmatrix}. \tag{6.14}$$

Where the values k_y are associated with the wave vector along y direction where the translation invariance is still not broken. After this substitution the Dirac equation is split into a pair of couple differential equations:

$$i\partial_x b - i(k_y + A_y)b = (\epsilon + V)a\,, \tag{6.15}$$

$$i\partial_x a + i(k_y + A_y)a = (\epsilon + V)b\,. \tag{6.16}$$

After expressing $b(x)$ from the second equation and with the next substitution $b(x)$ into the first equation after simplification we obtain that

$$-\partial_x^2 a + U_-(x)a - ib\partial_x V = (\epsilon + V)^2 a\,, \tag{6.17}$$

where $U_\pm(x) = (k_y + A_y)^2 \pm \partial_x A_y$ For $b(x)$ we obtain an analogous equation:

$$-\partial_x^2 b + U_+(x)b - ia\partial_x V = (\epsilon + V)^2 b\,. \tag{6.18}$$

In the case of asymmetric magnetic field and homogeneous doping, when $V(x) = const$ and $\partial_x V = 0$, these equations are decoupled and may be solved separately. In both cases we have a particle described by Shrödinger-like equation in a complex parabolic like potential. In the case when $B(x) = Bsign(x)$ the potential for the $a(x)$ function, $U_a(x)$ consists of two parabolas, shifted by each other by $2B$, see, Fig.6.9. The minima of this potential corresponds to the value $x = \pm k_y/B$. The potential in the equation for $b(x)$ is obtained by symmetrical reflection from the potential for $a(x)$: $U_b(x) = U_a(-x)$. The wave functions for other valley, at the K' point of BZ, is obtained from these equations, where $a'(x) = b(x)$ and $b'(x) = -a(x)$. Therefore, the corresponding Landau-like spectra associated with the combined parabolic potential, can be found with the use of some quasi classical approach.

6.7 Discussion and conclusion

Thus we see from the previous section that the lowest energy potential in both cases of asymmetric electrical and magnetic fields have identical form, while when energy rises the

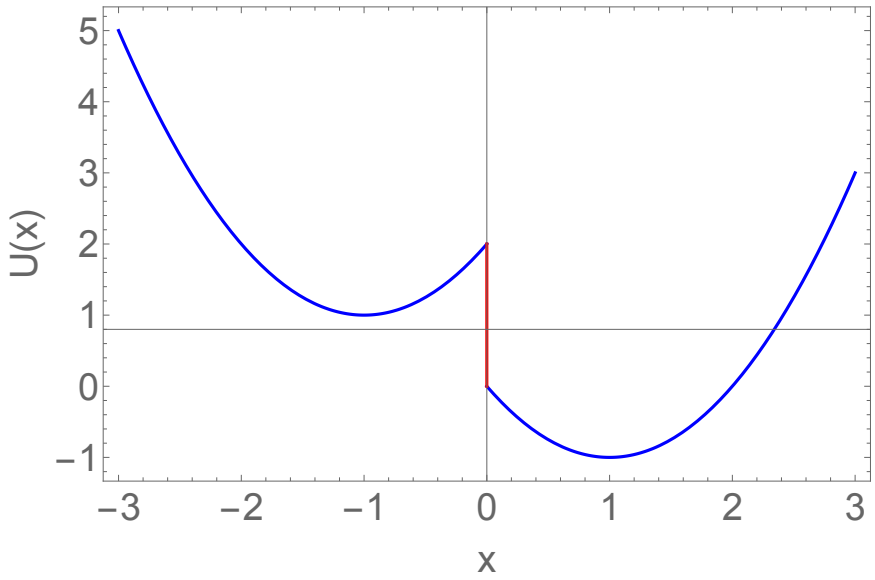

Figure 6.9: The potential of the interface created by asymmetric magnetic field $B(x) = -Bsign(x)$. It consists of two parabolas: $U_+(x) = (Bx - k_y)^2 - B$ when $x > 0$ and $U_-(x) = (Bx + k_y)^2 + B$ when $x < 0$, which are shifted with respect to each other by the amplitude of applied magnetic field, e. g. as $B = \partial_x A_y$.

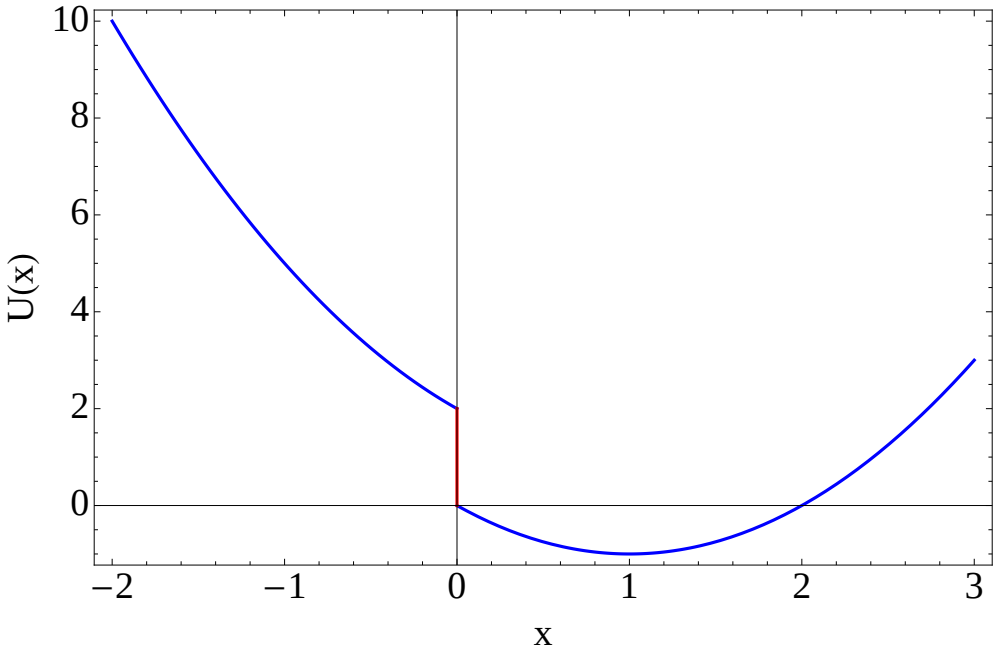

Figure 6.10: The potential of the interface created by asymmetric electric bias field $V(x) = -V sign(x)$. It consists of one parabola, which has a jump at the interface related to value of electric field in the p-n junction, e. g. as $E = \partial_x V(x)$.

difference in their potentials occurs. Therefore, the symmetries that allow this identification are generally broken at higher energy (i.e. for quasiparticle states with $E-\mu \neq 0$).

Time dependent gauge transformation – The presence of the superconducting pairing term in the transformed problem can also be understood by imagining the gauge transformation $\mathcal{S}(x)$ to be time dependent. In the beginning of this gauge transformation, our system is described by the original Hamiltonian ($\mathcal{H}_k$), and at the end by the transformed Hamiltonain ($\tilde{\mathcal{H}}$). We assume this time dependent gauge transformation to be adiabatic, which means that the time it takes to transform the original problem is much longer than any other time scale in our problem. As time evolves the holes in one half of the system are *converted* to electrons, and the magnetic field in that half flips sign, while we retain the original problem in the other half. Converting holes to electrons in that half *requires* an *infinite source* of electron pairs. This source is readily provided by the effective superconducting term at the domain wall. Furthermore, the reversal of the magnetic field in that half implies that the total flux changes as a function of time, which induces an EMF via the Lenz's law, giving rise to currents in the domain wall (the current pattern is such that it opposes the change in flux in that part). These currents are carried by our edge states at the domain wall. At the end of the transformation the total flux vansihes and is no longer time dependent.

Chapter 7

Summary and discussion

7.1 Summary

We started from analyzing the conductivity of graphene related to its edge states/channels and made an explicit understanding of the roles of the edge states/channels in the quantum transport regime. In graphene nanoribbons, the energy spectrums show a set of peaks corresponding to the different values of the Fermi energy. The related density of states implies a nonlinear dependence of the conductivity on the Fermi energy of the nanoribbins. When applying a magnetic field perpendicular to the plane of the nanoribbons, the ordinary Landau levels are formed. These bulk Landau levels with flat spectrum bend up when the states are approaching to the terminated boundaries, resulting in the conventional integer quantum Hall effect. The plot of the local density of states and charge distribution at the Fermi surface confirm an expected polarization of the two sublattices on the edges of the graphene nanoribbons. In nanoribbons, these edge states play the main role in contributing to the conductivity. The analytic calculations and numerical simulations get good agreements while the semi-classical approach renders an intuitive image.

Next, we had a brief look at the Aharonov-Bohm effect in such graphene structures as nano-disks and nano-rings. We found that these graphene systems are likely to demonstrate the conventional Aharonov-Bohm effect. The period of the oscillations of the conductivity as a function of the magnetic flux seems to be the same as in the cases involving either Pauli Hamiltonians or square lattices though there are two sublattices in graphene rather than one. In graphene nano-disk and nano-ring, we also performed a number of numerical simulations to find an influence of the magnetic field and the geometrical confinement on the conductivity characteristics. The results of these simulations show the periodic behaviors of conductivity which indicate clear traces of Aharonov-Bohm effect in these nano-devices.

We described new quantum oscillations in the magnetization of graphene flakes that are induced by magnetic fields which depend on the shape of the flake. At small values of the field they are due to the Aharonov-Bohm effect and with increasing field they are transformed into De Haas-van Alphen oscillations.

The specific form of the De Haas-van Alphen oscillations is analyzed in terms of their energy spectrum, which has a form of Hofstadter's butterfly. Numerical results obtained by using both a lattice tight-binding model and a continuum Dirac equation are presented and compared. We also discussed possible experiments to investigate the quantum oscillations in Moiré and graphene anti-dot superlattices.

The stress/strain caused distortions of graphene lattices can induce a gauge field. The strength of this pseudo-magnetic field is mathematically related to the Gaussian curvature of the surface of the graphene sheet. By carefully stretching of the graphene sheet, we can create a roughly homogeneous pseudo-magnetic field in the sheet. There exists an evident difference between this pseudo magnetic field and a real external field. In the case of the pseudo-magnetid field, the electrons in either of the two valleys in momentum space, which originate from two graphene sublattices, see the fields of equal strength but of opposite directions. However, we show that by application of an external magnetic field the underlying features of this stress induced gauge field can be more easily revealed. We find that both the conductivity and magnetization demonstrate the specific quantum oscillations similar to the familiar De Haas-van Alphen oscillations.

We also looked through topological aspects of graphene-like systems. Here we considered a model of the graphene ribbon with a domain wall in the centre. This domain wall is created through the difference of the chemical potentials and magnetic fields on the opposite sides of the interface. We found that semiclassical trajectories of the electrons in the domain walls have snake like shapes. We analized the snake trajectories in a single layer graphene for two cases: (i) a uniformly doped carrier sample placed in the field with an antisymmetric profile and (ii) antisymmetric carrier distribution in an uniform field. We concluded that these two cases are gauge equivalent and their correspondence is naturally represented in a Nambu-doubled formulation of the two limiting configurations. By using the gauge transformations in the particle hole space to connect these situations, we mapped the protected interfacial modes to the Bogoliubov quasiparticles of a one dimensional p-wave paired state.

With many of its already known outstanding properties, the graphene has found a number of exciting electronic and optoelectronic applications. Some of the examples include the field effect transistors, field emission generators, bio-sensors and the electrode materials. On the other hand, there are still some obstacles in the synthesis of the high quality graphene samples (as far as I recognized, it recently becomes a less difficult problem through introduction of the CVD growth technique), controlling bandgap widths and surface absorptions,

and several other practical problems. Till now, the majority of the practical applications of graphene are based on its extraordinary conductivity.

Potential applications of graphene based on various mesoscopic quantum effects, including those discussed in this thesis, are expected to to be a subject of future investigations.

7.2 Discussion

There remains several unfinished parts of the research investigated in this thesis. In the study of Aharonov-Bohm effect in Chapter 3, I had not obtained an accurate analytic result of the conductivity corresponding to Aharonov-Bohm scattering in the graphene flakes. There, better improved analytical definitions of the boundary conditions are required. In the study of this thesis, we had not considered the effects corresponding to the electron-electron interactions. The Green's function technique is widely used to analyze the many-body problem. In the research in chapter 5, I had tried to investigate this problem but have not finished. The presence of the magnetic field increased the complexity of this problem. The results may be likely to show characteristics similar to the fractional quantum Hall effect. In studying the topological aspects of graphene systems, I had started to investigate the topological aspects of the multilayered graphene superlattices. These research include the topological interpretation and predictions of the physical phenomenon of the multilayered graphene. Further, the modified graphene systems with defects, doping or other treatment remain to be investigated in the future.

Publications

Yang Liu, M. Brada, E. J. Mele, F. V. Kusmartsev, *Magnetisation Oscillations, Boundary conditions and the Hofstadter Butterfly in Graphene Flakes*, Annalen der Physik, **526**, 449 (2014).

Yang Liu, Rakesh Tiwari, Matej Brada, Ch. Bruder, Fedor Kusmartsev and E. J. Mele, *Snake states and their symmetries in graphene, Phys. Rev. B,* **92***, 235438 (2015).*

R. D. Y. Hills, M. Brada, Yang Liu, and F V Kusmartsev, *From graphene and topological insulators to Weyl semimetals*, Chapter in the book 'Symmetry, Spin Dynamics and the Properties of Nanostructures': 277-315. (2015) DOI: 10.1142/9789814740371_0012

Appendix A

Tight-binding Model for graphene

The tight-binding model is usually derived by assuming that electrons have tunneling amplitudes between orbitals on neighboring atom sites. These hopping processes are described by the Hamiltonian:

$$H = \sum_{<i,j>} t_{ij} c_i^\dagger c_j + h.c.\,, \tag{A.1}$$

where the operator $c_i^\dagger$ creates a spinless electron on the site i, while c_j - destroys a spinless electron on the site j. The matrix $||t_{ij}||$ describes the hopping overlapping integrals. With magnetic field, an additional phase is added to each matrix element, t_{ij}, through Peierls substitution,

$$t_{ij} \to t_{ij} e^{\frac{2\pi}{\Phi_0}\int_{r_i}^{r_j} \vec{A}\cdot\vec{dl}},$$

where $\Phi_0 = ch/e$ is an elementary flux quantum. For our numerical simulations described below, the magnetic flux through each hexagon has been taken in the form $\Phi = p/q\Phi_0$, where p/q is a rational number, which might be interpreted as a number of cells per current vortex. For simplicity, we only consider the nearest neighbor sites' hopping integrals.

A.1 Infinite graphene sheet

The graphene lattice is shown in Fig. A.1. We choose Landau gauge $A = (0, Bx, 0)$ for the vector potential associated with the magnetic field $H = H_0\hat{z}$. The Schrödinger equations for sites A and B are derived through the equation A.1 and has the following forms:

$$\varepsilon\psi_m^{B2} = t_{B2,A1}\psi_m^B + t_{B2,A2}\psi_m^B e^{-iky(\sqrt{3}/2)a} + t_{B2,A3}\psi_{m+1}^B e^{iky(\sqrt{3}/2)a}\,, \tag{A.2a}$$

$$\varepsilon\psi_m^{A1} = t_{A1,B1}\psi_m^B e^{-iky(\sqrt{3}/2)a} + t_{A1,B3}\psi_m^B + t_{A1,B2}\psi_{m+1}^B e^{iky(\sqrt{3}/2)a}\,. \tag{A.2b}$$

Here the tight-binding wave function, $\vec{\psi}_m = (\psi_m^A, \psi_m^B)^T$, defines the probability of the electron to occupy the m-th site of A or B sublattices of the graphene and ε is an eigenvalue.

After simplification of the above equations, we obtain the Harper equation in the form:

$$\varepsilon\psi_m^B = \psi_{m-1}^A + a_m\psi_m^A\,, \tag{A.3a}$$

$$\varepsilon\psi_m^A = a_m\psi_m^B + \psi_{m+1}^B\,, \tag{A.3b}$$

where $a_m = 2\cos\left(k_y\frac{\sqrt{3}a}{2} + 2\pi\frac{p}{q}\frac{1}{3a}\frac{x_m^A + x_m^B}{2}\right)$ [60]. Notice the periodicity of these equations, we choose the unit cell in commensurate with the magnetic flux per plaquette. The unit cell has a width of size q and is shown by the shadowed region in Fig. A.1. The magnetic flux in the unit cell is equal to the value of one flux quantum.

Expressing these equations in matrix form, where we display only nonvanishing elements, we obtain:

$$\begin{pmatrix}
0 & a_0 & & & & & & e^{ikdq} \\
a0 & 0 & 1 & & & & & \\
 & 1 & 0 & a_1 & & & & \\
 & & a_1 & 0 & 1 & & & \\
 & & & & \cdots & & & \\
 & & & & a_{q-2} & 0 & 1 & \\
 & & & & & 1 & 0 & a_{q-1} \\
e^{-ikdq} & & & & & & a_{q-1} & 0
\end{pmatrix}
\begin{pmatrix}
\psi_0^B \\ \psi_0^A \\ \psi_1^B \\ \psi_1^A \\ \\ \psi_{q-2}^A \\ \psi_{q-1}^B \\ \psi_{q-1}^A
\end{pmatrix}
= \varepsilon
\begin{pmatrix}
\psi_0^B \\ \psi_0^A \\ \psi_1^B \\ \psi_1^A \\ \\ \psi_{q-2}^A \\ \psi_{q-1}^B \\ \psi_{q-1}^A
\end{pmatrix}. \tag{A.4}$$

A.2 Zigzag graphene nanoribbon

We use Dirichlet boundary conditions as describe by the equation Eq. 2.2 in the chapter 2.

$$\psi_A^{(')}(x=0) = \psi_B^{(')}(x=N) = 0\,, \tag{A.5}$$

where N is the number of sites in width L of the ribbon. The matrix Hamiltonian A.4 becomes

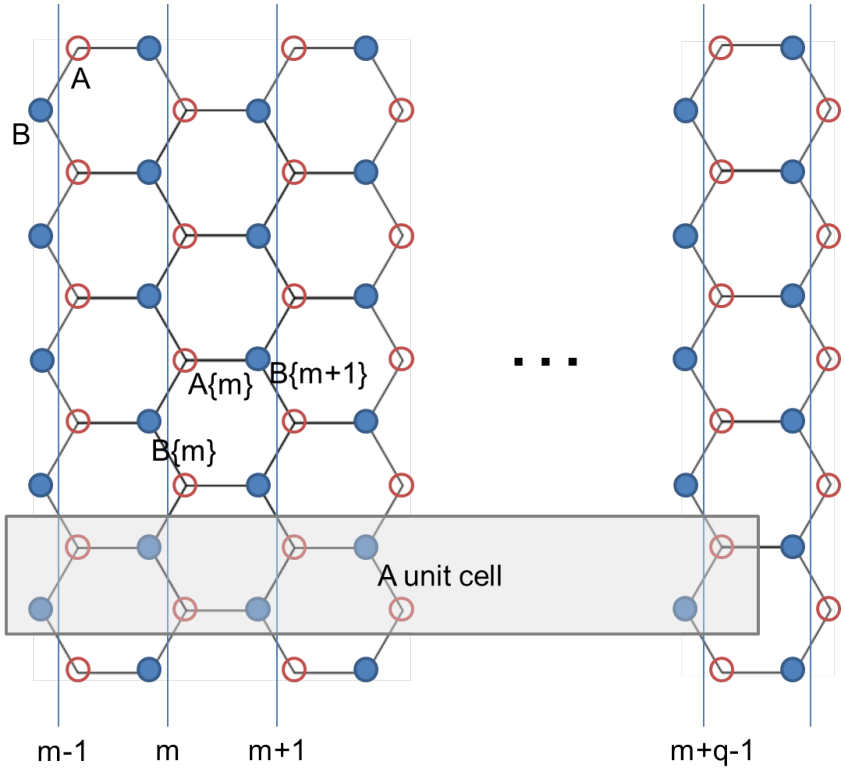

Figure A.1: Schematic graph showing the geometry of the unit cell chosen. The magnetic flux per unit cell is chosen to be equal to some fractional p/q number of the elementary flux quantum. The choice of the gauge is flexible in infinite graphene as long as they represent the correct value of magnetic flux in each cell.

$$\begin{pmatrix} 0 & a_0 & & & & & & \\ a0 & 0 & 1 & & & & & \\ & 1 & 0 & a_1 & & & & \\ & & a_1 & 0 & 1 & & & \\ & & & & \cdots & & & \\ & & & & a_{N-2} & 0 & 1 & \\ & & & & & 1 & 0 & a_{N-1} \\ & & & & & & a_{N-1} & 0 \end{pmatrix} \begin{pmatrix} \psi_0^B \\ \psi_0^A \\ \psi_1^B \\ \psi_1^A \\ \\ \\ \psi_{N-2}^A \\ \psi_{N-1}^B \\ \psi_{N-1}^A \end{pmatrix} = \varepsilon \begin{pmatrix} \psi_0^B \\ \psi_0^A \\ \psi_1^B \\ \psi_1^A \\ \\ \\ \psi_{N-2}^A \\ \psi_{N-1}^B \\ \psi_{N-1}^A \end{pmatrix}. \tag{A.6}$$

Appendix B

Recursive Green's function

A scattering region connected to 2 leads, as shown in Fig. B.1. The conductance coefficients is given through the Landauer-Büttiker formula

$$G_{l,l'} = \frac{e^2}{h} \sum |t_{ll',mn}|^2 \,, \tag{B.1}$$

where l and l' represents the index of the leads, m and n are the index of the channels in each lead. In the expression of the Green's function, the conductivity is equal to the form [105]:

$$G = \frac{e^2}{h} \mathcal{T}r[\Gamma_l G^r_{l,l'} \Gamma_{l'} G^a_{l',l}] \,, \tag{B.2}$$

where $G^{r,a}$ are the retarded and advanced Green's functions of the whole system. $G^{r,a}_{l,l'}$ is the Green's functions connecting the leads l and l'. Γ is the current operator and defined by the expression

$$\Gamma_l = i[\Sigma^r_l - \Sigma^{r\dagger}_l] \,. \tag{B.3}$$

The surface self energy Σ^r_l which is related to the interface of the leads and the scattering region is

$$\Sigma^r_l = u_l g^r_l u^\dagger_l \,. \tag{B.4}$$

g_l is the lead Green's function of the surface of the lead l before connecting to the scattering region. $u_{L,R}$ is the connecting (hopping) matrix between adjacent slice in the leads, shown in the Fig. B.2.

To calculate the Green's function of the system, we slice the smaple in many adjacent segments. The schematic configuration is plot in the Fig. B.2. Each slice can be describe

precisely by an isolated tight-binding Hamiltonian. This Hamiltonian matrix only considers the slice itself without any of its neighborhoods. The associated Green's function of the slice i is $G_{0,i,i} = (E - H_{i,i} + i\eta)^{-1}$ Between any adjacent slices, a connection matrix $H_{i,j}$ is defined to describe the hopping between slice i and j. Then, the adjacent two slice is glued through Dyson formulas,

$$G = G^{(0)} + GVG^{(0)}\,, \tag{B.5}$$

where the perturbation V has the components $V_{i,j} = H_{i,j}$. The definitions of the variables and subscripts are shown in Fig. B.2 for explicit.

Repeat this process, we can build the Green's function of the whole system slice by slice, therefore it is named 'recursive'.

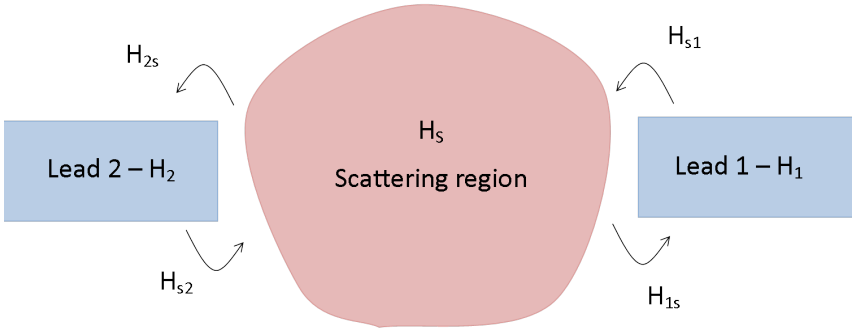

Figure B.1: Schematic show of the scattering region connect to 2 leads.

B.1 Explicit equations in graphene

We have seen the basic idea of the recursive Green's function theory (RGFT) technique. In this section we will write down the explicit equations calculated out from the general expressions given in the last section above.

The composite scheme of the RGFT method is demonstrated in the Fig. B.3. There are no difficult to define the Hamiltonian matrix of each slice and the hopping between slices as shown in the figure, Fig. B.3. By substitute all the quantities into the Dyson equation B.5, we will obtain the formulas of the Green's functions we needed. These equations serve as bricks in building the whole system's Green function and are list below: [105]

$$G^r_{i,i} = G^r_{0,i,i} + G^r_{0,i,i} H_{i,i+1} G^r_{i+1,i}\,, \tag{B.6a}$$

$$G^r_{i+1,i} = G^r_{0,i+1,i+1} H_{i,i+1} G^r_{i,i}\,. \tag{B.6b}$$

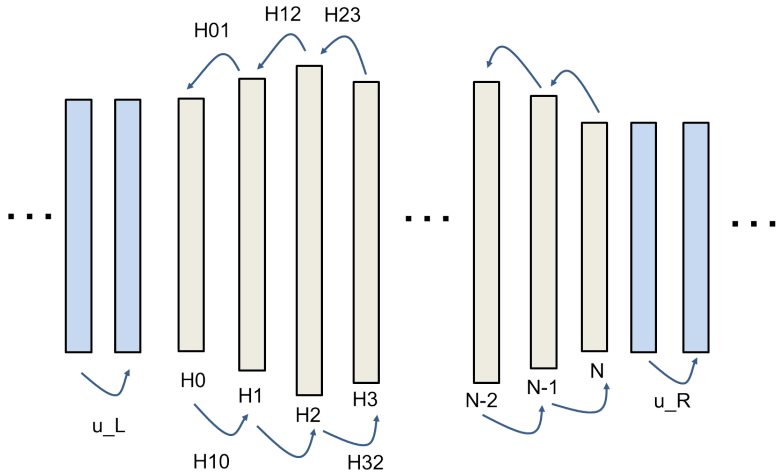

Figure B.2: Schematic show of the slicing of the sample in recursive Green's function technique.

Note that $G^r_{N+1,N+1} = g^r_R$ and $G^r_{0,0} = g^r_L$. Till now, the only quantities unknown are the surface Green's functions g^r_L and f^r_R.

The transmission matrix $t_{ll',mn}$ can be written in details, its form reads:

$$t_{ll',mn} = \frac{i}{\hbar\sqrt{|v^l_{m,in}||v^{l'}_{n,out}|}}(\phi^l_{m,in})^\dagger \Gamma_l G^r_{N+1,0}\Gamma_{l'}\phi^{l'}_{n,out} \tag{B.7}$$

for $l \neq l'$.

$$r_{ll,mn} = \frac{1}{\hbar\sqrt{|v^l_{m,in}||v^l_{n,out}|}}\left(i(\phi^l_{m,in})^\dagger \Gamma_l G^r_{N+1,0}\Gamma_l\phi^l_{n,out} - (\phi^l_{m,in})^\dagger\Gamma_l\phi^l_{n,out}\right) \tag{B.8}$$

for $l = l'$.

$v^l_{m,in}$ and $v^{l'}_{n,out}$ are the group velocity of the incident and outgoing propagation modes in lead l and l' respectively. $\phi^l_{m,in}$ and $\phi^{l'}_{n,out}$ are the eigenvectors of the incident and outgoing propagation modes in lead l and l'. The derivate of these quantities will be explained in the next section.

B.2 Leads' surface Green's function

The leads' surface Green's function can be derived through numerically approach or eigenvalue algorithms method. The method has been explicitly explained in section 3.2 in the

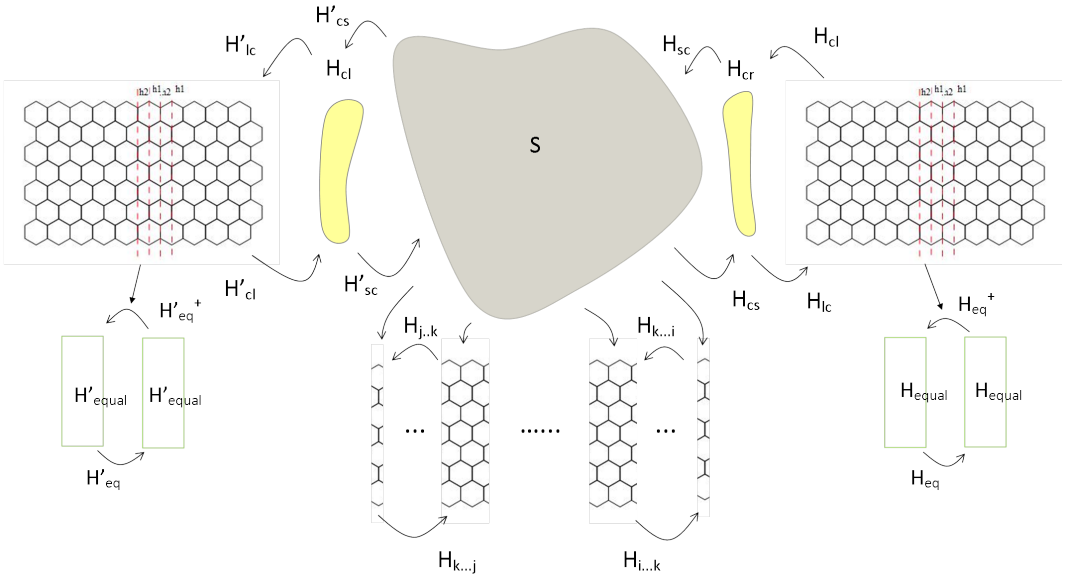

Figure B.3: The schematic figure showing the process of composing cells for graphene structures.

reference Ref. and well summered in the appendix D3 there. So here for simplicity I skipped the complicated derivative but the results, which is similar as the Algorithm D.1. in the reference mentioned. However, some modification is needed in the case of graphene leads. In the graphene lead (nanoribbon), the period of the repeated lattice segment is not 1-slice of the ribbon. In zigzag graphene nanoribbon, the period of the repeated segments is 2. In armchair graphene nanoribbon, this period is 4. In our example, see the Fig. B.3, we use the zigzag nanoribbon. We can convert the 2-slice period lattice system into an equivalent 1-slice period problem through the tight-binding equations: [106]

$$h_{01}^{\dagger}\Psi_0(i)+h_1\Psi_1(i)+h_{01}(i+1)=E\Psi_1(i)\,, \tag{B.9a}$$
$$h_{10}^{\dagger}(i-1)+h_0\Psi_1(i)+h_{10}\Psi_1(i)=E\Psi_0(i)\,, \tag{B.9b}$$
$$H_{Sl}^{\dagger}\Psi_S+h_0\Psi_0(i)+h_{01}\Psi_1(0)=E\Psi_0(0)\,, \tag{B.9c}$$

which has an equivalent equations of the form

$$H_{eq}^{\dagger}\Psi_0(i-1)+H_{equal}\Psi_0(i)+H_{eq}\Psi_0(i+1)=E\Psi_0(i)\,, \tag{B.10a}$$
$$H_{Sc}^{\dagger}\Psi_S+H_{cl}\Psi_0(0)+H_c\Psi_0(1)=E\Psi_0(0)\,, \tag{B.10b}$$

where

$$H_{equal} = h_{10}^{\dagger}(E-h_1)^{-1}h_{10} + h_0 + h_{01}(E-h_1)^{-1}h_{01}^{\dagger}\,, \tag{B.11a}$$

$$H_{eq} = h_{01}(E-h_1)^{-1}h_{10}\,, \tag{B.11b}$$

$$H_{cl} = h_0 + h_{01}(E-h_1)^{-1}h_{01}^{\dagger}\,. \tag{B.11c}$$

The transport eigenmodes $\phi_{m(n)}$ described in Eq. B.7 & B.8 are obtained by solving the eigenproblem [105]

$$A\begin{pmatrix}\phi_n\\ \lambda_n\phi_n\end{pmatrix} = \lambda_n\begin{pmatrix}\phi_n\\ \lambda_n\phi_n\end{pmatrix}, \tag{B.12}$$

where operator A has the form

$$A = \begin{pmatrix} 0 & 1 \\ -(H'_{eq})^{-1}(H'_{eq})^{\dagger} & (H'_{eq})^{-1}(E-H'_{equal})\end{pmatrix}. \tag{B.13}$$

The group velocity operator v_n is defined as

$$v_n = -1/\hbar\ \mathrm{Im}(2\phi_n^{\dagger}H'_{equal})\lambda_n\phi_n)\,. \tag{B.14}$$

Then pick out the right moving solutions by checking the corresponding velocity of the modes ϕ_n, i.e. for all modes with velocity $v_n > 0$. The surface Green's function of one lead is constructed

$$g_R^r = U_R\Lambda_R U_R^{-1}(H_{eq}'^{\dagger})^{-1}\,, \tag{B.15a}$$

$$U_R = (\phi_{1,v_1>0}, \phi_{2,v_2>0},\ \ldots, \phi_{1,v_n>0})\,, \tag{B.15b}$$

$$\Lambda_R = \mathrm{diag}(\lambda_{1,v_1>0}, \lambda_{2,v_2>0},\ \ldots, \lambda_{n,v_n>0})\,. \tag{B.15c}$$

The other leads (e.g. the left lead g_L^r) can be constructed through the same way.

B.3 Current

The local current density is defined by [106]

$$\mathbf{j}(\mathbf{x}_i, E) = \frac{1}{2\pi\hbar}\sum_j(\mathbf{x}_j - \mathbf{x}_i)\mathrm{Re}(H_{i,j}G^{<}_{j,i}(E))\,, \tag{B.16}$$

where $G^{<}$ is the lesser Green's function and has the following definitions. More details can be consulted to the reference [106, 107]:

$$G^{<}_{i,i} = G^{r}_{i,i}(\Sigma^{L,<}_{i,i} + \Sigma^{R,<}_{i,i})G^{a}_{i,i}\,, \tag{B.17a}$$

$$G^{<}_{i+1,i} = G^{R,r}_{i+1,i+1}H_{i+1,i}G^{<}_{i,i} + G^{R,<}_{i+1,i+1}H_{i+1,i}G^{a}_{i,i} \tag{B.17b}$$

and

$$\Sigma^{L(R),<}_{i,i} = H_{i,i-1}G^{L(R),<}_{i-1,i-1}H_{i-1,i}\,, \tag{B.18a}$$

$$G^{L(R),<}_{i,i} = (G^{L(R),r}_{i,i}H_{i,i})G^{L(R),<}_{i-1,i-1}(G^{L(R),r}_{i,i}H_{i,i-1})^{\dagger}\,. \tag{B.18b}$$

B.4 Summery of the algorithms

The standard procedure of performing the RGFT technique is (for the case of 2 leads connected to a scattering region):

1. Calculated the surface Green's function of the leads.

2. Construct the Green's function of the whole system by sweeping from one end to another end, e.g. from left lead to the right. The equations used in building the sets of the Green's functions of the complete system are the Eq. B.6.

3. Using the sets of the Green's function obtained, the transmission is calculated by the Eq. B.7.

4. The local current density is calculated through the Eq. B.16.

Appendix C

The numerical calculation of Chern number in graphene

Numerical calculation of Chern number (c) requests a discretization of the Brillouin zone(BZ). Then, the Berry connection is obtained by the integration of the Berry curvature over the reciprocal space of the torus, which is isomorphic to a single Brillouin zone. Here we are using the method developed in the papers [99, 108]. There the Chern number c can be simply calculated through a summation of the field strength or, equivalently speaking, the Berry curvature defined on the discretized plaquettes of the Bloch sphere [109]. The calculation of the Berry curvature requires the knowledge of the states vector or here the eigenvector of tight- binding model.

Following the paper [99] the field strength on plaquette $([k_x, k_x + \delta k_x], [k_y, k_y + \delta k_y])$ is defined as

$$F(k) = \ln \left(U_{k_x}(k_x, k_y) U_{k_y}(k_x + \delta k_x, k_y) U_{k_x}(k_x, k_y + \delta k_y)^{-1} U_{k_y}(k_x, k_y)^{-1}) \right) , \tag{C.1}$$

where $U_{k_x}(k_y) = \frac{\det\left(\psi^\dagger(k)\psi(k+k_x(k_y))\right)}{|\det\left(\psi^\dagger(k)\psi(k+k_x(k_y))\right)|}$ is the relative phase linking the neighbouring mesh points on the BZ, (k_x, k_y) with $(k_x + \delta k_x, k_y)$ as well as with $(k_x, k_y + \delta k_y)$. Then the Chern number is thus calculated as a sum of the Berry phases or curvatures over all plaquettes covering the BZ. In fact it is simply the flux of the field strength, $F(k)$, penetrating the BZ:

$$c = \frac{1}{2\pi i} \sum_k F(k). \tag{C.2}$$

Now for a specific example of the Chern number calculation we choose the unit cell as shown in the Fig. C.1. There we also use a convenient gauge defined, so as each plaquette is penetrated by the flux Φ. It is associated with a proper choice of periodic boundary

condition over plaquettes. This setting is similar to one used in the Ref. [110]. We consider thecae here when the value of magnetic flux through the chosen plaquette is equal to equal to some fractional number p/q, that is $\Phi/\Phi_0 = p/q$. Then our Hamiltonian of the tight-binding model takes the form,

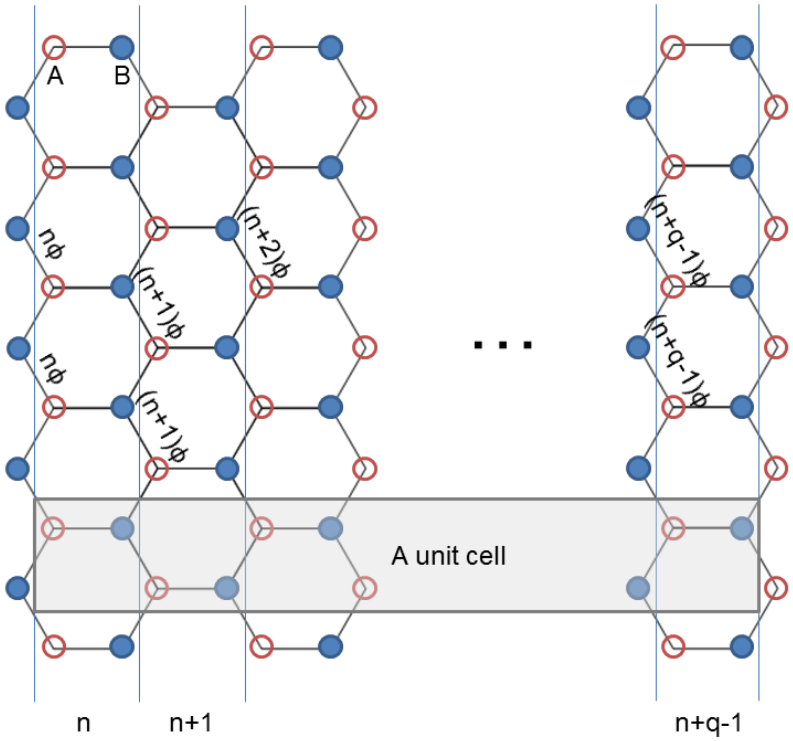

Figure C.1: Schematic graph showing the geometry of the unit cell chosen. The gauge has been chosen in a form, which we found convenient for our calculations of the the Chern-number. The magnetic flux per unit cell is chosen to be equal to some fractional p/q number of the elementary flux quantum.

$$H = \begin{pmatrix} \mu & 1 & & & & & & & & a_q e^{-i\frac{3}{2}k_x qa} \\ 1 & \mu & a_0^* & & & & & & & \\ & a0 & \mu & 1 & & & & & & \\ & & 1 & \mu & a_1^* & & & & & \\ & & & a_1 & \mu & 1 & & & & \\ & & & & & \cdots & & & & \\ & & & & & a_{q-2} & \mu & 1 & & \\ & & & & & & 1 & \mu & a_{q-1}^* & \\ & & & & & & & a_{q-1} & \mu & \\ a_q^* e^{i\frac{3}{2}k_x qa} & & & & & & & & 1 & \mu \end{pmatrix}. \quad \text{(C.3)}$$

Where $a_n(k_y) = 2e^{i(n\pi\frac{p}{q}+\frac{\sqrt{3}k_y a}{2})}\cos(n\pi\frac{p}{q}+\frac{\sqrt{3}k_y a}{2})$.

Here the BZ is defined as $\{(k_x,k_y)|k_x \in [-\frac{2\pi}{3qa},\frac{2\pi}{3qa}), k_y \in [-\frac{\pi}{\sqrt{3}qa},\frac{\pi}{\sqrt{3}qa})\}$.

The eigenvectors of the Hamiltonian matrix, the eq.(C.3), define the tight-binding states wave vectors $\{|n_{\varepsilon_1}\rangle|n_{\varepsilon_2}\rangle\ldots|n_{\varepsilon_q}\rangle\}$. Therefore, using these vectors we built up the wave function, $\psi(k)$, of the filled states as $\psi(k) = (|n_{\varepsilon_1}\rangle \ldots |n_{\varepsilon_f}\rangle)$. Here we have taken into account all filled states, only. By substituting $\psi(k)$ into the eq. (C.1) we estimate the field strength or the Berry curvature through different plaquettes. Next, with the use of the eq. (C.2), we calculate the total flux of this field through the BZ, which is the Chern number c. Some characteristic results of our calculations are shown in the Fig. C.2. Therewith such calculations we were able to reproduce the results presented in the Ref. [108].

Note that: 1) flipping the magnetic field direction changes the sign of c; 2) when the Fermi energy rises and crossing the zero Landau level in graphene the Chern number changes from -1 to 1. 3) We have also observed large jumps in the Chern number, see the Fig.C.2. They take place when the Fermi energy crossing the saddle points of the graphene's tight-binding spectrum. Now we can also see, that the topological invariant number c changes from -1 to 1, when we crossing the interface from left to right. This happens in both cases when the magnetic field changes sign and where the graphene PN-junction does exist. In our notations these cases are noted as $H[-,+;+,+]$ & $H[+,+;-,+]$.

In the Nambu representation of the Hamiltonian, eq. (3), the link determinant U_k defined in eq. C.1 is equal to the multiplication of the individual determinants of the particle ($\mathcal{H}_k$) and of the hole branch of the spectrum ($\mathcal{H}^*_{-k}$), i.e. $U_k = U_k(\mathcal{H}_k)U_k(\mathcal{H}^*_{-k})$. Evidently, the field strength F is resulting from the sum of the two representations: $F(k) = F(\mathcal{H}_k)+F(\mathcal{H}^*_{-k})$. The practical form of the Nambu redundant representation should depend on the ways of particle-hole pairing. However if we assume that the Hamiltonian has the particle-hole symmetry, that is, its form is invariant with respect to the complex conjugate

operation, C, which converts $C\mathcal{H}(k)C^{-1} \rightarrow -\mathcal{H}(-k)$. The latter is equivalent to the flipping of the magnetic field. Then the Chern number of this Nambu redundant representation would be doubled. Moreover the invariant index changes on opposite sides of the interface. Here, when the Fermi energy is between the zero and the first Landau level, i.e. in the lowest gap of the spectrum, the Chern number changes would be from -2 to 2 rather than -1 to 1.

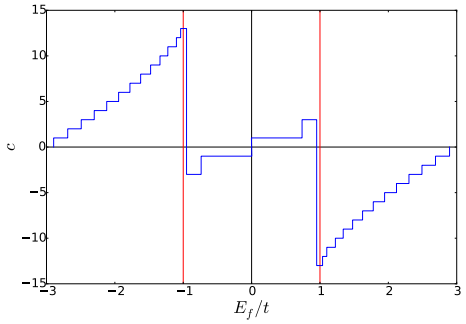

(a) $\Phi/\Phi_0 = 1/17$

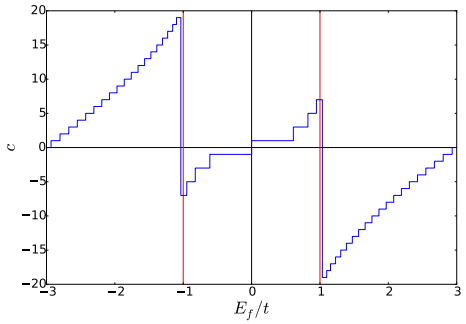

(b) $\Phi/\Phi_0 = 1/27$

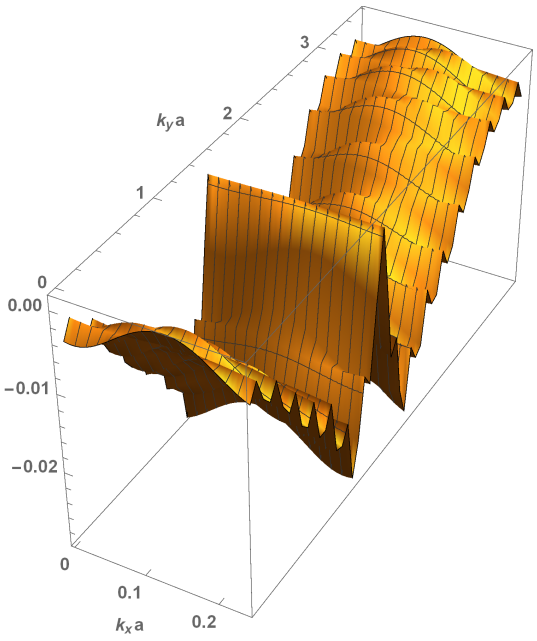

(c) $F|_{\frac{\Phi}{\Phi_0}=\frac{1}{17},\varepsilon<\varepsilon_{15}}$

Figure C.2: The Chern number c numerically calculated at different position of the Fermi energy taken over whole tight-binding band. The magnetic flux per unit cell on Fig. (a) is taken as $\Phi = \frac{1}{17}\Phi_0$ and on the Fig (b) - as $\Phi = \frac{1}{27}\Phi_0$. The characteristic field strength is shown on the Fig. (c) . The large jump in the Chern number takes place when the Fermi energy is crossing the saddle points of the graphene energy spectrum. All jumps are marked by the red vertical lines.

References

[1] P. R. Wallace. The band theory of graphite. *Phys. Rev.*, 71:622–634, 1947.

[2] S. V. Morozov D. Jiang Y. Zhang S. V. Dubonos I. V. Grigorieva A. A. Firsov K. S. Novoselov, A. K. Geim. Electric field in atomically thin carbon films. *Science*, 306:666–669, 2004.

[3] F. Schedin T. J. Booth V. V. Khotkevich S. V. Morozov K. S. Novoselov, D. Jiang and A. K. Geim. Two-dimensional atomic crystals. *PNAS*, 102:10251–10453, 2005.

[4] A. K. Geim and K. S. Novoselov. The rise of graphene. *Nature Materials*, 6:183–191, 2007.

[5] J. Hone H. L. Stormer K. I. Bolotin, K. J. Sikes and P. Kim. Temperature-dependent transport in suspended graphene. *Phys. Rev. Lett.*, 101:096802, 2008.

[6] K. S. Novoselov M. I. Katsnelson and A. K. Geim. Chiral tunnelling and the klein paradox in graphene. *Nature Physics*, 2:620–625, 2006.

[7] A Chaves J. M. Pereira Jr, F. M. Peeters and G. A. Farias. Klein tunneling in single and multiple barriers in graphene. *Semicond. Sci. Technol*, 25:033002, 2009.

[8] Z. A. Maizelis A. Levchenko V. A. Yampol'skii, S. S. Apostolov and F. Nori. Voltage-driven quantum oscillations of conductance in graphene. *EPL*, 96:67009, 2011.

[9] B. Huard N. Stander and D. Goldhaber-Gordon. Evidence for klein tunneling in graphene p-n junctionss. *Phys. Rev. Lett.*, 102:026807, 2009.

[10] M. P. Pierpoint F. V. Kusmartsev K. C. Yung, W. M. Wu. Introduction to graphene electronics - a new era of digital transistors and devices. *Contemp. Phys*, 54:233–251, 2013.

[11] F. V. Kusmartsev et al. Application of graphene wihin optoelectronic devices and transistors. *Applied Spectroscopy and the Science of Nanomaterials. Springer Singapore*, pages 191–221, 2015.

[12] Y. Zhang S. V. Morozov H. L. Stormer U. Zeitler J. C. Maan G. S. Boebinger P. Kim A. K. Geim K. S. Novoselov, Z. Jiang. Room-temperature quantum hall effect in graphene. *Science*, 315:1379, 2007.

[13] F. Duerr A. Luican X. Du, I. Skachko and E. Y. Andrei. Fractional quantum hall effect and insulating phase of dirac electrons in graphene. *Nature*, 462:192–195, 2009.

[14] P. Cadden-Zimansky L. Wang H. Ren K. Watanabe T. Taniguchi P. Kim J. Hone C. R. Dean, A. F. Young and K. L. Shepard. Multicomponent fractional quantum hall effect in graphene. *Nature Physics*, 7:693–696, 2011.

[15] E. J. Mele F. V. Kusmartsev Y. Liu, M. Brada. Magnetisation oscillations, boundary conditions and the hofstadter butterfly in graphene flakes. *Annalen der Physik*, 526:449, 2014.

[16] E. McCann and V. I. Fal'ko. Symmetry of boundary conditions of the dirac equation for electrons in carbon nanotubes. *J. Phys.: Condens. Matter*, 16:2371–2379, 2004.

[17] A. R. Akhmerov and C. W. J. Beenakker. Boundary conditions for dirac fermions on a terminated honeycomb lattice. *Phys. Rev. B*, 77:085423, 2008.

[18] L. Brey and H. A. Fertig. Electronic states of graphene nanoribbons studied with the dirac equation. *Phys. Rev. B*, 73:235411, 2006.

[19] I. Adagldell K. Richter J. Wurm, M. Wlmmer and H. U. Baranger. Interfaces within graphene nanoribbons. *New Journal of Physics*, 11:095022, 2009.

[20] N. M. R. Peres, A. H. Castro Neto, and F. Guinea. Conductance quantization in mesoscopic graphene. *Phys. Rev. B*, 73:195411, 2006.

[21] N. M. R. Peres, A. H. Castro Neto, and F. Guinea. Dirac fermion confinement in graphene. *Phys. Rev. B*, 73:241403, 2006.

[22] D. Abanin L. Levitov G. Li, A. Luican-Mayer and E. Y. Andre. Evolution of landau levels into edge states in graphene. *Nature comm.*, 4:1744, 2013.

[23] M. I. Katsnelson M. A. H. Vozmediano and F. Guinea. Gauge fields in graphene. *Phys. Rep.*, 496:109–148, 2010.

[24] F. M. Peeters M. Ramezani Masir, D. Moldovan. Pseudo magnetic field in strained graphene: Revisited. *Solid State Commun.*, 175-176:76–82, 2013.

[25] A. K . Geim F. Guinea., M. I. Katsnelson. Energy gaps and a zero-field quantum hall effect in graphene by strain engineering. *Nature Physics*, 6:30, 2010.

[26] M. A. H. Vozmediano F. Guinea, M. I. Katsnelson. Midgap states and charge inhomogeneities in corrugated graphene. *Phys. Rev. B*, 77:075422, 2008.

[27] Baruch Horovitz F. Guinea and P. Le Doussal. Gauge field induced by ripples in graphene. *Phys. Rev. B*, 77:205421, 2008.

[28] A. M. Tsvelik Katsnelson T. O. Wehling, A. V. Balatsky and A. I. Lichtenstein. Midgap states in corrugated graphene: Ab initio calculations and effective field theory. *EPL*, 84:17003, 2008.

[29] R. Peierls. On the theory of diamagnetism of conduction electrons. *Z. Phys.*, 80:763, 1933.

[30] Edward McCann and Vladimir I. Fal'ko. Symmetry of boundary conditions of the dirac equation for electrons in carbon nanotubes. *J. Phys.: Condens. Matter*, 16:2371, 2004.

[31] A. R. Akhmerov and C. W. J. beenakker. Weak localization in monolayer and bilayer graphene. *Phys. Rev. B*, 77:085423, 2008.

[32] G. Montambaux P. Delplace, D. Ullmo. Zak phase and the existence of edge states in graphene. *Phys. Rev. B*, 84:195452, 2011.

[33] Markus B$\acute{}$uttiker Jian Li, Alberto F. Morpurgo and Ivar Martin. Marginality of bulk-edge correspondence for single-valley hamiltonians. *Phys. Rev. B*, 82:245404, 2010.

[34] V. I. Fal'ko H. Suzzuura T. Ando K. Kechedzhi, E. McCann and B. L. Altshuler. Weak localization in monolayer and bilayer graphene. *Eur. Phys. J. Special Topics*, 148:39–54, 2007.

[35] Y. Aharonov and D. Bohm. Significance of electromagnetic potentials in the quantum theory. *Phys. Rev.*, 115, 1959.

[36] D. Bohm Y. Aharonov. Significance of electromagnetic potentials in the quantum theory. *Phys. Rev*, 115, 1959.

[37] F. Guinea. Models of electron transport in single layer graphene. *J. Low. Temp Phys.*, 153:359–373, 2008.

[38] M.P. Pierpoint F.V. Kusmartsev K.C. Yung, W.M. Wu. Introduction to graphene electronics - a new era of digital transistors and devices. *Contemp. Phys.*, 54:233–251, 2013.

[39] A. H. Castro Neto, F. Guinea, N. M. R. Peres, K. S. Novoselov, and A. K. Geim. The electronic properties of graphene. *Rev. Mod. Phys.*, 81:109–162, 2009.

[40] Y. Zhang S. V. Morozov H. L. Stormer U. Zeitler J. C. Maan G. S. Boebinger P. Kim A. K. Geim K. S. Novoselov, Z. Jiang. Room-temperature quantum hall effect in graphene. *Science*, 315:1379, 2007.

[41] A Chagves J M Pereira Jr, F M Peeters and G A Farias. Klein tunneling in single and multiple barriers in graphene. *Semicond. Sci. Technol.*, 25:033002, 2010.

[42] M.O. Goerbig. Electronic properties of graphene in a strong magnetic field. *Rev. Mod. Phys.*, 83:1193, 2011.

[43] L. Ma G. T. Liu L. Lu Z. Tan, C. Tan and C. L. Yang. Shubnikov-de haas oscillations of a single layer graphene under dc current bias. *Phys. Rev. B*, 84:115429, 2011.

[44] J. G. Pedersen and T. G. Pedersen. Hofstadter butterflies and magnetically induced band-gap quenching in graphene antidot lattices. *Phys. Rev. B*, 87:235404, 2013.

[45] L. Brown et al. Polycrystalline graphene with single crystalline electronic structure. *Nano Lett.*, 14 (10):5706–5711, 2014.

[46] M. P. Pierpoint F. V. Kusmartsev, W. M. Wu. Chapter *Application of Graphene within Optoelectronic Devices and Transistors* chapter in the book: Applied spectroscopy and the science of nanomaterials, 978-981-287-241-8, 316600 1 en, (9), the series *Progress Optical Science and Photonics. Prabhakar Misra (Eds)*, 2, 2014.

[47] S.D. Ganichev M.M. Glazov. High frequency electric field induced nonlinear effects in graphene. *Phys. Rep.*, 535:101–138, 2014.

[48] F. Ortmann R. Martinez-Gordillo, S. Roche and M. Pruneda. Transport fingerprints at graphene superlattice dirac points induced by a boron nitride substrate. *Phys. Rev. B*, 89:161401 (R), 2014.

[49] Y.-W. Son M.L. Cohen C.-H. Park, L. Yang and S.G. Louie. New generation of massless dirac fermions in graphene under external periodic potentials. *Phys. Rev. Lett.*, 101:126804, 2008.

[50] M. Lohse-J. T. Barreiro B. Paredes M. Aidelsburger, M. Atala and I. Bloch. Realization of the hofstadter hamiltonian with ultracold atoms in optical lattices. *Phys. Rev. Lett.*, 111, 2013.

[51] W. Wohlleben K.W. Madison, F. Chevy and J. Dalibard. Vortex formation in a stirred bose-einstein condensate. *Phys. Rev. Lett.*, 84:806, 2000.

[52] P. Engels-V.P. Mogendorff V. Schweikhard, I. Coddington and E.A. Cornell. Rapidly rotating bose-einstein condensates in and near the lowest landau level. *Phys. Rev. Lett.*, 92:040404, 2004.

[53] K. Jiménez-García J. V. Porto Y. Lin, R. L. Compton and I. B. Spielman. Synthetic magnetic fields for ultracold neutral atoms. *Nature (London)*, 462:628, 2009.

[54] G. Juzeliūnas J. Dalibard, F. Gerbier and P. ́Ohberg. Colloquium: artificial gauge potentials for neutral atoms. *Rev. Mod. Phys.*, page 1523, 2011.

[55] G. Gómez-Santos and T. Stauber. Measurable lattice effects on the charge and magnetic response in graphene. *Phys. Rev. Lett.*, page 045504, 2011.

[56] Jun-Won Rhim and Kwon Park. *Phys. Rev. B*, 86:235411, 2012.

[57] D. P. DiVincenzo and E. J. Mele. Self-consistent effective-mass theory for intralayer screening in graphite intercalation compounds. *Phys. Rev. B*, 29:1685, 1984.

[58] I. A. Luk'yanchuk S. G. Sharapov V. P. Gusynin, V. M. Loktev and A. A. Varlamov. Quantum oscillations as the tool for study of new functional materials. *Low Temp. Phys.*, 40:270.

[59] Igor A. Luk'yanchuk. De haas-van alphen effect in 2d systems: application to mono- and bilayer graphene. *Low Temp. Phys.*, 37:45, 2011.

[60] W. Apel G. Pal and L. Schweitzer. Landau level splitting due to graphene superlattices. *Phys. Rev. B*, 85:235457, 2012.

[61] D.R. Hofstadter. Energy levels and wave functions of bloch electrons in rational and irrational magnetic fields. *Phys. Rev. B*, 14:2239–2249, 1976.

[62] E. McCann and V. I. Fal'ko. Symmetry of boundary conditions of the dirac equation for electrons in carbon nanotubes. *J. Phys. Condens. Matter*, 16:2371, 2004.

[63] A. R. Akhmerov and C. W. J. Beenakker. Detection of valley polarization in graphene by a superconducting contact. *Phys. Rev. Lett.*, 98:157003, 2007.

[64] A. R. Akhmerov and C. W. J. Beenakker. Boundary conditions for dirac fermions on a terminated honeycomb lattice. *Phys. Rev. B*, 77:085423, 2008.

[65] F. D. M. Haldane. Model for a quantum hall effect without landau levels: condensed-matter realization of the parity anomaly. *Phys. Rev. Lett.*, 61:2015, 1988.

[66] F. V. Kusmartsev and A. M. Tsvelik. Semimetallic properties of a heterojunction. *JETP lett.*, 42:257–260, 1985.

[67] C. L. Kane and E. J. Mele. Z2 topological order and the quantum spin hall effect. *Phys. Rev. Lett.*, 95:146802, 2005.

[68] C. L. Kane and E. J. Mele. A new spin on the insulating state. *Science*, 314:1692–1693, 2006.

[69] Shou-Cheng Zhang B. Andrei Bernevig, Taylor L. Hughes. Quantum spin hall effect and topological phase transition in hgte quantum wells. *Science*, 314:1757–1761, 2006.

[70] J. E. Moore. The birth of topological insulators. *Nature*, 164:194–198, 2010.

[71] C. R. Dean et al. Hofstadter's butterfly and the fractal quantum hall effect in moiré superlattices. *Nature (London)*, 497:598, 2013.

[72] G. L. Yu D. D. Elias R. Jalil A. A. Patel A. Mishchenko A. S. Mayorov C. R. Woods J. R. Wallbank M. Mucha-Kruczynski B. A. Piot M. Potemski I. V. Grigorieva K. S. Novoselov F. Guinea V. Falko L. A. Ponomarenko, R. V. Gorbachev and A. K. Geim. Cloning of dirac fermions in graphene superlattices. *Nature (London)*, 497:594–597, 2013.

[73] A. A. Patel M. Mucha-Kruczyński E. McCann V. I. Fal'ko X. Chen, J. R. Wallbank. Dirac edges of fractal magnetic minibands in graphene with hexagonal moiré superlattices. *Phys. Rev. B*, 89:075401, 2014.

[74] A. H. MacDonald R. Bistritzer. Moiré butterflies in twisted bilayer graphene. *Phys. Rev. B*, 84:035440, 2011.

[75] B. J. Robinson-A. Ouerghi O. E. Kusmartseva O. V. Kolosov R. Mazzocco Marat B. Gaifullin A. Ben Gouider Trabelsi, F. V. Kusmartsev and M. Oueslati. Charged nano-domes and bubbles in epitaxial graphene. *Nanotechnology*, 25:165704, 2014.

[76] O. E. Kusmartseva F. V. Kusmartsev M. Oueslati A. Ben Gouider Trabelsi, A. Ouerghi. Raman spectroscopy of four epitaxial graphene layers: Macro-island grown on 4h-sic (000-1) substrate and an associated strain distribution. *Thin Solid Films*, 539:377–383, 2013.

[77] F. V. Kusmartsev A. O'Hare and K. I. Kugel. A stable flat form of two-dimensional crystals: could graphene, silicene, germanene be minigap semiconductors. *Nano Lett.*, 12 (2):1045–1052, 2012.

[78] M. Wilde Ch. Heyn M. P. Schwarz, D. Grundler and D. Heitmann. Magnetization of semiconductor quantum dots. *J. Appl. Phys.*, 91:6875, 2002.

[79] A. A. Koronovskii et al. A. E. Hramov, V. V. Makarov. Subterahertz chaos generation by coupling a superlattice to a linear resonator. *Phys. Rev. Lett.*, 112:116603, 2014.

[80] M. I. Katsnelson M. A. H. Vozmediano and F. Guinea. Gauge fields in graphene. *Phys. Rep.*, 496:109, 2010.

[81] F. M. Peeters M. Ramezani Masir, D. Moldovan. Pseudo magnetic field in strained graphene: revisited. *Solid State Commun.*, 175-176:76–82, 2013.

[82] A. K. Geim F. Guinea., M. I. Katsnelson. Energy gaps and a zero-field quantum hall effect in graphene by strain engineering. *Nat. Phys.*, 6:30–33, 2010.

[83] K. L. Meaker M. Panlasigui A. Zettl F. Guinea A. H. Castro Neto M. F. Crommie N. Levy, S. A. Burke. Strain-induced pseudo-magnetic fields greater than 300 tesla in graphene nanobubbles. *Science*, 329:544–547, 2010.

[84] T. Ando H. Suzuura. Phonons and electron-phonon scattering in carbon nanotubes. *Phys. Rev. B*, 65:235412, 2002.

[85] J. L. Manes. Symmetry-based approach to electron-phonon interactions in graphene. *Phys. Rev. B*, 76:045430, 2007.

[86] E. M. Lifshitz L. D. Landau. Course of theoretical physics: Theory of elasticity. *London: Pergamon*, 1959.

[87] M. I. Katsnelson F. Guinea, A. K. Geim and K. S. Novoselov. Generating quantizing pseudomagnetic fields by bending graphene ribbons. *Phys. Rev. B*, 81:035408, 2010.

[88] M. I. Katsnelson K. V. Zakharchenko and A. Fasolino. Finite temperature lattice properties of graphene beyond the quasiharmonic approximation. *Phys. Rev. Lett.*, 102:046808, 2009.

[89] Vladimir I. Fal'ko H. Suzuura T. Ando E. McCann, K. Kechedzhi and B. L. Altshuler. Weak-localization magnetoresistance and valley symmetry in graphene. *Phys. Rev. Lett.*, 97:146805, 2006.

[90] I. A. Luk'yanchuk S. G. Sharapov V. P. Gusynin, V. M. Loktev and A. A. Varlamov. Quantum oscillations as the tool for study of new functional materials. *Low Temp. Phys.*, 40:270, 2014.

[91] S. Slizovskiy and J. J. Betouras. Nonlinear magnetization of graphene. *Phys. Rev. B*, 86:125440, 2012.

[92] Baruch Horovitz F. Guinea and P. Le Doussal. Gauge field induced by ripples in graphene. *Phys. Rev. B*, 77:205421, 2008.

[93] M.-H. Liu E. Tóvári M. Weiss R. Maurand K. Richter P. Rickhaus, P. Makk and C. Schonenberger. Snake trajectories in ultraclean graphene p-n junctions. *Nat. Comm.*, 6:6470, 2015.

[94] Y. Yeo K. Watanabe T. Taniguchi T. Taychatanapat, J. Y. Tan and B. Ozyilmaz. Conductance oscillations induced by ballistic snake states in a graphene heterojunction. *Nat. Comm.*, 6:6093, 2015.

[95] A. Altland and M. R. Zirnbauer. Nonstandard symmetry classes in mesoscopic normal-superconducting hybrid structures. *Phys. Rev. B*, 55:1142, 2005.

[96] A. Furusaki A. P. Schnyder, S. Ryu and A. W. W. Ludwig. Classification of topological insulators and superconductors in three spatial dimensions. *Phys. Rev. B*, 78:195125, 2008.

[97] A. Furusaki S. Ryu, A. P. Schnyder and A. W. W. Ludwig. Topological insulators and superconductors: tenfold way and dimensional hierarchy. *New J. Phys.*, 12:065010, 2010.

[98] Y. Tanaka M. Ezawa and N. Nagaosa. Topological phase transition without gap closing. *Sci. Rep.*, 3:2790, 2013.

[99] Y. Hatsugai T. Fukui and H. Suzuki. Chern numbers in discretized brillouin zone: Efficient method of computing (spin) hall conductances. *J. Phys. Soc. Jpn.*, 74:1674, 2005.

[100] N. M. R. Peres K. S. Novoselov A. H. Castro Neto, F. Guinea and A. K. Geim. The electronic properties of graphene. *Rev. Mod. Phys.*, 81:109, 2009.

[101] F. V. Kusmartsev and A. M. Tsvelik. Semimetalic properties of a heterojunction. *JETP lett.*, 42:257–260, 1985.

[102] X. Gong-Jie X. Xu-Guang, Z. Chao and C. Jun-Cheng. Electron tunneling in single layer graphene with an energy gap. *Phys. Rev. B*, 20:027201, 2011.

[103] J. V. Gomes and N. M. R. Peres. tunnelling of dirac electrons through spactial regions of finite mass. *J. Phys.:Condens. Matter*, 20:324221, 2008.

[104] M. R. Setare and D. Jahnai. electronic transmission through p-n and n-p-n junctions of graphene. *J. Phys.:Condens. Matter*, 22:245503, 2010.

[105] M. Wimmer. Quantum transport in nanostructures: From computational concepts to spintronics in graphene and magnetic tunnel junctions. url:http://epub.uni-regensburg.de/12142/, 2009.

[106] J. Schelter. The aharonov-bohm effect and resonant scattering in graphene. *UniversitÃđt WÃijrzburg, Fakultat fur Physik und Astronomie*, 2013.

[107] Eduardo R. Mucciolo Caio H. Lewenkopf. The recursive green's function method for graphene. *Journal of Computational Electronics*, 12:203–231, 2013.

[108] H. Aoki Y. Hatsugai, T. Fukui. Topological aspects of graphene dirac fermions and the bulk-edge correspondence in magnetic fields. *EPJ.*, 148:133–141, 2007.

[109] László Oroszlány János Asbóth and AndrásPályi. Topological insulators. *http://fizipedia.bme.hu/images/1/14/Topological_insulators.pdf*.

[110] Jun-Won Rhim and Kwon Park. Self-similar occurrence of massless dirac particles in graphene under a magnetic field. *Phys. Rev. B*, 86:235411, 2012.